INVESTIGATION OF THE SECOND-ORDER VELOCITY SLIP AND TEMPERATURE-JUMP IN MICROCHANNEL FLOWS

By
Vladimir Akram Hammoudeh

Supervisor
Dr. Mohammad A. Hamdan, Prof.

Co-Supervisor
Dr. Mohammad A. Al-Nimr, Prof.

This Dissertation was Submitted in Partial Fulfillment of the Requirements for the Doctor of Philosophy Degree in Mechanical Engineering

Faculty of Graduate Studies
The University of Jordan

December, 2007

Committee Decision

This dissertation; "Investigation of the Second-Order Velocity-Slip and Temperature-Jump in Microchannel Flows" was successfully defended and approved on Nov. 27th, 2007.

Examination Committee	**Signature**
Dr. Mohammad A. Hamdan, Chairman Prof. of Mech. Eng.	……
Dr. Mohammad A. Al-Nimr, Co-Chairman Prof. of Mech. Eng.	……
Dr. Ali A. Badran, Member Prof. of Mech. Eng.	……
Dr. Ahmad S. A. Al-Salaymeh, Member Associate Prof. of Mech. Eng.	……
Dr. Mohammad I. Al-Kilani, Member Associate Prof. of Mech. Eng.	……
Dr. Khalid Ramadan, Member Associate Prof. of Mech. Eng. (Mu'tah University, Karak)	……

Dedications

To my parents, who saw the potential in me and made me go on all this time.

Acknowledgments

I would like to thank my advisors Prof. Mohammad Hamdan and Prof. Mohammad Al-Nimr for their support, guidance and help, especially Prof. Al-Nimr who was much more than advisor to me, he was a mentor who never stopped encouraging me and never failed to give me the help I needed.

I would also like to thank all the examination committee members: Prof. Ali Badran, Dr. Khalid Ramadan, Dr. Mohammad Al- Kilani and Dr. Ahmad Al-Salaymeh for their valuable comments on this work.

INVESTIGATION OF THE SECOND-ORDER VELOCITY SLIP AND TEMPERATURE-JUMP IN MICROCHANNEL FLOWS

Table of Contents

List of Figures:

List of Symbols

C_f	skin friction coefficient
D	pipe diameter
f	Darcy friction coefficient
Kn	Knudsen number ($=\lambda/L$)
L	reference length (v/u_0 for Stoke's 2nd and $r\alpha$ in Jeffery-Hamel)
M	Mach number
p	pressure
Pr	Prandtl number ($= v/\acute{\alpha}$)
R	pipe radius
r	radial coordinate
Re	Reynolds number ($=u_{max}L/v$)
T	temperature
TP	periodic time ($=2\pi/\omega$)
t	time
U	dimensionless axial velocity ($= u/u_0$)
u	velocity, axial velocity
V	complex solution function for velocity
$\bar{V}$	mean velocity
W	complex solution function for temperature
x	axial coordinate , complex solution function for temperature
X	dimensionless axial coordinate ($=x/L$)
y	transverse coordinate
Y	dimensionless transverse coordinate ($=y/L$)

Greek Letters

α	wall angle
$\acute{\alpha}$	thermal diffusivity
β	coefficient of thermal expansion
γ	specific heat ratio
λ	mean free path length
Δ	second viscosity coefficient
μ	viscosity
ν	kinematic viscosity
ρ	density
η	dimensionless angle ($=\theta/\alpha$)
θ	polar coordinate angle, dimensionless temperature ($=(t - t_\infty)/t_w - t_\infty$)
σ_T	thermal accommodation coefficient
σ_v	tangential momentum accommodation coefficient
τ	dimensionless time ($=t/t_r$)
ϖ	frequency
ω	dimensionless frequency ($=\varpi/\omega_0$)
ω_0	reference frequency ($=v/l^2$ for case 1,2 and 4 and u_0^2/v for case 3)

Subscripts

max	centerline velocity
r	radial component, reference time ($=l^2/\nu$ for case 1, 2 & 4 and ν/u_0^2 for case 3)
w	wall condition, temperature or shear stress
0	reference velocity ($= -l^2(\partial p/\partial x)/\mu$ for case 2 and $g\beta(t_w-t_\infty)l^2/\nu$ for case 4)
∞	ambient condition (temperature)

Investigation of the Second-Order Velocity Slip and Temperature-Jump in Microchannel Flows

By

Vladimir Akram Hammoudeh

Supervisor

Dr. Mohammad A. Hamdan, Prof.

Co-Supervisor

Dr. Mohammad A. Al-Nimr, Prof.

ABSTRACT

In this work, three different cases that cover different flow patterns in microchannels was studied by implementing the first and second order velocity-slip/temperature jump models in order to observe the behavior of the flow so that a certain criteria for the use of each of the no-slip, and the two slip models is established. These three cases are; the Jeffery-Hamel flow in microchannels, Fanno flow in circular microchannels and a number of basic fluctuating flows in microchannels.

In the first part, the Jeffery-Hamel flow case has been studied using both, first order and second order velocity-slip boundary conditions models and then compared to the no-slip boundary conditions solution. The study concentrates on investigating the effect the change of *Kn* number has on the velocity profiles, magnitude of slip at the wall and the skin friction coefficient. For the inflow case it was found that due to the favorable pressure gradient the differences between the three models studied increases significantly as the Kn number increases and according to that three Kn number regions can be established. In the outflow case the difference between the no-slip model and the two slip models is much smaller. But as $Re{\cdot}\alpha$ parameter becomes larger, at relatively large *Kn* numbers, the adverse pressure gradient causes the flow at the wall to separate at $Re{\cdot}\alpha$ values lower than 10.31. This is predicted only by the second order velocity-slip model so for outflow cases near the separation flow region the second order velocity-slip model should always be used. It was also found that increasing the *Kn* number decreases the skin friction coefficient calculated using the two velocity-slip models in all cases except for when separation occurs, as when the velocity at the wall is reversed this factor increases.

In the second part, the effect of adding the second order term to the velocity-slip/temperature-jump boundary condition has on the solution of four cases in which the driving force is fluctuating was examined. The study concentrated on comparing the effect frequency has on the velocity and temperature solutions at given *Kn* number using the first and the second order slip/jump models. It is found that, at a given *Kn* number value, increasing the driving force frequency increases the difference between

the first and second order models. It was found that the critical frequency for which the second order velocity-slip model should be used instead of the first order depends on the *Kn* number and also on the type of the flow driving force.

In the third part, the Fanno flow problem has been studied using both, first order and second order velocity-slip boundary conditions models and then compared to the no-slip boundary conditions solution. The study concentrates on investigating the effect the change of *Kn* number has on the velocity profiles, magnitude of slip at the wall, skin friction coefficient C_f and the L_{max}/D factor characteristic of Fanno line. It is found that the slip increases as the Kn increases and the skin friction coefficient decreases. Also as the *Kn* number increases, the friction coefficient *f* decreases, this reduction in friction leads to increase of the *L/D* parameter for both supersonic and subsonic flows with slip when compared to the no-slip solution. Overall, it is concluded that for an adiabatic compressible flow in circular microchannel, for $Kn \leq 0.01$ there is no need to apply any velocity-slip model as the no-slip model will give sufficiently accurate predictions. As for the range $0.01 \leq Kn \leq 0.1$, the first order velocity slip model should be applied, and that for this range, there is no necessity to use the second order velocity-slip model.

Chapter One

Introduction

1.1 Prologue

In the recent years the industry, driven by the constant quest for miniaturization of gadgets and machines, has developed a number of manufacturing processes that can create extremely small electronic and mechanical components. This has led to the increase of interest in the micro-scale fluid and heat transfer research. It was observed that in such small devices the fluid flows differ from those in macroscopic machines and cannot always be predicted from conventional flow models such as the Navier-Stokes equations with no-slip boundary condition at a fluid-solid interface. Slip flow, thermal creep, rarefaction, viscous dissipation, compressibility, intermolecular forces and other unconventional effects may have to be taken into account. For gases, micro-fluid mechanics has been studied by incorporating slip boundary conditions, thermal creep, viscous dissipation as well as compressibility effects into the continuum equations of motion, but it has a number of limitations. Molecular-based models have also been attempted for certain ranges of the operating parameters.

These small devices for which the characteristic length falls in the range between 1 mm and 1 micron are usually referred to as microelectromechanical systems (MEMS). Some of them are very complex systems that combine electrical and mechanical components. These small devices are usually manufactured using integrated circuit batch-processing technologies such as surface silicon micromachining; bulk silicon micromachining; lithography, electrodeposition and plastic molding and electrodischarge machining

(EDM) [16]. Yet smaller devices are being developed with an overall dimension of less than a1 micron, these are referred to as nanodevices (or NEMS). Applications of such small devices can nowadays be found in the electronic industries, for example ink jet printing where micropumps deliver picoliters of ink through microscopic nozzles. Another potential application is in electronic equipment cooling, scientists are experimenting on micro heat sinks which can be integrated into the chips to cool the new power hungry microprocessors. There is also work on potential medical applications as the development of an artificial pancreas.

When experimental work was conducted on a number of such small devices in was noticed that the fluid flow behavior differ from that in macro machines. When scientists tried to apply the same principles for conventional flows such as the Navier-Stokes equations with no-slip boundary condition at a fluid-solid interface to microscopic equipment as microscopic ducts, nozzles or valves, there was difference between the theoretical and the experimental data obtained. One such example is the measured flowrate in a long pipe which was observed to be higher than that predicted from the conventional continuum flow model.

This difference in results started a search for a suitable model for dealing with flow in micro devices. One of the major factors that lead to such a difference is the surface effect which is dominant in such small devices. Depending on the size of the micro device, the surface-to-volume ratio can be millions of times larger than that for a macro device. This increase in surface area relative to the mass of the micro device noticeably affects the transport of mass, momentum and energy through the surface. For some very small devices the continuum approach altogether can fail. In such a small devices slip flow, thermal creep, rarefaction, viscous dissipation, compressibility and intermolecular forces all start to play significant role and may have to be taken into account preferably

using only first principles such as conservation of mass, Newton's second law, conservation of energy, etc.

When characterizing the flow in a particular device the best way is to begin by computing the typical Reynolds, Mach and Knudsen numbers. For example, gas flows in micro devices is usually studied by applying the continuum equations of motion with slip boundary conditions and also taking into account the thermal creep, viscous dissipation and compressibility effects.

For some cases and operating ranges where the continuum approach fails a number of molecular based models have been proposed and tried. In such cases, molecular dynamics simulations seem to be the only first-principle approach available to characterize liquid flows in microdevices. One of the famous molecular models is the direct simulation Monte Carlo (DSMC) method which is based on a kinetic formulation and is valid for all flow regimes. However these models require huge processing power and their convergence is very slow and sensitive, so they are hardly practical solution

1.2 Literature Review:

Following is a review of some of the work, theoretical and experimental, published in the microchannel flow research area. Most of these publications have come out in the last five years as the topic is still considered to be new and constantly evolving.

An interesting review papers on the topic is Gad-Al-Hak (1999) "The Fluid Mechanics of Microdevices-The Freeman Scholar Lecture" which serves as an excellent introduction into the microelectromechanical systems (MEMS) research area. It explains the phenomena of fluid flow in microdevices and the different flow regimes in

micro-domains. It also summarizes the important parameters and the governing equations applicable in micro-flows. The paper also emphasizes the use of MEMS as sensors and actuators for flow diagnosis and control.

Other good review papers of the research in the microchannel flow area were published by Obot (2002) and by Celata (2004). Another work presenting an interesting historical overview and deeper physical understanding of the slip boundary condition has been published by Lauga (2005).

Michael J. Martin and Iain D. Boyd (2001) studied the effect slip condition has on the Blasius Boundary Layer Solution. Their results showed that the boundary layer equations can be used to study flow at the MEMS scale, and to judge when non-equilibrium effects become important. While the self-similarity of the Blasius boundary layer is lost, the boundary layer equations continue to provide useful information to study the effects of rarefaction on the shear stress and structure of the flow. They also show the weakness of using a simple geometric Knudsen number in describing the flow, and provide a new flow parameter, K_1, for describing non-equilibrium behavior. Navier-Stokes flow solvers, incorporating the effects of slip conditions at the boundary, have been used to study the accuracy of these solutions for flow over thin flat plates. These results were used to evaluate test conditions for an experimental study of MEMS scale airfoils. Based on the results of their work, and additional computational studies, suggest that the reduction in drag due to these effects should be measurable for flat plates with chords of 10-40μm, at pressures ranging from 0.1 to 1.0 atmospheres.

Asako et al. (2003) studied the Effect of compressibility on gaseous flows in micro-channels. They solved two-dimensional compressible momentum and energy equations in a parallel plate channel to obtain the effect of compressibility on gaseous flow

characteristics in micro-channels. The computations were performed for a wide range of *Reynolds* number and *Mach* number and for both no-heat-conduction, and isothermal flow conditions. From their work it was concluded that both *Fanning* and *Darcy* friction factors are function of the *Mach* number and they differ from the incompressible value of 96 for parallel-plate ducts. The effect of stagnation pressure and temperature on the friction factors is small. Their values for two cases of big differences of pressure and temperature varied by about only 2%.

More recently, Haddad et al. (2005) investigated theoretically the effect of frequency of fluctuation of the driving force on velocity slip and temperature jump at the wall(s) for four cases of basic gas micro-flow problems. The cases they considered were the transient Couette flow, the pulsating Poiseuille flow, the Stoke's second problem flow and the transient natural convection flow. The formulation of the problem had revealed that the controlling parameter of the problem is a combination of Knudsen number (Kn) and frequency of fluctuation (ω) in the form of an effective Knudsen number, $Kn_{eff} = \sqrt{\omega}Kn$, that replaced the usual Knudsen number (Kn), and consequently the slip flow regime was found to be valid when $10^{-3} \leq Kn_{eff} \leq 10^{-1}$. They also found that when the frequency is small the velocity and temperature profiles are similar to the corresponding classical macro-flow profiles at zero frequency. Also, the slip in velocity and the jump in temperature increase as the Knudsen number and/or the frequency of the driving force increases. In addition, the slip in velocity and the jump in temperature were found to be negligible when the frequency and/or Kn are sufficiently small. Another work concerned with the effect of slip in oscillating walls in Couette flow and Stoke's second problem has been published by Khaled and Vafai (2004).

In another work, Toh et al. (2002) performed a numerical study of fluid flow and heat transfer in microchannels. The heat transfer inside four microchannels heat sinks has been presented. The local thermal resistance has also been well predicted for a situation where experimental data is available. The numerical procedure correctly predicted the location of the maximum thermal resistance and the drop (due to axial heat spreading) in the thermal resistance towards the trailing edge of the heater. The friction factor has also been predicted in this study. It was found that the heat input lowers the frictional losses, particularly at lower Reynolds numbers. At lower Reynolds numbers the temperature of the water increases, leading to a decrease in the viscosity and hence smaller frictional losses.

Ambatipudi and Rahman (2000) performed an analysis of conjugate heat transfer in microchannel heat sinks. They numerically investigated the heat transfer in a silicon substrate containing rectangular microchannels by developing an exact model for a device that was fabricated using silicon. Equations governing the conservation of mass, momentum, and energy were solved in the fluid region (microchannels). Within the solid wafer, the heat conduction was solved. The effects of channel aspect ratio, *Reynolds number*, and number of channels on the thermal performance of the device was investigated. It was found that the *Nusselt number* is more for a system with a larger number of channels and larger *Reynolds number*. For *Re = 673*, the optimum channel depth that maximizes *Nusselt number* occurred at *300μm*. This interesting behavior of *Nusselt number* variation is the result of competing effects of thermal resistance inside the solid and that at the solid/fluid interface. When the Reynolds number and channel width are constant, the pressure drop is inversely proportional to the depth of the channel. Increasing the number of channels increased the local Nusselt number along the entire length of the channel.

In an example on experimental work in microchannels, Araki et al. (2002) performed an experimental investigation of gaseous flow characteristics in microchannels. They investigated frictional characteristics of nitrogen and helium flows in three different microchannels with hydraulic diameter range of between *3–10 μm*. The frictional resistance of gaseous flow in a trapezoidal cross-section microchannel was observed to be smaller than that in the conventional-sized channel. The reduced frictional resistance in microchannels is caused by the rarefaction effect due to extremely small dimensions of flow passages. By using Maxwell's first-order slip boundary condition, they predicted the mass flow rate through microchannels and the friction constant.

Another experimental work was done by Gao et al. (2002) who carried out an investigation of the flow and the associated heat transfer in two-dimensional microchannels. Their results were affected by a significant scatter, owing to the various conditions used in the experiments, and, most likely, owing to the difficulty of measurements at micronic scales. The present facility was designed to modify easily the channel height *e*. It was then possible to investigate hydrodynamics and heat transfer in channels of height ranging from 1 mm, which corresponds to conventional size, up to *0.1 mm*, where size effects are expected. Size effects were therefore tested in the same set-up and with the same channel walls for all the experiments, which were carried out with demineralized water. Measurements of the overall friction coefficient and of local *Nusselt numbers* show that the classical laws of hydrodynamics and heat transfer are verified for $e > 0.4$ *mm*. For lower values of *e*, a significant decrease of the *Nusselt number* is observed whereas the *Poiseuille number* keeps the conventional value of laminar developed flow. The transition to turbulence is not affected by the channel size.

Pettersen (2004) studied experimentally the two-phase flow patterns in microchannel vaporization of CO_2 at near-critical pressure. A special test rig was built in order to

observe two-phase flow patterns. The observations showed a dominance of intermittent (slug) flow at low *x* and wavy annular flow with entrainment of droplets at higher *x*. Stratified flow was not observed in the tests with heat load. Bubble formation and growth could be observed in the liquid film, and the presence of bubbles gave differences in flow pattern compared to adiabatic flow. The flow pattern observations on CO_2 did not fit any of the generalized maps or transition lines. Compared to small-diameter observations with air/water at low pressure, the transition into annular flow occurred at a much lower superficial vapor velocity (superficial velocity of approximately $0.5ms^{-1}$). The observed inception of entrainment at $0.5–0.6\ ms^{-1}$ superficial vapor flow velocity was close to the predicted onset at $0.4\ ms^{-1}$.

Another examples of experimental work published on the topic of micro-flow are the papers by Arkilic et al. (2001), Chen et al. (2004) and Nishio (2004). Roy et al. (2003) published a work that used both theoretical and experimental techniques for modeling of gas flow in microchannels and nanopores.

Also a fair amount of work has been done using molecular-dynamics and probabilistic models. One of the famous is the direct simulation Monte Carlo (DSMC) method (Alexeenko, et al. (2005), Faghri and Sun (2003), Tzeng and Chen (2003)) which is based on a kinetic formulation and is valid for the entire range of *Kn* numbers. Another molecular model used by Tretheway et al. (2002) for gas flow behavior investigation is the Lattice Boltzmann Simulation. The main problem with these models is that they require huge processing power and their convergence is very slow and sensitive, so they are hardly practical solution.

In this work, three different cases that cover different flow patterns in microchannels will be studied by implementing the first and second order velocity-slip/temperature

jump models in order to observe the behavior of the flow so that a certain criteria for the use of each of the no-slip, the first order slip and the second order slip models. These three cases are; the Jeffery-Hamel flow in microchannels, Fanno flow in circular microchannels and basic fluctuating flows in microchannels. The fluctuating flows cases are the same four cases studied by Haddad et al. (2005) only this time the second order slip/jump model will be used and the results compared to the results for the first order model.

Chapter Two

Micro-Flow Governing Equations

As mentioned earlier, in the literature there are two ways used for modeling a flow field, either the molecular based model or the continuum approach where the matter is assumed continuous and indefinitely divisible. The continuum model, which is traditionally applied for fluid flows, is represented by the Navier-Stokes equations. This model ignores the molecular nature of gases and liquids and treats the fluid as a continuous medium describable in terms of the macroscopic flow quantities such as spatial and temporal variations of density, velocity, pressure, and temperature.

In the current work we are going to use the second, continuum model for which the equations are the continuity, momentum and energy conservation principles, which are introduced below:

$$\frac{\partial \rho}{\partial t} + \frac{\partial}{\partial x_k}(\rho u_k) = 0 \tag{2.1}$$

$$\rho\left(\frac{\partial u_i}{\partial t} + u_k \frac{\partial u_i}{\partial x_k}\right) = -\frac{\partial p}{\partial x_i} + \rho g_i + \frac{\partial}{\partial x_k}\left[\mu\left(\frac{\partial u_i}{\partial x_k} + \frac{\partial u_k}{\partial x_i}\right) + \delta_{ki}\Lambda\frac{\partial u_j}{\partial x_j}\right] \tag{2.2}$$

$$\rho c_v\left(\frac{\partial T}{\partial t} + u_k \frac{\partial T}{\partial x_k}\right) = \frac{\partial}{\partial x_k}\left(k\frac{\partial T}{\partial x_k}\right) - p\frac{\partial u_k}{\partial x_k} + \varphi \tag{2.3}$$

$$\varphi = \frac{1}{2}\mu\left(\frac{\partial u_i}{\partial u_k} + \frac{\partial u_k}{\partial x_k}\right)^2 + \lambda\left(\frac{\partial u_j}{\partial x_j}\right)^2 \tag{2.4}$$

The first equation, Eq.(2.1) is the continuity (conservation of mass) equation. The three components of Eq.(2.2) are the conservation of momentum (Navier-Stokes) equations for a Newtonian fluid. The third equation, Eq.(2.3), is the conservation of thermal

energy equation In it φ is the dissipation function expressing the irreversible conversion of mechanical energy to internal energy as a result of the deformation of the fluid element. It is given in Eq.(2.4) from which it can be seen that this term is always positive as required by the Second Law of thermodynamics. The second term on the right-hand side of Eq.(2.3) is the reversible work done by the pressure as the volume of a fluid material element changes.

In order to be able to solve the above equations for a certain flow situation we need to apply a number of initial and boundary conditions. If dealing with a traditional macro flow case these conditions are the no-slip boundary condition at the fluid-solid interface which is applied to the momentum equation and the no-temperature-jump condition is applied to the energy equation.

Since the continuum model is better known and is mathematically easier to handle than alternative molecular models it should be used as long as it is applicable. That is why in recent years there has been extensive examination of the validity of the Navier-Stokes equations for the new cases that face the scientists. This examination work can be done both theoretically and experimentally.

All this work has shown that the continuum model is fairly accurate as long as local properties such as density and velocity can be defined as averages over elements large compared with the microscopic structure of the fluid but small enough in comparison with the scale of the macroscopic phenomena to permit the use of differential calculus to describe them. Additionally, the flow must not be too far from thermodynamic equilibrium. [16]

In order to obtain satisfactory results, the shear stress and heat flux must be expressed in terms of lower-order macroscopic quantities such as velocity and temperature, and the

linear relations are valid only when the flow is near thermodynamic equilibrium. What further complicates the matter is that the classical no-slip boundary condition at the solid-fluid interface becomes inapplicable before the linear stress-strain relation becomes invalid.

Here the *Knudsen number* definition has to be introduced as the ratio between the mean free path (λ) and the characteristic length (L) and is generally the most important parameter determining the flow regime. The different Knudsen number regimes are specific for each geometry and flow configuration and so they are determined empirically only to serve as a general guidelines for the use of the different models.

For gases, the mean free path λ is defined as the average distance traveled by molecules between consecutive collisions. If an ideal gas is assumed its molecules can be modeled as rigid spheres, a relation for the mean free path in terms of temperature T and pressure p can be given in the form

$$\lambda = \frac{1}{\sqrt{2}\pi n \sigma^2} = \frac{kT}{\sqrt{2}\pi p \sigma^2} \tag{2.5}$$

where n is the number density (number of molecules per unit volume), σ is the molecular diameter, and k is the Boltzmann constant. Based on this definition, the continuum approach is applicable as long as characteristic flow dimension L is much larger than the mean free path for the gas λ. If this condition is violated, the flow departs from the equilibrium and the linear relation between stress and strain rate and the no-slip velocity condition are no longer valid. Also the linear relation between heat flux and temperature gradient and the no-jump temperature condition at a solid-fluid interface are no longer accurate when L is much larger than the mean free path for the λ.

The characteristic length L can be some overall dimension of the flow geometry, but a more precise choice is the scale of the gradient of a macroscopic quantity, as for example the density ρ,

$$L = \frac{\rho}{\left|\frac{\partial \rho}{\partial y}\right|} \tag{2.6}$$

This all bring us to the definition of the *Knudsen number* as the ratio between the mean free path and the characteristic length as shown in the equation below

$$Kn = \frac{\lambda}{L} \tag{2.7}$$

It has been shown that the traditional continuum approach validity can be extended by modifying the boundary conditions for *Kn* number values as high as 0.1.

Another two very important dimensionless parameters in fluid mechanics are the Reynolds number and the Mach number, and the Knudsen number can be expressed in terms of those two. The Reynolds number is the ratio of inertial forces to viscous forces as shown:

$$Re = \frac{V_0 L}{\nu} \tag{2.8}$$

where V_o is a characteristic velocity and ν is the kinematic viscosity of the fluid. On the other hand, the Mach number is the ratio of flow velocity to the speed of sound in the fluid

$$Ma = \frac{V_0}{a_0} \tag{2.9}$$

The Mach number can be considered a dynamic measure of fluid compressibility or as the ratio of inertial forces to elastic ones. Using the kinetic theory of gases, a relation between the mean free path and the viscosity can be given as follows:

$$\nu = \frac{\mu}{\rho} = \frac{1}{2}\lambda\bar{v}_m \tag{2.10}$$

where μ is the dynamic viscosity, and $\bar{v}_m$ is the mean molecular speed which is given as follows,

$$\bar{v}_m = \sqrt{\frac{8}{\pi\gamma}}\, a_0 \tag{2.11}$$

where γ is the specific heat ratio (i.e. the isentropic exponent). As it can be seen, this velocity $\bar{v}_m$ is higher than the sound speed a_o. Combining Eq. (2.7) – (2.11), the required relation for *Kn* is given as:

$$Kn = \sqrt{\frac{\pi\gamma}{2}}\frac{Ma}{Re} \tag{2.12}$$

For boundary layer flows, the characteristic length-scale is the shear-layer thickness δ, which for laminar flows can be expressed as

$$\frac{\delta}{L} \sim \frac{1}{\sqrt{Re}} \tag{2.13}$$

$$Kn \sim \frac{Ma}{Re_\delta} \sim \frac{Ma}{\sqrt{Re}} \tag{2.14}$$

where Re_δ is the Reynolds number based on the free stream velocity V_o and the boundary layer thickness δ, while *Re* is based on V_o and the stream wise length-scale *L*.

The different Knudsen number regimes are specific for each geometry and flow conditions and by so are empirically determined only as an approximate guide. For the Knudsen number region close to zero, the transport terms in the continuum momentum and energy equations are negligible and so the Navier-Stokes equations are reduced to the inviscid Euler equations. At this region heat conduction and viscous diffusion and dissipation are both negligible, and the flow can be assumed isentropic (i.e., adiabatic

and reversible) from the continuum viewpoint. On the other hand the equivalent molecular viewpoint is that the velocity distribution function is everywhere of the local equilibrium or Maxwellian form. For larger *K*n numbers regime, rarefaction effects become significant, and the continuum approach becomes useless. Based on a number of experimental and theoretical works, it has been established that the traditional no-slip/no-jump boundary conditions gives accurate results for the range of $Kn<0.001$. At larger values of *Kn* the assumption of equilibrium at the fluid-solid interface is no longer true and some velocity-slip and temperature-jump occurs so the model has to be modified in order to take then into consideration. The flow in microchannels falls into the later category so for it the modified velocity-slip/temperature-jump models should be used. Navier-Stokes equation with first order velocity-slip/temperature-jump are considered to be applicable for the range between $0.001<Kn<0.1$. For the transition region which falls in the range between $0.1<Kn<10$ there are two options, either using the Navier-Stokes equations which can still be applied if second or higher order slip/jump boundary conditions are applied, or use one of the molecular-based models. After gad Al-Hak (1999) the different Knudsen number regimes can be summarized as follows: [14, 15]

Euler equations (neglect molecular diffusion)	$Kn \rightarrow 0\ (Re \rightarrow \infty)$
Navier-Stokes equations with no-slip boundary conditions	$Kn \leq 10^{-3}$
Navier-Stokes equations with slip boundary conditions	$10^{-3} \leq Kn \leq 10^{-1}$
Transition regime	$10^{-1} \leq Kn \leq 10$
Free-molecule flow	$Kn > 10$

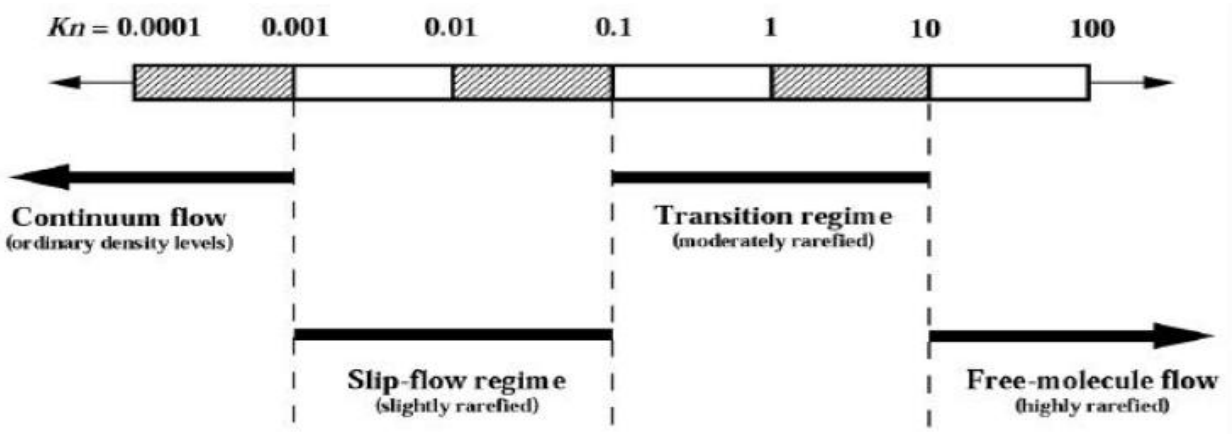

Fig.2.1 Knudsen number regimes. [17]

Usually, the no-velocity-slip at the wall boundary condition is applied to the momentum equation while no-temperature-jump boundary condition is applied to the energy equation. But these two boundary conditions are applicable only if the fluid flow and the wall are at thermodynamics equilibrium. In order for this equilibrium to exist, there has to be an infinitely high frequency of collisions between the fluid particles and the solid surface. In practice, for the cases of gas flows, for the region of Kn<0.001 this condition is satisfied and the no-slip/no-jump model gives accurate results. But for Kn numbers higher than that, the gas becomes too rarefied and the collision frequency is not high enough to ensure equilibrium so the boundary conditions must be modified to accommodate the velocity-slip/temperature-jump that takes place. Since flow in microchannels is usually modeled using the velocity-slip/temperature-jump model, next the appropriate boundary conditions will be introduced.

In both liquid and gasses, for the linear Navier boundary condition the tangential velocity slip at the wall $\Delta u|_w$ and the local shear are related as following:

$$\Delta u|_w = u_{fluid} - u_{wall} = L_s \frac{\partial u}{\partial y}\Big|_w \tag{2.15}$$

where L_s is the constant slip length, and $\partial u/\partial y\big|_w$ is the strain rate computed at the wall. If a force balance is applied on a gas element near to the wall, the following relation for the slip velocity can be obtained

$$u_{gas} - u_{wall} = \lambda \frac{\partial u}{\partial y}\Big|_w \tag{2.16}$$

where λ is the molecule mean free path. The right-hand side can be considered to be the first term in an infinite Taylor series, sufficient if the mean free path is small enough. However, for real walls, some of the molecules are reflected diffusely while some are reflected specularly.

In order to take this into consideration, a tangential-momentum-accommodation coefficient σ_v has to be defined as the fraction of molecules reflected diffusively. This coefficient depends on the fluid, the solid and the surface finish, and is found experimentally to be between 0.2-0.8. The lower limit represents exceptionally smooth surfaces while the upper limit is typical for most practical surfaces. Thus the final expression for the velocity-slip for an isothermal wall as derived by Maxwell (1879) becomes

$$u_{gas} - u_{wall} = \frac{2-\sigma_v}{\sigma_v} \lambda \frac{\partial u}{\partial y}\Big|_w \tag{2.17}$$

When $\sigma_v=0$ the slip velocity is unbounded, while when $\sigma_v=1$ equation (2.17) reverts to equation (2.16). For the case of ideal gas flow under the effect of wall-normal and tangential temperature gradients, the complete slip-flow and temperature-jump boundary conditions as given by Smoluchowski (1898) are

$$u_{gas} - u_{wall} = \frac{2-\sigma_v}{\sigma_v} \lambda \frac{\partial u}{\partial y}\Big|_w + \frac{3}{4} \frac{\mu}{\rho T_{gas}} \frac{\partial T}{\partial x}\Big|_x \tag{2.18}$$

$$T_{gas} - T_{wall} = \frac{2-\sigma_T}{\sigma_T}\left(\frac{2\gamma}{\gamma+1}\right)\frac{\lambda}{Pr}\frac{\partial T}{\partial y}\Big|_w \tag{2.19}$$

where x and y are the streamwise and normal coordinates, ρ and μ are the fluid density and viscosity respectively, T_{gas} is the temperature of the gas adjacent to the wall, T_{wall} is the wall temperature, τ_w is the shear stress at the wall, Pr is the Prandtl number and γ is the gas specific heat ratio. The tangential-momentum-accommodation coefficients σ_v and the thermal-accommodation coefficient σ_T are given by

$$\sigma_v = \frac{\tau_i - \tau_r}{\tau_i - \tau_w} \tag{2.20}$$

$$\sigma_{T} = \frac{dE_i - dE_r}{dE_i - dE_w} \tag{2.21}$$

where the subscripts i, r and w stand for incident, reflected and solid wall conditions respectively, τ is tangential momentum flux and dE is an energy flux.

While the Navier-Stokes equation with the first order velocity-slip/temperature-jump boundary conditions are applicable to the range between $0.001 < Kn < 0.1$, for higher values of Kn second-order or higher velocity-slip/temperature-jump boundary conditions should be applied to the Navier-Stokes equation if it is to be used in the transition region (the range between $0.1<Kn<10$). For example, for the isothermal wall case, a higher-order slip velocity condition has been proposed by Beskok (1994) in the form

$$u_{gas} - u_{wall} = \frac{2-\sigma_v}{\sigma_v}\left(\lambda\frac{\partial u}{\partial y}\Big|_w + \frac{\lambda^2}{2!}\frac{\partial^2 u}{\partial y^2}\Big|_w + \frac{\lambda^3}{3!}\frac{\partial^3 u}{\partial y^3}\Big|_w + \cdots\right) \tag{2.22}$$

In similar manner a higher-order temperature-jump boundary condition has been derived by Beskok (1996) for which the Taylor series in dimensionless form looks like this:

$$T^*_{gas} - T^*_{wall} = \frac{2-\sigma_T}{\sigma_T}\left(\frac{2\gamma}{\gamma+1}\right)\frac{1}{Pr}\left(Kn\left.\frac{\partial T^*}{\partial y^*}\right|_w + \frac{Kn^2}{2!}\left.\frac{\partial^2 T^*}{\partial y^{*2}}\right|_w + \cdots\right) \quad (2.23)$$

Implementing the above high-order boundary conditions in numerical simulations is rather difficult since second and higher order derivatives of velocity and temperature cannot be accurately computed at the wall. That's why a number of scientists have proposed alternative higher-order boundary conditions derived using asymptotic analysis using high-order slip coefficients determined from the presumably known no-slip solution which avoids the computational difficulties associated with the above equations.

Chapter Three

Mathematical Formulation and Solution Methods

In this chapter, the mathematical formulation and analysis for the three cases will be derived and solved by implementing the first and second order velocity-slip/temperature jump models in order to observe the behavior of the flow so that a certain criteria for the use of each of the no-slip, the first order slip and the second order slip models. These three cases are; the Jeffery-Hamel flow in microchannels, four basic fluctuating flows in microchannels and Fanno flow in microchannels.

3.1. Jeffery-Hamel Flow in Microchannels

In this first section the effect of implementing the velocity-slip boundary conditions on the case of radial flow caused by a line source or sink is investigated. This problem was first discussed by Jeffery (1915) and independently by Hamel (1917) and so the name. Up to our knowledge, so far Jeffery-Hamel flow has not been investigated in micro-domains. The objective is to investigate the effect of both the first order and the second order slip models on the hydrodynamic behavior of micro-convergent/divergent channels. This is attained by establishing criteria that justifies the use of the first order slip model instead of the second order slip model.

3.1.1 Governing Equations

Referring to the schematic diagram shown in Fig.1, the flow is considered in polar coordinates *(r, θ),* generated by a source (or sink) at the origin and bounded by solid walls at $\theta = \pm\alpha$.

Assuming that the flow is purely radial, $u_\theta = 0$ and from the continuity equation in polar coordinates for a steady incompressible flow with constant properties is reduced to:

$$\frac{1}{r}\frac{\partial}{\partial r}(ru_r) = 0, \qquad \text{or} \qquad ru_r = fcn(\theta) \tag{3.1}$$

It is expected that u_r will have a local maximum $u_{max,}$ at $\theta = 0$. Then a convenient nondimensionalization for this problem is [42]

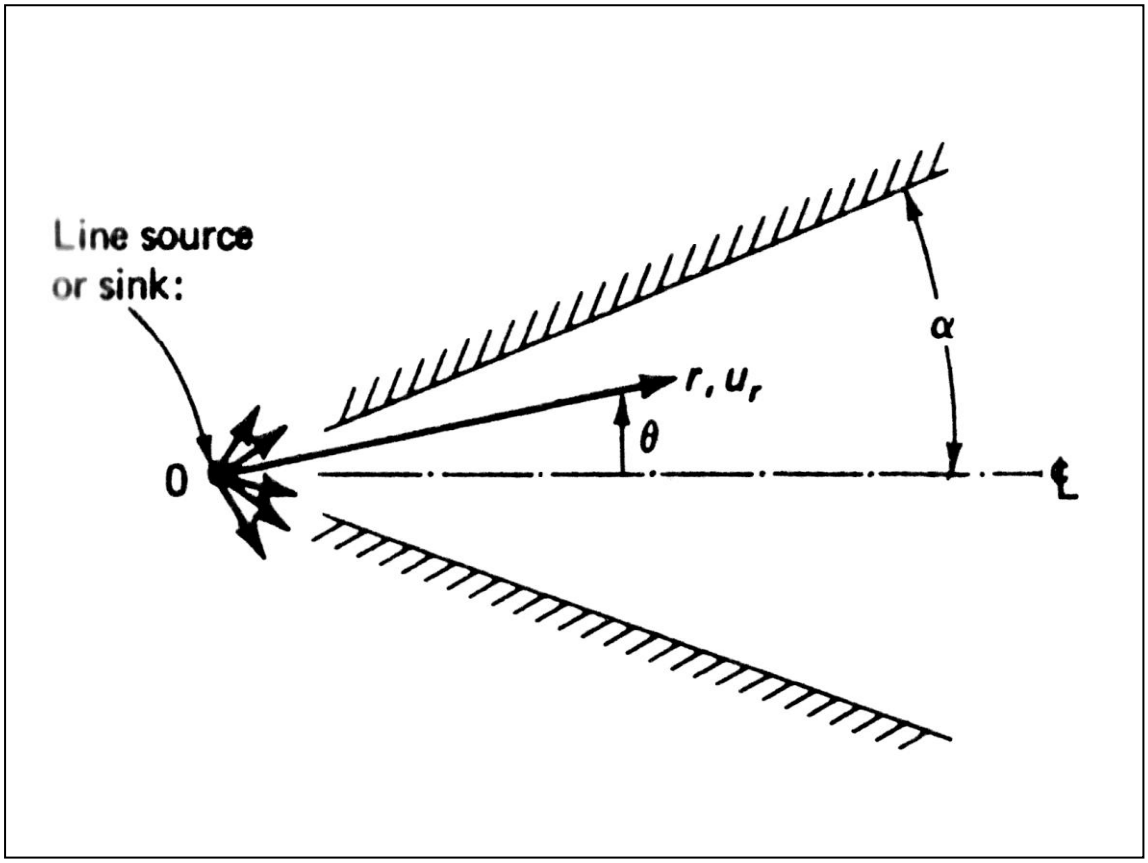

Figure 3.1: Jeffery-Hamel flow problem schematic diagram. [42]

$$\eta = \frac{\theta}{\alpha}, \qquad \frac{u_r}{u_{max}} = f(\eta) \tag{3.2}$$

The momentum equations in polar coordinates, for $u_\theta = 0$, are

$$u_r\frac{\partial u_r}{\partial r} = -\frac{1}{\rho}\frac{\partial p}{\partial r} + \nu\left(\frac{\partial^2 u_r}{\partial r^2} + \frac{1}{r}\frac{\partial u_r}{\partial r} - \frac{u_r}{r^2} + \frac{1}{r^2}\frac{\partial^2 u_r}{\partial \theta^2}\right) \tag{3.3.a}$$

$$0 = -\frac{1}{\rho r}\frac{\partial p}{\partial \theta} + \frac{2\nu}{r^2}\frac{\partial u_r}{\partial \theta} \tag{3.3.b}$$

3.1.2 Solution

The pressure can be eliminated by cross-differentiation and introducing the variables η and $f(\eta)$. The result is a third-order nonlinear differential equation for f

$$f''' + 2Re \cdot \alpha f f' + 4\alpha^2 f' = 0 \tag{3.4}$$

Where the characteristic Reynolds number of the flow is defined as

$$Re = \frac{u_{max}\, r\alpha}{\nu} \tag{3.5}$$

The boundary conditions are assumed symmetric flow with a maximum at the centerline:

$$f(0) = 1 \tag{3.6}$$

and the velocity-slip boundary conditions at the wall are:

for the first order slip mode $f(-1) = f(+1) = -\frac{2-\sigma_v}{\sigma_v} Kn \cdot f'(1)$ (3.7.a)

and for the second order model $f(-1) = f(+1) = -\frac{2-\sigma_v}{\sigma_v}\left(Kn \cdot f'(1) + \frac{Kn^2}{2} \cdot f''(1)\right)$ (3.7.b)

Where the characteristic Knudsen number of the flow is defined as

$$Kn = \frac{\lambda}{r\alpha} \tag{3.8}$$

The condition given in Eq. (3.6) can be replaced by the symmetry requirement $f'(0) = 0$ and confine the analysis to the upper half of the wedge region. Since Eq. (3.4) is nonlinear, it is next solved numerically by reducing it to a system of first order equations:

$$F_0'(\eta) = F_1(\eta) \tag{3.9.a}$$

$$F_1'(\eta) = F_2(\eta) \tag{3.9.b}$$

$$F_2'(\eta) = -2Re\alpha \cdot F_0(\eta)F_1(\eta) - 4\alpha^2 \cdot F_1(\eta) \tag{3.9.c}$$

with the boundary conditions as following:

$$F_0(0) = 1 \tag{3.10.a}$$

$$F_1(0) = 0 \tag{3.10.b}$$

$$F_0(1) = -\frac{2-\sigma_v}{\sigma_v} Kn \cdot F_1(1), \quad \text{or} \quad F_0(1) = -\frac{2-\sigma_v}{\sigma_v}\left(Kn \cdot F_1(1) + \frac{Kn^2}{2} \cdot F_2(1)\right) \tag{3.10.c}$$

Another parameter that is to be studied here is the skin friction coefficient C_f which depends on the shear at the wall τ_w which is defined as

$$\tau_w = -\mu \frac{\partial u}{\partial y} \tag{3.11}$$

where *y* is the normal to the wall.

Eq. 3.11 is then rewritten in dimensionless form in terms of C_f and *Re* as following:

$$C_f = -\frac{2}{Re} f'(\eta) \quad \text{at} \quad \eta = 1 \tag{3.12}$$

The solution of Eq.(3.9) and (3.10) for a range of $Re{\cdot}\alpha$ and *Kn* numbers gives the velocity profiles plots, and the solution of Eq.(3.12) gives the skin friction coefficient. From these results the differences among the three models are found for the specified range of *Kn* numbers. Also the separation (reversal) of the flow concept is further investigated.

3.2 Basic Gaseous Fluctuating Micro-Flows

In this part, the effect of adding the second order term to the velocity-slip/temperature-jump boundary conditions on the solution of four cases in which the driving force is fluctuating harmonically is studied. The four cases are the transient Couette flow, the pulsating Poiseuille flow, the Stoke's second problem and the transient natural convection flow. So far fluctuating flow in micro-domains has been investigated only by

Haddad et al. (2005) but only using the first order velocity-slip/temperature-jump boundary conditions, so the effect of adding the second order term to the velocity-slip/temperature-jump boundary condition has on the solution of these four cases will be examined and compared with the results for the first order model solution. The objective is to try and establish a certain criteria as for when using the more complicated model becomes viable.

3.2.1 Governing Equations

The scope of the present work should be to investigate the effect of the frequency (ω) of the driving force on the velocity-slip and temperature-jump at the wall for four different flow settings using the second order slip/temperature-jump model and compare it with the results for the first order slip/temperature-jump model from a previous works on the subject. The geometries for the four cases we are interested in are shown in Fig.3.2. The flow in all of them is laminar, incompressible flow of a Newtonian fluid with constant properties. Here we are only interested in the slip flow regime, which is for $10^{-3} \leq Kn \leq 10^{-1}$. These four cases are shown next.

3.2.1.1 - Case 1: Transient Couette gas flow between parallel plates with infinite length with one of the plates moving with fluctuating velocity ($u=sin(\omega t)$) in its plane and the other plate remaining stationary. The geometry of the problem is shown in Fig.(3.2.a) and the governing equations and boundary conditions for this case and the second order velocity-slip for this case are as following:

$$\frac{\partial U}{\partial \tau} = \frac{\partial^2 U}{\partial Y^2}, \tag{3.13}$$

with boundary conditions

$$U(\tau, 0) = \frac{2-\sigma_v}{\sigma_v}\left[Kn \left.\frac{\partial U}{\partial Y}\right|_{Y=0} + \frac{Kn^2}{2}\left.\frac{\partial^2 U}{\partial Y^2}\right|_{Y=0}\right] \tag{3.14}$$

$$U(\tau, 1) - \sin(\omega\tau) = -\frac{2-\sigma_v}{\sigma_v}\left[Kn \left.\frac{\partial U}{\partial Y}\right|_{Y=1} + \frac{Kn^2}{2}\left.\frac{\partial^2 U}{\partial Y^2}\right|_{Y=1}\right] \tag{3.15}$$

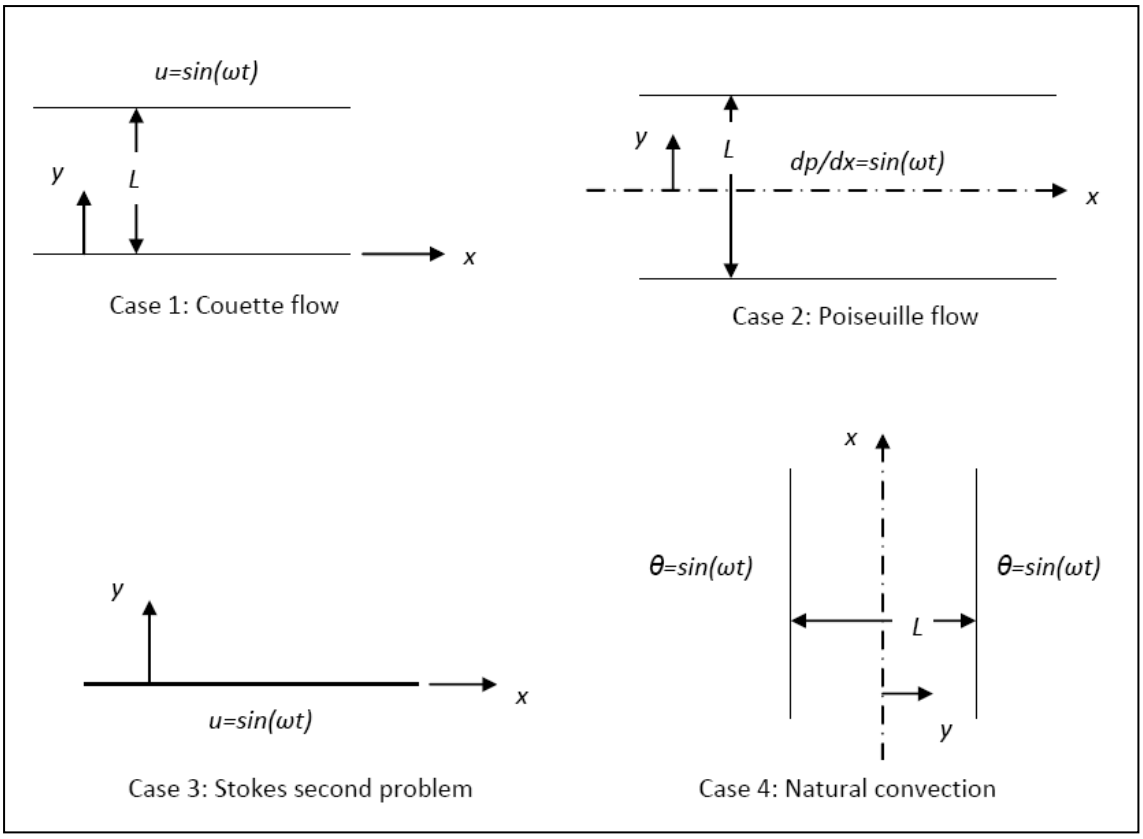

Figure 3.2: Basic gaseous fluctuating micro-flows schematic diagram

3.2.1.2 - Case 2: The pulsating Poiseuille gas flow between two infinite length parallel plates shown in Fig.(3.2.b). Here the plates are stationary while the driving pressure gradient is fluctuating in a sinusoidal manner (*dp/dx=sin(ωt)*). The governing equations and boundary conditions for this case for the second order velocity-slip at the walls and symmetry at the centerline are as following:

$$\frac{\partial U}{\partial \tau} = \sin(\omega\tau) + \frac{\partial^2 U}{\partial Y^2} \tag{3.16}$$

with boundary conditions

$$\frac{\partial U}{\partial Y}(\tau, 0) = 0 \tag{3.17}$$

$$U(\tau, 1) = -\frac{2-\sigma_v}{\sigma_v}\left[Kn\frac{\partial U}{\partial Y}\Big|_{Y=1} + \frac{Kn^2}{2}\frac{\partial^2 U}{\partial Y^2}\Big|_{Y=1}\right] \tag{3.18}$$

3.2.1.3 - Case 3: The Stokes second problem, shown in Fig.(3.2.c) involves a single plate of infinite length shaking in a sinusoidal manner ($u=sin(\omega t)$) in its own plane in an initially stationary fluid domain. The governing equations and boundary conditions for this case and the second order velocity-slip at the wall are as following:

$$\frac{\partial U}{\partial \tau} = \frac{\partial^2 U}{\partial Y^2} \tag{3.19}$$

with boundary conditions

$$U(\tau, 0) = \frac{2-\sigma_v}{\sigma_v}\left[Kn\frac{\partial U}{\partial Y}\Big|_{Y=0} + \frac{Kn^2}{2}\frac{\partial^2 U}{\partial Y^2}\Big|_{Y=0}\right] \tag{3.20}$$

$$U(\tau, \infty) = 0 \tag{3.21}$$

3.2.1.4 - Case 4: The transient natural convection gas flow between two vertical infinite length stationary parallel plates, which are subjected to fluctuating temperature variation ($\theta=sin(\omega t)$). The problem geometry is shown in Fig.(3.2.d) while the governing equations and boundary conditions for this case with the second order velocity-slip/temperature-jump at the wall, and symmetry conditions at the centerline are as following:

$$\frac{\partial U}{\partial \tau} = \frac{\partial^2 U}{\partial Y^2} + \theta \tag{3.22}$$

$$\frac{\partial \theta}{\partial \tau} = \frac{1}{Pr}\frac{\partial^2 \theta}{\partial Y^2} \tag{3.23}$$

with boundary conditions

$$\frac{\partial U}{\partial Y}(\tau, 0) = 0 \tag{3.24}$$

$$\frac{\partial \theta}{\partial Y}(\tau, 0) = 0 \tag{3.25}$$

$$U(\tau, 1) = -\frac{2-\sigma_v}{\sigma_v}\left[Kn\frac{\partial U}{\partial Y}\Big|_{Y=1} + \frac{Kn^2}{2}\frac{\partial^2 U}{\partial Y^2}\Big|_{Y=1}\right] \tag{3.26}$$

$$\theta(\tau,1)-\sin(\omega\tau)=-\frac{2-\sigma_v}{\sigma_v}\left(\frac{2\gamma}{1+\gamma}\right)\frac{1}{Pr}\left[Kn\frac{\partial U}{\partial Y}\Big|_{Y=1}+\frac{Kn^2}{2}\frac{\partial^2 U}{\partial Y^2}\Big|_{Y=1}\right] \quad (3.27)$$

Here, just like in the previous works, the flow will be assumed hydrodynamically fully developed, i.e. the change of U with X is zero ($dU/dX=0$). The change of temperature θ with respect to X is also zero ($d\theta/dX=0$).

3.2.2 Solution

After all the geometries, governing equations and boundary conditions are specified we proceed with obtaining the solutions for the four cases above. For these, an exact solution can be obtained by assuming the solution to be of the form:

$$U(\tau,Y)=Im\left[e^{i\omega\tau}V(Y)\right], \quad (3.28)$$

$$\Theta(\tau,Y)=Im\left[e^{i\omega\tau}W(Y)\right]. \quad (3.29)$$

Here, "*Im*" stands for the imaginary part of the assumed complex solution and $i=\sqrt{-1}$. By substituting this assumed solution in the governing equation for each case we find the four solutions to be as follows

Case 1: $$V(Y)=\frac{(1+m_2)sinh\left(\sqrt{i\omega}Y\right)+m_1 cosh(\sqrt{i\omega}Y)}{(m_1^2-m_2^2+1)sinh\left(\sqrt{i\omega}\right)+2m_1 cosh(\sqrt{i\omega})}, \quad (3.30)$$

Case 2**:** $$V(Y)=\frac{1}{i\omega}\left[1-\frac{\cosh(\sqrt{i\omega}Y)}{m_1\sinh(\sqrt{i\omega})+(1+m_2)\cosh(\sqrt{i\omega})}\right], \quad (3.31)$$

Case 3**:** $$V(Y)=\frac{e^{-\sqrt{i\omega}Y}}{1+m_1-m_2}, \quad (3.32)$$

Case 4**:**

$$V(Y)=\left\{\frac{1}{(i\omega-i\omega\,\mathrm{Pr})\left(n_1\sinh(\sqrt{i\omega\,\mathrm{Pr}})+(1+n_2)\cosh(\sqrt{i\omega\,\mathrm{Pr}})\right)}\right\}\cdot \left\{\frac{m_3\sinh(\sqrt{i\omega\,\mathrm{Pr}})+(1+m_4)\cosh(\sqrt{i\omega\,\mathrm{Pr}})}{m_1\sinh(\sqrt{i\omega})+(1+m_2)\cosh(\sqrt{i\omega})}\cosh(\sqrt{i\omega}Y)-\cosh(\sqrt{i\omega\,\mathrm{Pr}}Y)\right\} \tag{3.33}$$

and $$W(Y)=\frac{\cosh(\sqrt{i\omega Pr}\,Y)}{n_1\sinh(\sqrt{i\omega Pr})+(1+n_2\cosh(\sqrt{i\omega Pr})} \tag{3.34}.$$

where

$$m_1=\frac{2-\sigma_v}{\sigma_v}Kn\sqrt{i\omega},\qquad m_2=\frac{2-\sigma_v}{\sigma_v}\frac{Kn^2}{2}(i\omega),$$

$$m_3=\frac{2-\sigma_v}{\sigma_v}Kn\cdot\sqrt{i\omega Pr},\qquad m_4=\frac{2-\sigma_v}{\sigma_v}\frac{Kn^2}{2}(i\omega Pr),$$

$$n_1=\frac{2-\sigma_T}{\sigma_T}\left(\frac{2\gamma}{\gamma+1}\right)\frac{Kn}{Pr}\sqrt{i\omega Pr},\qquad n_2=\frac{2-\sigma_T}{\sigma_T}\left(\frac{2\gamma}{\gamma+1}\right)\frac{Kn^2}{2Pr}(i\omega Pr).$$

3.3 Fanno Flow in Microchannels

In this section the effect of implementing the velocity-slip boundary conditions on the case of the adiabatic flow in a constant-area duct with friction, also known as Fanno flow is investigated. The classical Fanno flow case with the no-slip boundary conditions is standard issue in most of the fluid dynamics textbooks (John (1984)) but up to our knowledge it has not been investigated using any of the velocity-slip models so far. The objective of the present work so, is to investigate the effect of both the first order and the second order slip models on the hydrodynamic behavior of compressible flow in

microchannels. This aims to establish criteria that justify the use of the first order slip model instead of the second order slip model.

3.3.1 Governing Equations

In order to derive a relation for a compressible flow in microchannel, the control volume shown in Fig.(3.3) is considered. When the momentum equation is applied to the differential element shown the resulting equation is:

$$-Adp - \tau_f (dx)\frac{4A}{D} = \rho AVdV \tag{3.35}$$

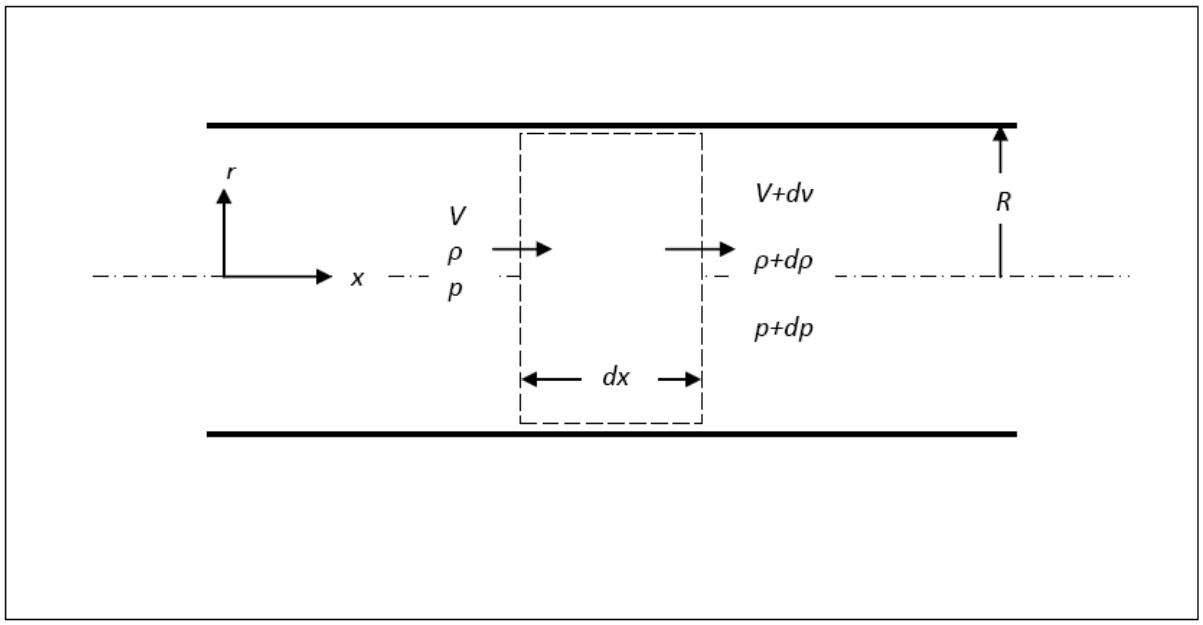

Figure 3.3: Fanno flow problem schematic diagram.

Where τ_f is the shear stress due to the wall friction and D is the pipe diameter. By introducing the friction factor $f = 4\tau_f/(1/2\rho V^2)$ and the Mach number definition ($V = M\sqrt{\gamma \mathcal{R} T}$), the whole equation divided by p, Eq. 3.35 can be rewritten as

$$\frac{dp}{p} + \frac{1}{2}\gamma M^2 f\frac{dx}{D} + \gamma M^2 \frac{dV}{V} = 0 \tag{3.36}$$

Now in order to obtain an expression for the Mach number *M* in terms of distance *x*, the *dp/p* and *dV/V* terms must be replaced. For that, first the ideal-gas equation of state ($\rho=p/RT$) is used, the logarithm is taken and differentiated resulting in the following equation

$$\frac{dp}{p} = \frac{d\rho}{\rho} + \frac{dT}{T} \tag{3.37}$$

In the same manner, using the above mentioned Mach number definition ($V = M\sqrt{\gamma \mathcal{R} T}$), taking the logarithm an then differentiating results

$$\frac{dV}{V} = \frac{dM}{M} + \frac{1}{2}\frac{dT}{T} \tag{3.38}$$

Since the flow considered is adiabatic, the stagnation temperature ($T_0 = T\left(1 + \frac{\gamma-1}{2}M^2\right)$) is constant, so if the definition is used as above it will result:

$$\frac{dT}{T} + \frac{d\left(1+\frac{\gamma-1}{2}M^2\right)}{1+\frac{\gamma-1}{2}M^2} = 0 \tag{3.39}$$

After combining the Eq.(3.36), (3.37), (3.38) and (3.39) and a lengthy procedure of rearrangement and integration [24] the resulting equation can be rewritten in the form

$$\frac{f L_{max}}{D} = \left(\frac{\gamma+1}{2\gamma}\right)\ln\left(\frac{(\gamma+1)M^2}{2\left(1+\frac{\gamma-1}{2}M^2\right)}\right) + \left(\frac{1-M^2}{\gamma M^2}\right) \tag{3.40}$$

where *f* is known as the *Darcy friction factor*. For this equation, the *M* is the inlet Mach number and the outlet Mach number for $L=L_{max}$ is considered to be $M=1$. Since it is expected that for microchannels *f* will differ from the (*64/Re*) value for a pipe obtained using the no-slip model, next *f* should be derived as a function of *Kn* using the first and second order velocity-slip models.

3.3.2 Solution

To obtain the solution for the friction factor f in microchannels the geometry of the problem shown in Fig.(3.3) is considered again. Although the flow at high Mach numbers (supersonic) is turbulent, for the purpose of obtaining the skin friction coefficient it is common practice in the literature to assume that the friction coefficient for turbulent flow is approximately the same as for the laminas flow. This considerably simplifies the mathematical model and is justified by the fact that even for turbulent flows, the area just adjacent to the wall has laminar boundary behavior (laminar sub-layer) and so the velocity gradient at the wall is basically the same and so is the skin friction coefficient. So now, for a constant area circular pipe with a radius R and assuming a fully developed, laminar flow, the momentum equation is reduced to the following:

$$\frac{1}{r}\frac{d}{dr}\left(r\frac{du}{dr}\right)=\frac{1}{\mu}\frac{dp}{dx}=const \tag{3.41}$$

This is solved by integrating twice and applying the appropriate boundary conditions. Even though the velocity at the centerline is not known, from physical considerations it is known that the velocity must be finite at $r=0$, which is our first boundary condition. Now, the second boundary condition, the velocity at the wall must be applied. Here, the slip velocity at the wall will be introduced, once using the first order slip model and once using the second order model. So for the first order slip model the velocity at $r=R$ is:

$$u(R)=-\frac{2-\sigma_v}{\sigma_v}\lambda\left(\frac{\partial u}{\partial r}\right)_R \tag{3.42.a}$$

and for the second order slip model:

$$u(R) = -\frac{2-\sigma_v}{\sigma_v}\left[\lambda\left(\frac{\partial u}{\partial r}\right)_R + \frac{\lambda^2}{2}\left(\frac{\partial^2 u}{\partial r^2}\right)_R\right] \tag{3.42.b}$$

From these two conditions, the constants of integration can be found and the solutions for the velocity profiles for the two velocity-slip models are found. For the first order model the velocity is given by:

$$u(r) = \frac{1}{4\mu}\left(\frac{dp}{dx}\right)\left[r^2 - R^2\left(\frac{2-\sigma_v}{\sigma_v}\cdot 2Kn + 1\right)\right] \tag{3.43.a}$$

and for the second order model the velocity is:

$$u(r) = \frac{1}{4\mu}\left(\frac{dp}{dx}\right)\left[r^2 - R^2\left(\frac{2-\sigma_v}{\sigma_v}\cdot (2Kn + Kn^2) + 1\right)\right] \tag{3.43.b}$$

Once the velocity profiles are found a number of additional features of the flow can be derived from them. Also, the shear stress at the wall $\tau_w = -\mu\left(\frac{du}{dr}\right)_R$ can be derived from the velocity profiles, so when the first order slip and the second order slip models are used the shear stress at the wall is given for the first and second order model respectively by

$$\tau_w = \frac{4\mu\bar{V}}{R\left(\frac{2-\sigma_v}{\sigma_v}\cdot 4Kn+1\right)} \quad \text{and} \quad \tau_w = \frac{4\mu\bar{V}}{R\left(\frac{2-\sigma_v}{\sigma_v}\cdot (4Kn+2Kn^2)+1\right)} \tag{3.44}$$

where $\bar{V}$ is the mean velocity of the flow. Finally, the skin friction coefficient $C_f = \frac{2\tau_w}{\rho\bar{V}^2}$ can be obtained. The skin friction coefficient for the first order and second order slip models are given respectively by:

$$C_f = \frac{16}{Re}\frac{1}{\left(\frac{2-\sigma_v}{\sigma_v}\cdot 4Kn+1\right)} \quad \text{and} \quad C_f = \frac{16}{Re}\frac{1}{\left(\frac{2-\sigma_v}{\sigma_v}\cdot (4Kn+2Kn^2)+1\right)} \tag{3.45}$$

As it can be seen from Eq. (11), for microchannels C_f (and consequently $f=4C_f$) is a function of both *Re* and *Kn* numbers, so next the effect of changing *Kn* number will be investigated for the two slip models and compared to the no-slip model results.

3.4 Solution Methodology

Since the resulting equations are complex and hard to evaluate some type of computer software had to be used in order to obtain the required results. For the purposes of this work, Mathsoft's Mathcad software was used both for its versatility and ease of use.

1. For the first case, the Jeffery-Hamel flow, the resulting system of first order ordinary differential equations. Using Mathcad's built in "odesolve" command which is based on the fourth order Runge-Kutta method and applying it in a solve block, the domain $0 \leq \eta \leq 1$ was divided to 1000 steps and iterations were made until the error in the evaluation of f and f ' dropped below 0.001. The resulting values were used to plot the velocity profiles and to obtain the plots for the differences between the three slip models.
2. For the second sections, the four basic fluctuating gas flows, although the equations 3.30 through 3.34 are obtained analytically, they involve complex numbers and are very hard to evaluate. This is why the software was used here also to evaluate and plot the velocity and temperature profiles at a range of frequency values and to obtain from them the differences and comparison figures.
3. For the third case, the Fanno flow in microchannels, after equations 3.40 and 3.45 were obtained analytically, the software was used to evaluate the Fanno flow lines and the friction coefficient plots for a large range of Mach and Knudsen numbers, and from them to obtain the plots for the differences between the three slip models.

Chapter Four

Results and Discussion

4.1 Jeffery-Hamel Flow in Microchannels

The classical Jeffery-Hamel flow case with no-slip boundary conditions has been studied extensively with the most noticeable contribution made by Rosenhead (1940) who summarized his findings from which the following conclusions have been extracted. For $\pi/2<\alpha<\pi$, a solution with pure outflow is impossible, and pure-inflow solutions are limited in certain respects. Also for $\alpha<\pi/2$, pure inflow is always possible and tends at large Re to have boundary-layer behavior, while pure outflow is limited to certain small Re whose approximate range is $Re<10.31/\alpha$.

Also since the most practical application of this flow is to large Re and small α in the rest of the work, the study will be concentrated on the region $\alpha<\pi/2$ and $Re>>\alpha$. Fig.4.1 represents the classical Jeffery-Hamel flow solution with no-slip boundary conditions which serves as a comparison for the next figure, Fig.4.2, which recreates the same conditions but using the first order slip model at $Kn=0.02$. It can be seen from the two figures that in the no-slip solution, as the name implies the velocity at the wall is always zero, no matter what the $Re\cdot\alpha$ parameter value is, while for the first order slip model, there is a velocity slip which is small for $Re\cdot\alpha>0$ (outflow) and the slip starts to increase as $Re\cdot\alpha$ become smaller and then negative $Re\cdot\alpha<0$ (inflow).

The next five figures, Fig.4.3-4.7 show the velocity profiles resulting from the three models, the no-slip model, the first order and the second order velocity-slip

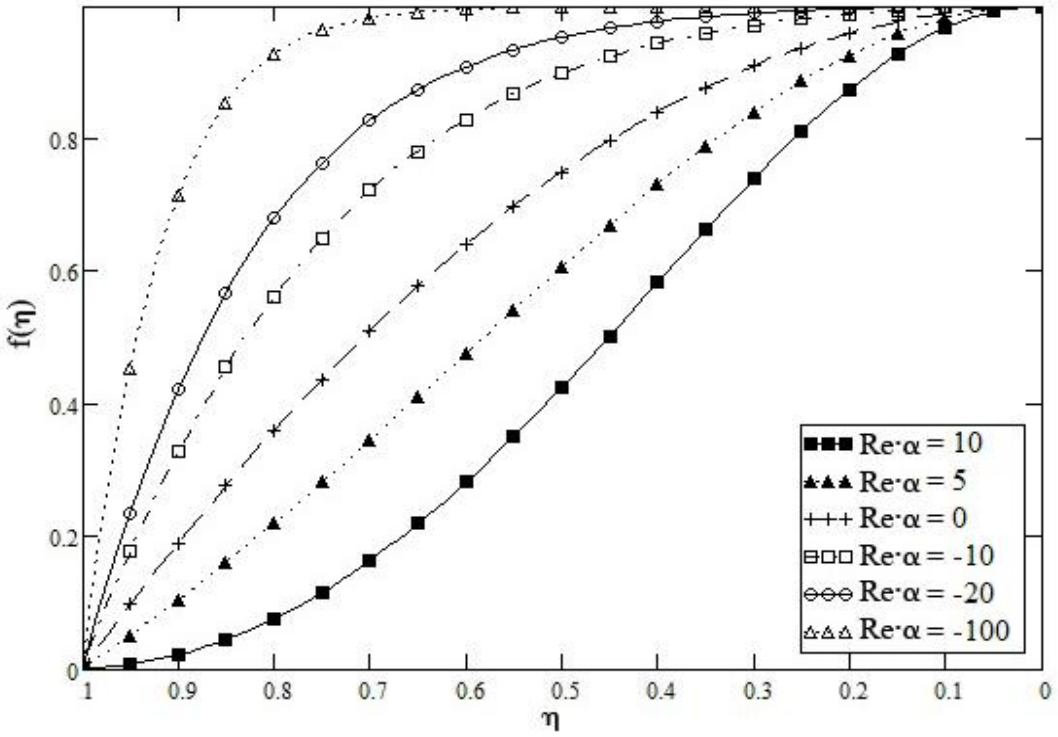

Figure 4.1: Velocity profiles for Jeffery-Hamel flow at $Re>>\alpha$ with no slip boundary conditions. [34]

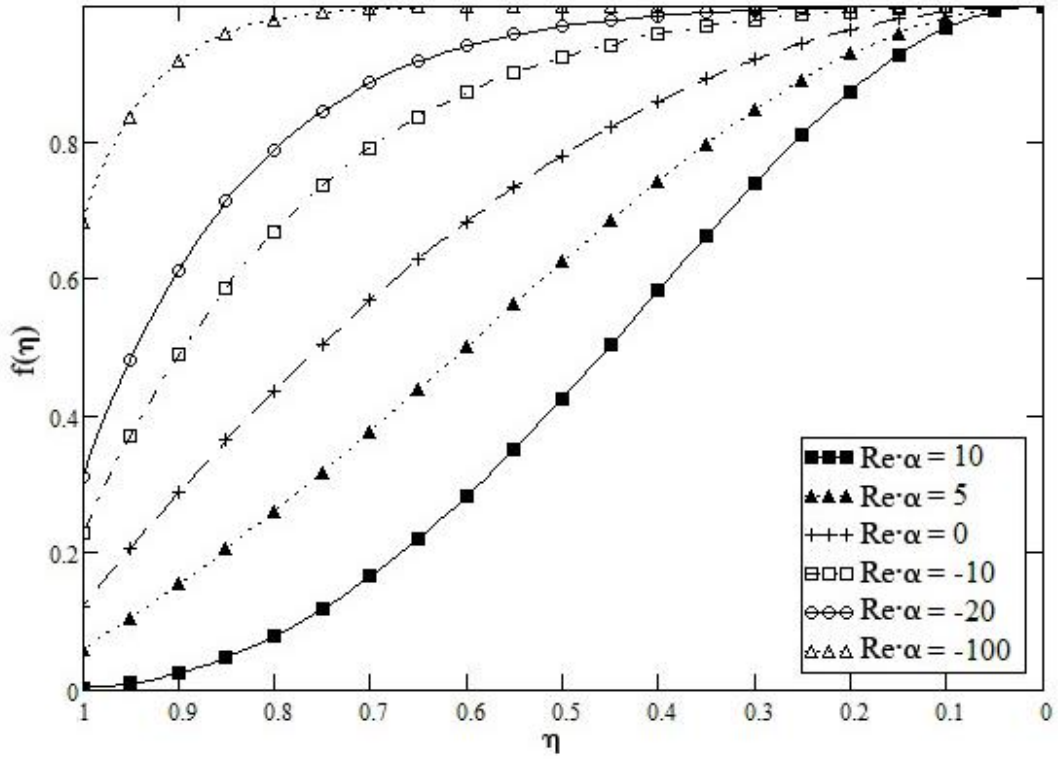

Figure 4.2: Velocity profiles for Jeffery-Hamel flow at $Re>>\alpha$ with first order velocity-slip boundary condition at $Kn=0.02$

models at different $Re \cdot \alpha$ and for different Kn numbers. Fig.4.3 and Fig.4.4 show the velocity profiles for $Re \cdot \alpha = -10$ *and* $Re \cdot \alpha = -5$ respectively which is an inflow. What can be seen from those two figures is that increasing the Kn number will increase the velocity slip at the wall. The difference between the no-slip model and the two slip models is small up to a $Kn = 0.01$ after which it becomes significant. Also the difference between the first order slip and the second order slip models is relatively small up to about $Kn = 0.05$ after which it becomes noticeable.

The next figure (Fig.4.5) shows the velocity profiles at $Re \cdot \alpha = 0$, and from it can be seen here that the difference between the no-slip model and the two slip models is negligible all the way up to $Kn = 0.01$ and becomes important only at larger values of Kn. What differentiates this figure from the two above is first, that the slip at the wall is smaller in magnitude than in the previous two figures and second, that the difference between the first order slip and the second order slip models is negligible across the entire Kn number range explored.

Figures 4.6 and 4.7 compare the velocity profiles for the three models for $Re \cdot \alpha = +5$ and $Re \cdot \alpha = +10$ respectively which represents outflow. Fig.4.6 shows that the difference between the no-slip model and the two slip models is very small for $Kn < 0.05$ and also that the difference between the first order slip and the second order slip models is negligible across the entire Kn number range explored. On the other hand Fig.4.7 shows a slightly different behavior. As it can be seen, the velocity profiles for the three models are so close that they cannot be differentiated from one another, but the interesting thing here is that the second order model predicts a negative slip velocity at the wall as Kn increases which indicates separation of the flow at that point.

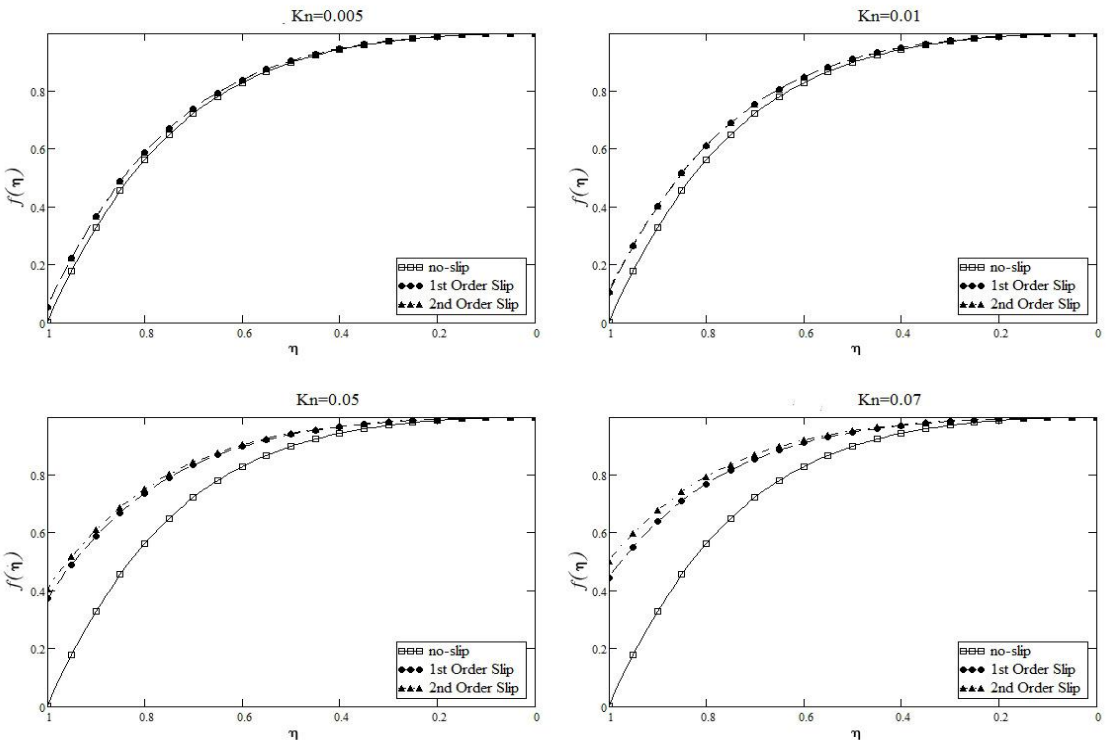

Figure 4.3: Comparison of the velocity profiles for Jeffery-Hamel flow at $Re \cdot \alpha = -10$ using the three models, no-slip, first order and second order velocity-slip boundary conditions.

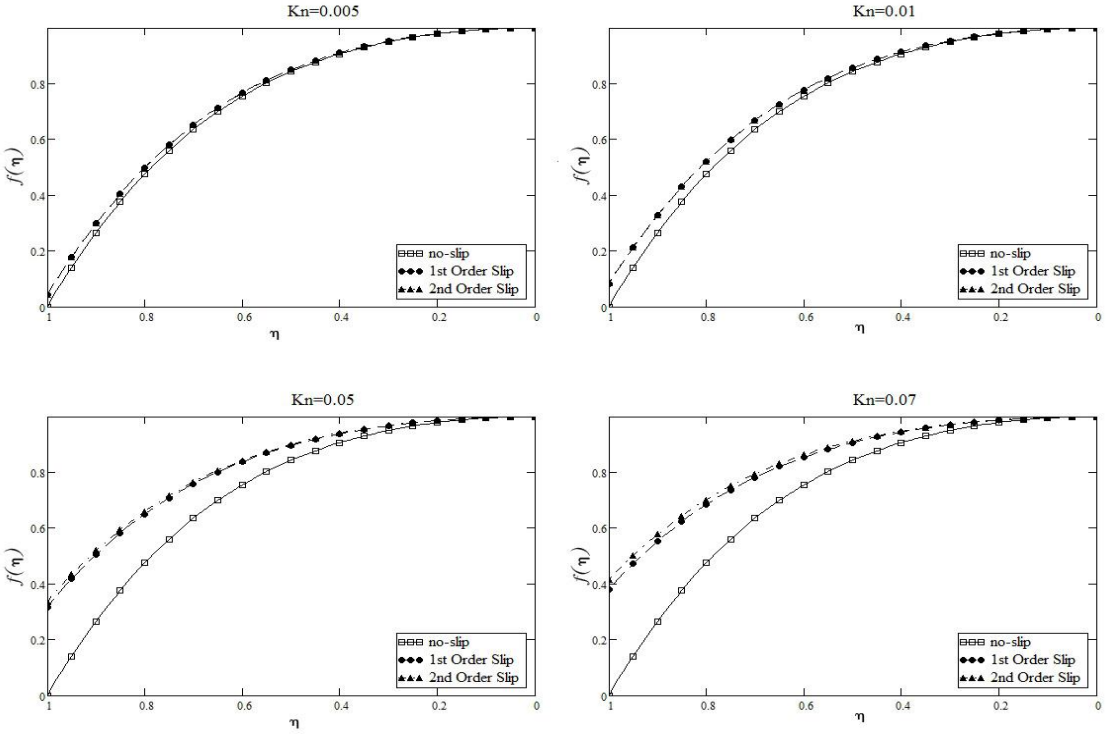

Figure 4.4: Comparison of the velocity profiles for Jeffery-Hamel flow at $Re \cdot \alpha = -5$ using the three models, no-slip, first order and second order velocity-slip boundary conditions.

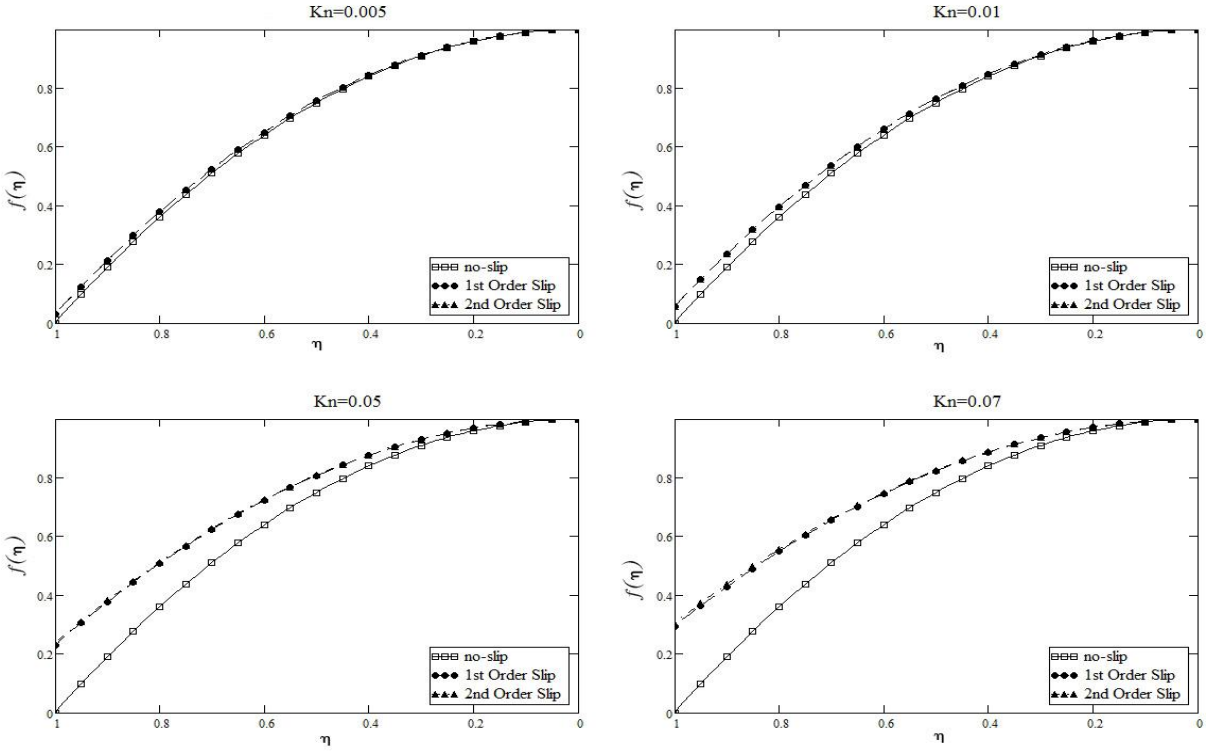

Figure 4.5: Comparison the velocity profiles for Jeffery-Hamel flow at *Re·α=0* using the three models, no-slip, first order and second order velocity-slip boundary conditions.

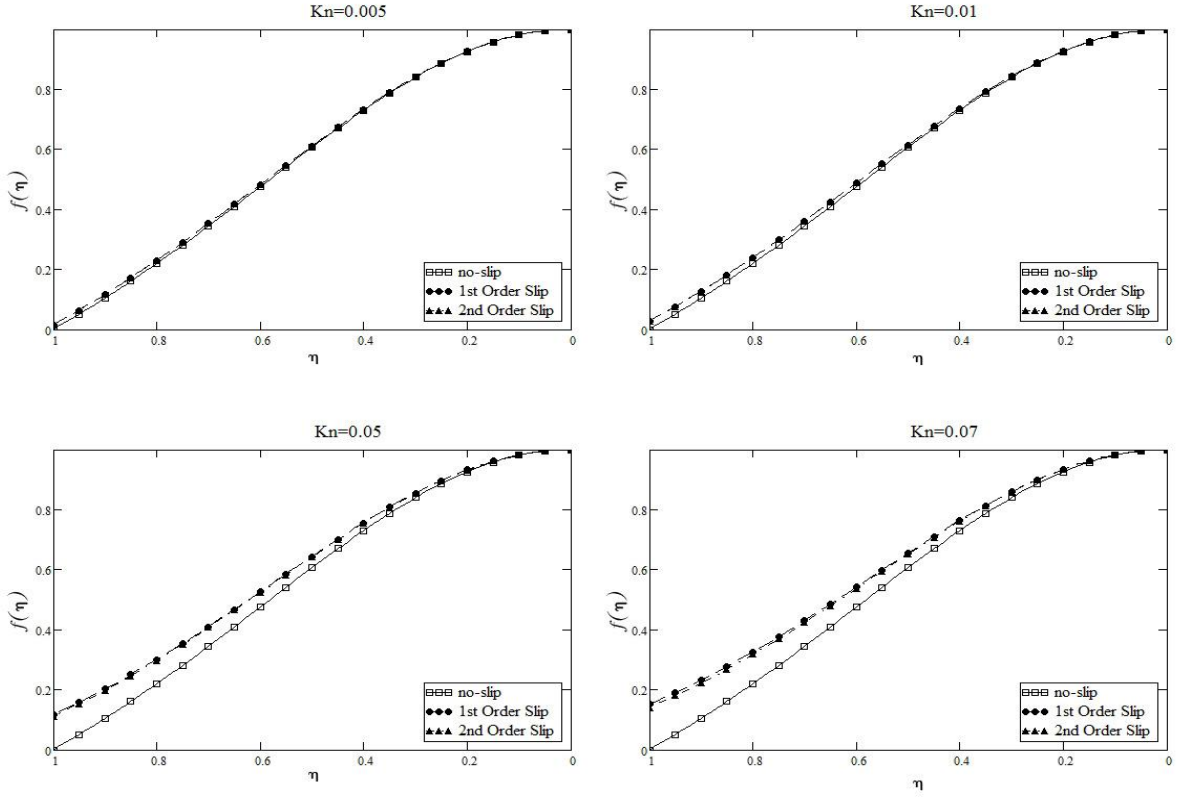

Figure 4.6: Comparison of the velocity profiles for Jeffery-Hamel flow at *Re·α=+5* using the three models, no-slip, first order and second order velocity-slip boundary conditions.

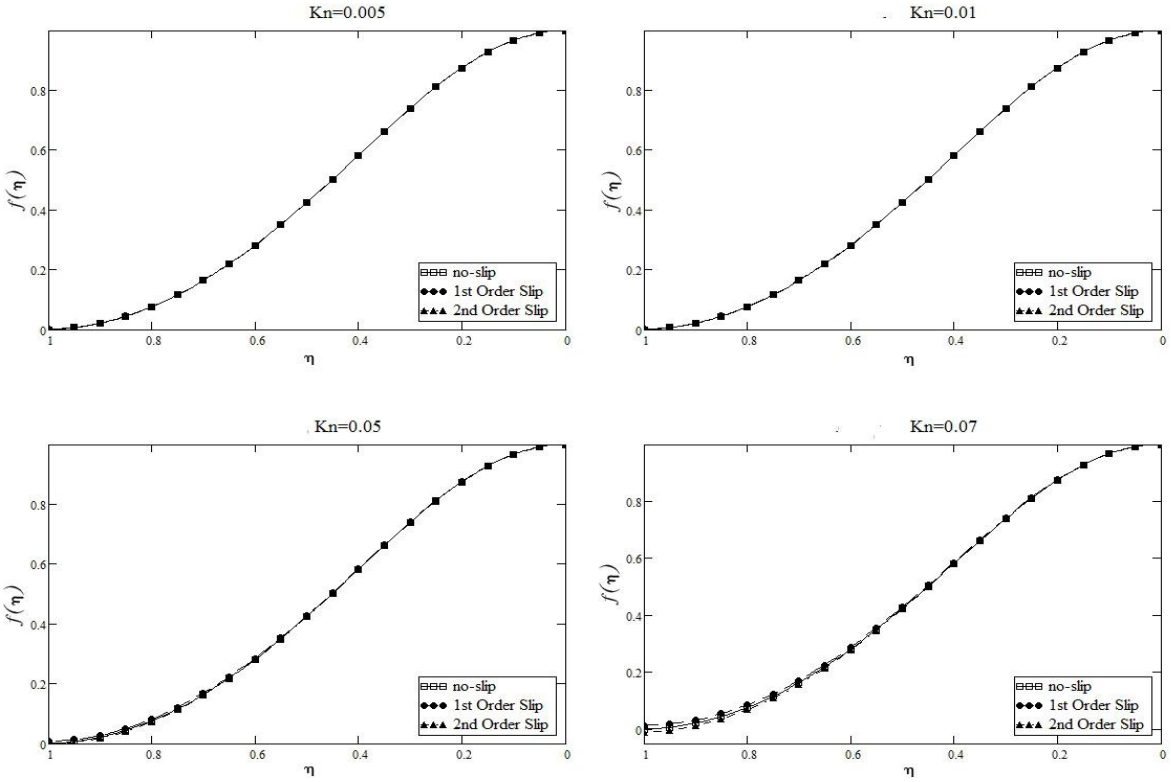

Figure 4.7.a: Comparison of the velocity profiles for Jeffery-Hamel flow at *Re·α=+10* using the three models, no-slip, first order and second order velocity-slip boundary conditions.

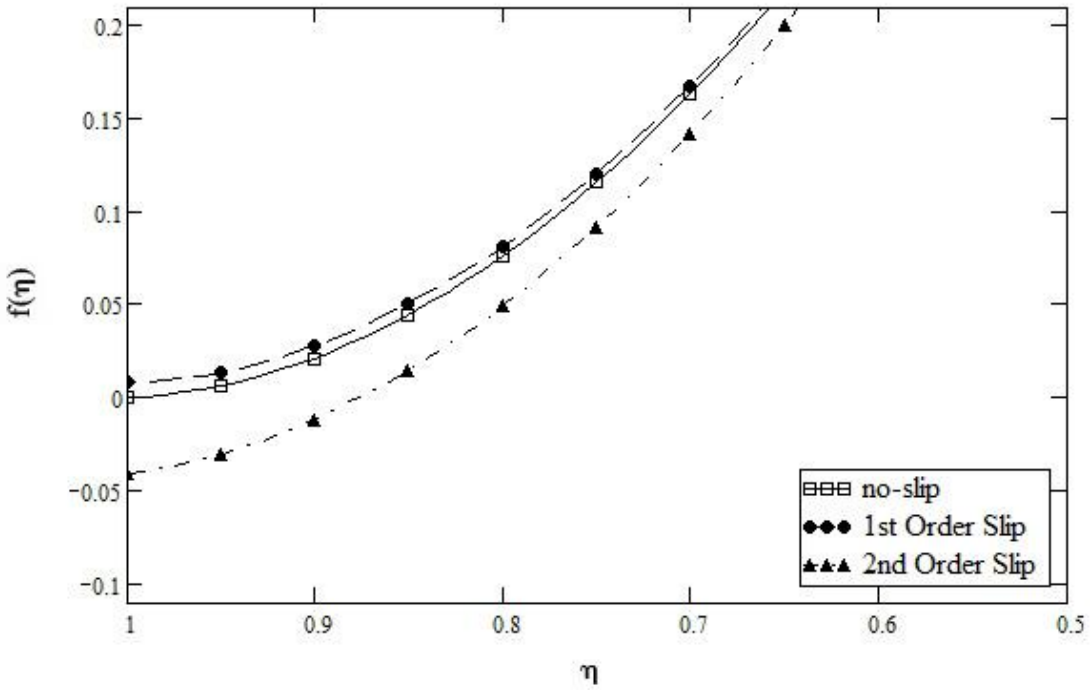

Figure 4.7.b: Comparison of the velocity profiles for Jeffery-Hamel flow at *Re·α=+10* and *Kn = 0.1* near the wall for the purpose of clarification of the backflow occurrence using the three models, no-slip, first order and second order velocity-slip boundary conditions.

The flow separation is well documented case in the Jeffery-Hamel flow with no slip boundary conditions. As it was seen in figures 4.1, 4.6 and 4.7, for the outflow the velocity profiles become S-shaped as a result of the change in sign of the streamwise pressure gradient. For inflow, the pressure p decreases in the direction of the flow (favorable pressure gradient) and there is no separation, while for the outflow, the pressure increases downstream (adverse pressure gradient) and causes inflection in the velocity profile until at some point a separation occurs. For the no-slip boundary conditions this separation point is function of $Re\cdot\alpha$ and has been found by Millsaps and Pohlhausen (1953) to occur at $Re\cdot\alpha=10.31$, but as it can be seen from Fig.4.7, the second order slip model predicts that separation can occur at smaller $Re\cdot\alpha$ if the Kn number is sufficiently large.

Assuming that a difference between the no-slip model and the first order velocity-slip of *10%* or more is significant enough to justify the use of the velocity-slip model, criteria for the use of the first order slip model can be set. By examining Fig.4.8, it can be seen that for $Re\cdot\alpha=-10$ the difference reaches *10%* at $Kn=0.01$, for $Re\cdot\alpha=-5$ at $Kn=0.012$, for $Re\cdot\alpha=0$ at $Kn=0.02$ and for $Re\cdot\alpha=+5$ the difference reaches *10%* at $Kn=0.04$. As for the $Re\cdot\alpha=+10$ the difference between the three models is negligible but since the second order slip model predicts separation it will be studied more extensively later.

Also of interest is the difference between the first order slip and the second order slip models. This is why the normalized difference ($\Delta= \left|\frac{u_1(1)-u_2(1)}{u_1(1)}\right|$, where the 1 and 2 subscripts stand for first and second order slip model respectively) between the two models is shown in Fig.4.9.

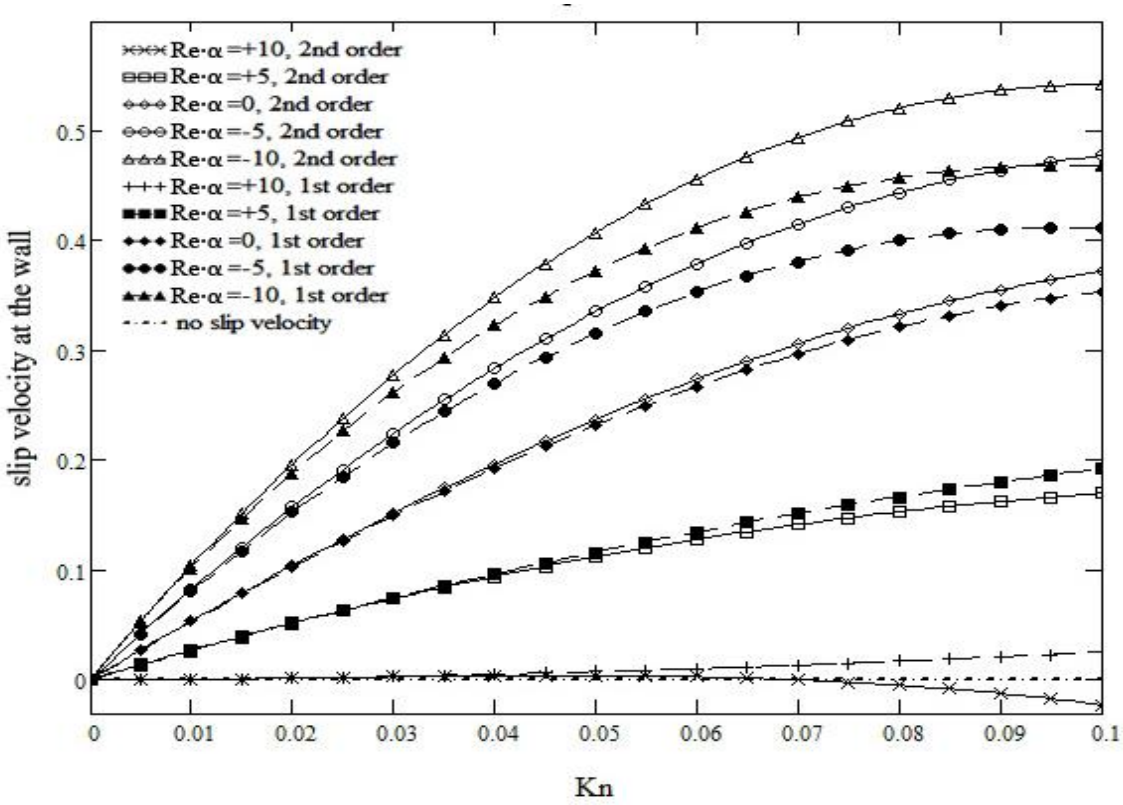

Figure 4.8: Comparison between the first and the second order models predicted slip velocity at the wall.

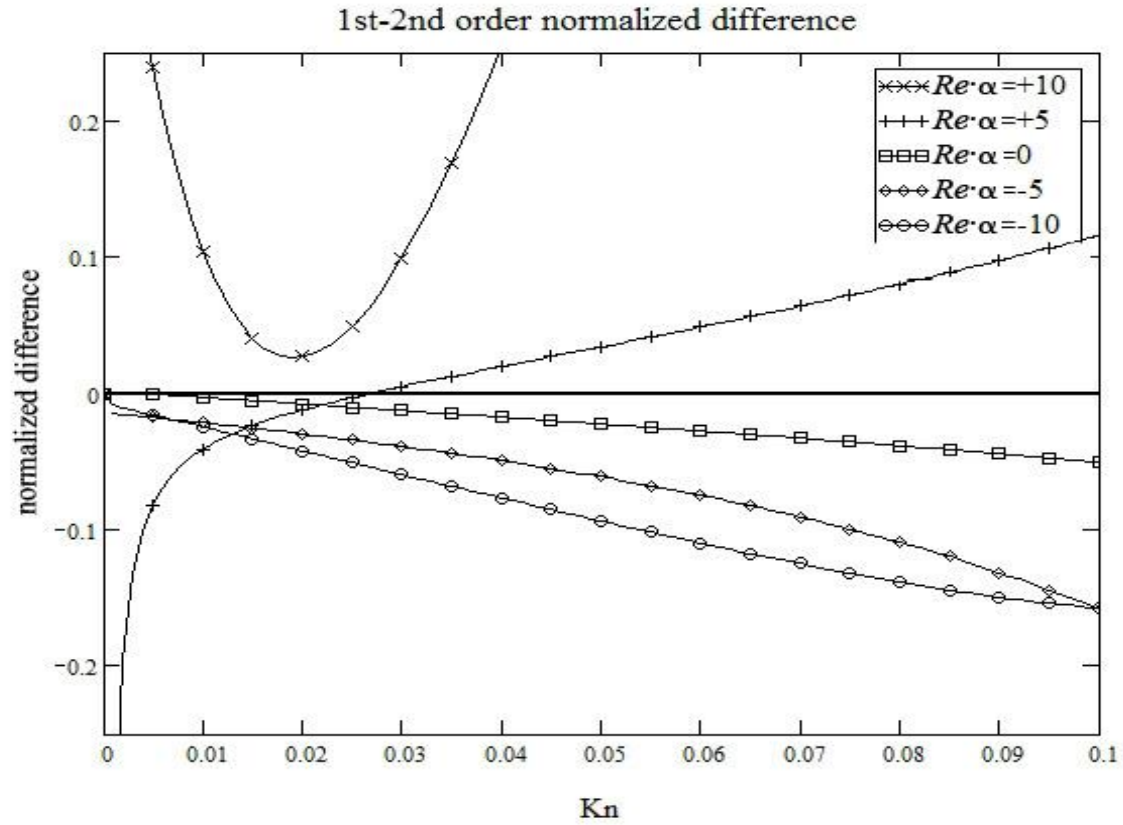

Figure 4.9: Normalized difference between the first and the second order models predicted velocity-slip at the wall.

Ignoring the line which shows the difference at $Re{\cdot}\alpha=+10$ as it represents the case where separation occurs, the line representing the difference for outflow at $Re{\cdot}\alpha=+5$ is examined. Using the same *10%* difference criteria, it can be seen that the second order model becomes necessary only for $Kn>0.09$ which is very close to the upper limit of the range in which the Navier-Stokes equation with slip boundary conditions is applicable. For $Re{\cdot}\alpha=0$ the difference between the two models never reaches *10%* so, for this case the first order slip model will be sufficient. As for the inflow cases at $Re{\cdot}\alpha=-5$ and $Re{\cdot}\alpha=-10$, the difference becomes significant at $Kn=0.075$ and $Kn=0.052$ respectively.

Next the effect of the *Kn* number on the skin friction coefficient C_f is examined. Fig.4.10 shows the skin friction coefficient C_f for an inflow with different values of *Re* number while Fig.4.11 represents C_f for an outflow. As it can be seen for inflow, the two velocity-slip models result in reduced friction at the wall with the second order slip model always results in lower friction coefficient values. On the other hand for the outflow cases, it is seen that at small *Re* both models show lower friction coefficient than the no-slip model and the second order slip model predicts lower values than the first order model. As the *Re* increases to $Re=50$, the second order model results in values larger than the first order model but still lower than the no-slip model. And last as the *Re* number increases to $Re=100$, the values of C_f predicted by the second order slip model drastically increases and become even larger than the values for the no-slip model. This strange behavior can be attributed to the reversal of the flow at the wall (separation) which only the second order slip model predicts.

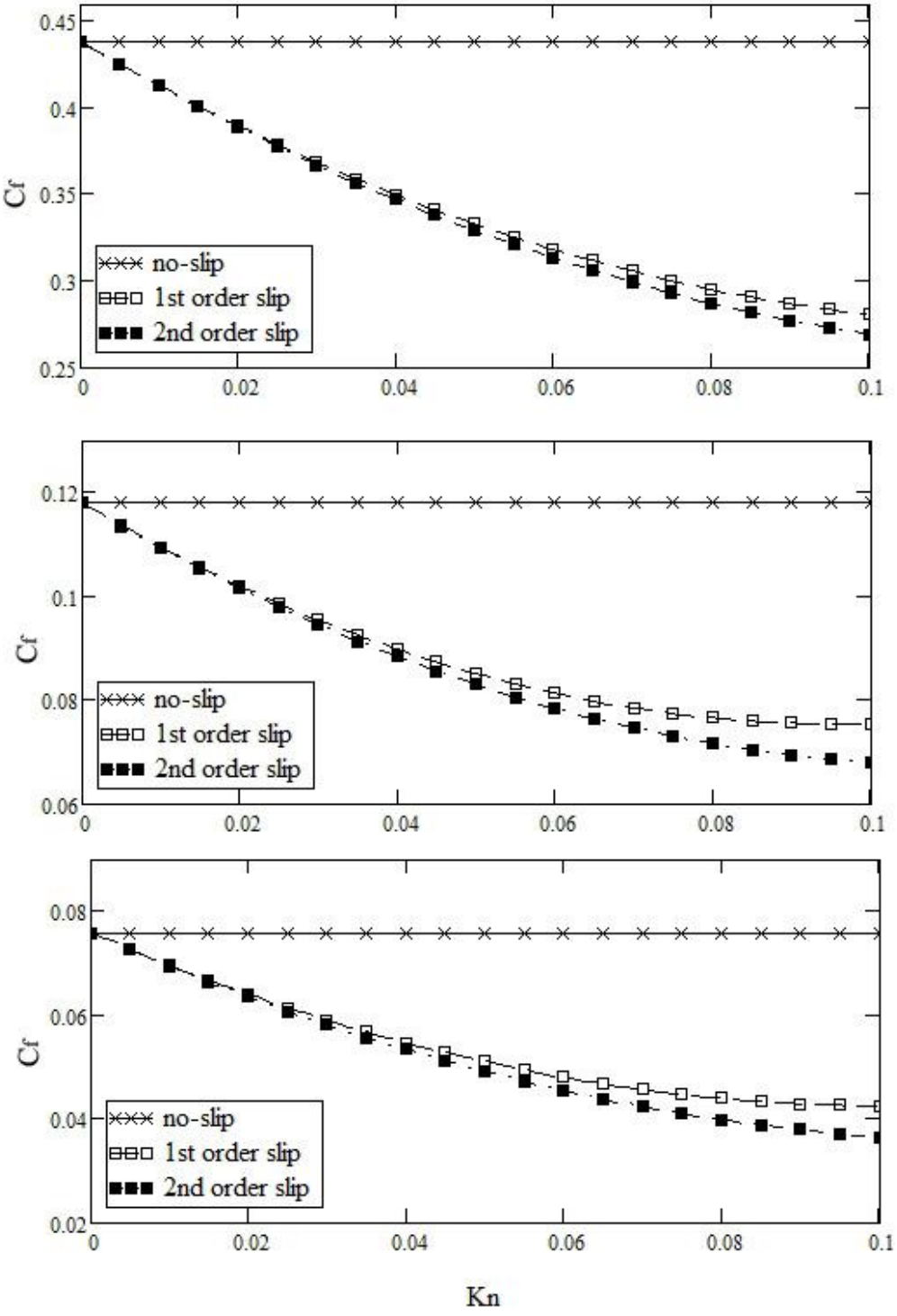

Figure 4.10: Friction coefficient C_f comparison for inflow at α=*-0.1* and different *Re*: (a) for *Re=10*, (b) for *Re=50* and (c) for *Re=100*.

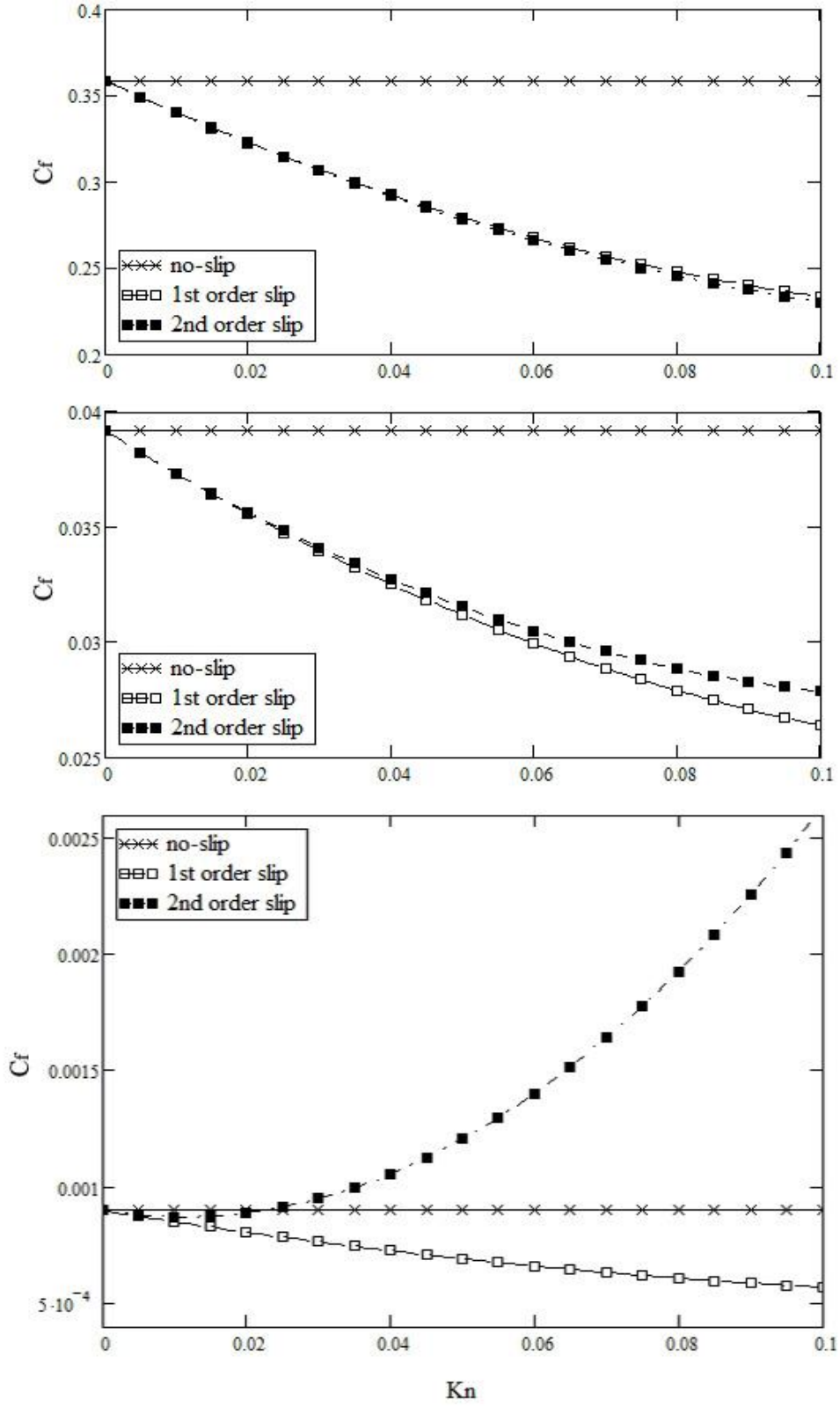

Figure 4.11: Friction coefficient C_f comparison at $\alpha=+0.1$ and different *Re*: (a) for *Re=10*, (b) for *Re=50* and (c) for *Re=100*.

Due to the importance of the separation concept on the analysis so far it was further investigated and summarized in figures 4.12 and 4.13. The first one (4.12) shows the velocity slip at the wall as predicted by the second order velocity-slip model, for different values of *Kn* as a function of *Re·α*. It shows that as the *Kn* number increases the *Re·α* value for which the separation occurs decreases. For *Kn=0.01* the separation occurs at about *Re·α=10.2* which is very close to the results for the no slip solution, while for *Kn=0.1* the separations occurs at *Re·α=8.8*. The second figure (4.13) represents, the slip velocity at the wall for different *Re·α* as a function of *Kn* number. It shows that the larger the *Re·α* value is, the smaller the *Kn* number needed for separation to occur is.

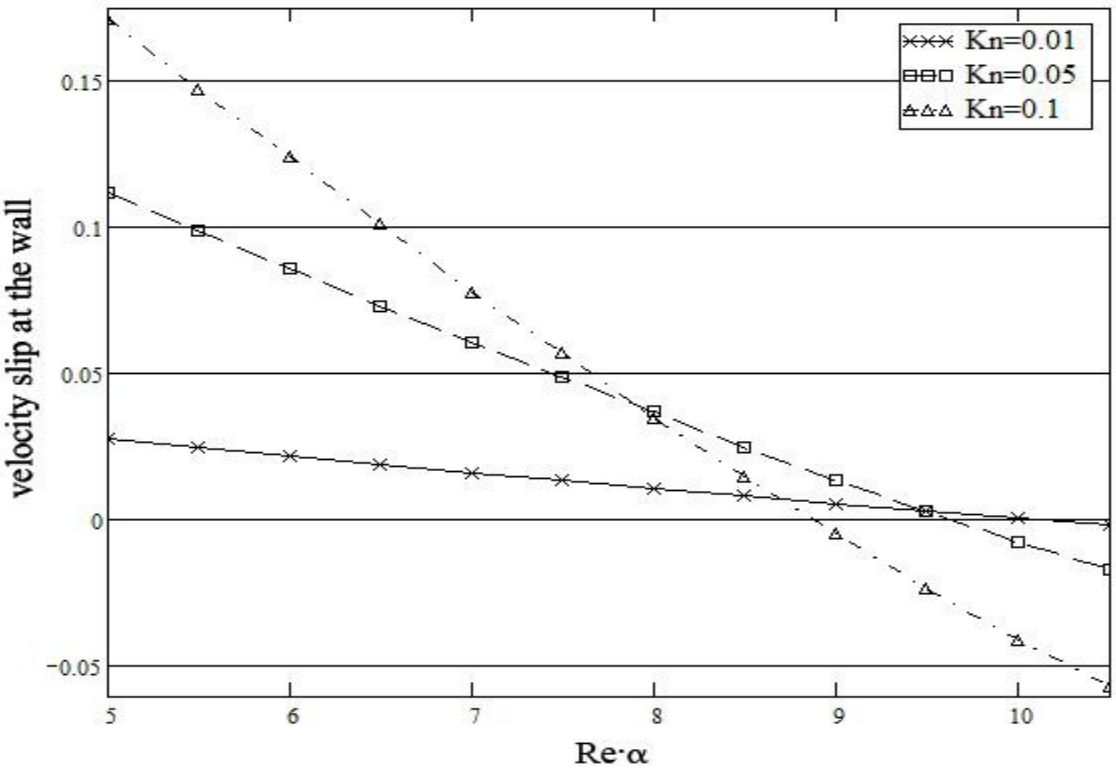

Figure 4.12: Second order model predicted velocity slip at the wall for different *Kn* numbers as a function of *Re·α*

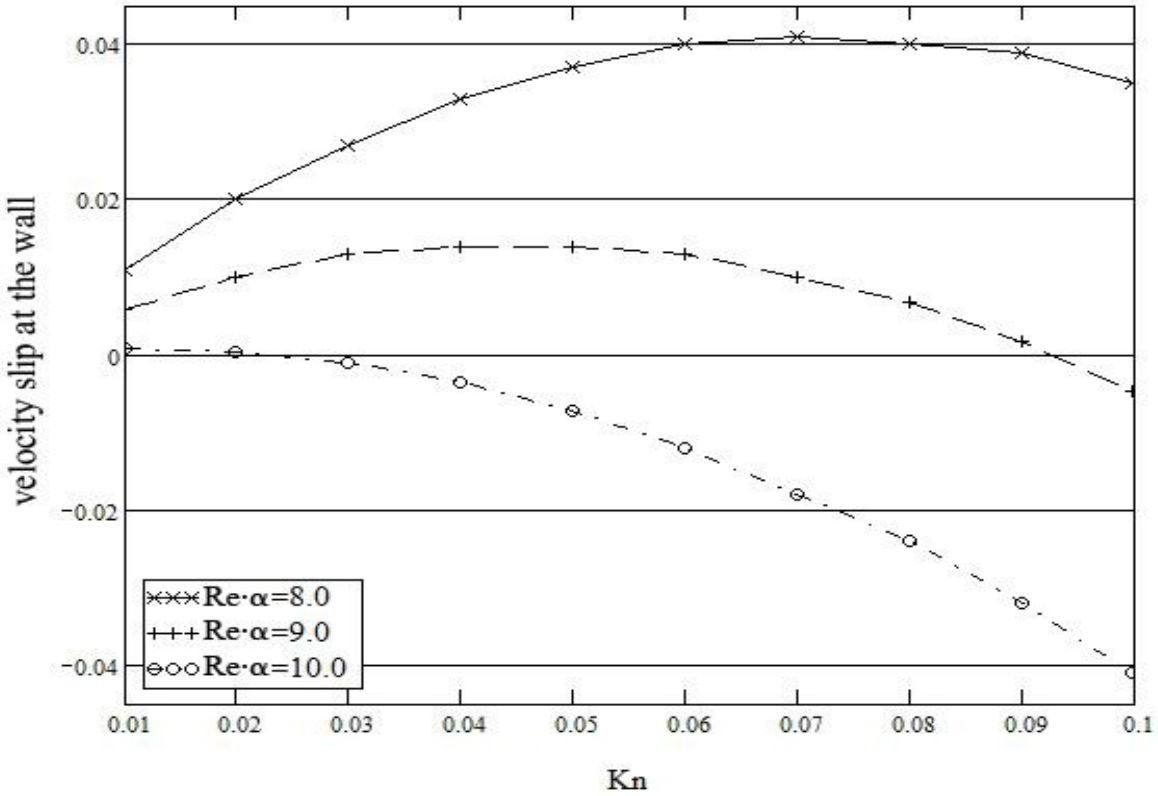

Figure 4.13: Second order model predicted velocity slip at the wall for different $Re{\cdot}\alpha$ as a function of *Kn* number.

4.2 Basic Gaseous Fluctuating Micro-Flows

After the solutions for the four cases were obtained, they were plotted in the figures 4.14 to 4.28. All the graphs were for *Kn=0.1* as it is considered the end of the region in which the Navier-Stokes equations with velocity-slip and temperature-jump are applicable. The velocity and temperature accommodation coefficients σ_v and σ_t both are in the range of ($0.2 \leq \sigma \leq 0.8$) so an intermediate value of $\sigma = 0.5$ is used for all plots. The instantaneous velocity and temperature profiles for all four cases are plotted in figures 4.14, 17, 20, 23 and 24 for both the first order slip and the second order velocity-slip and temperature-jump models.

What can be observed by looking at these velocity profiles plots and at Fig. 4.18, 25 and 26, is that as the driving force frequency increases the amplitude of the velocity or temperature at the wall decreases. This is due to the fact that the total amount of momentum transferred to the fluid by the wall in the Couette flow and Stoke's second problem case, the pressure energy from the pump in the Poiseuille flow case and the thermal energy transferred from the wall in the natural convection case all decrease as the frequency increases. That is because the total energy transferred to the fluid is proportional to ($cos(\omega t)/\omega$), so as the frequency increases the total energy decreases.

From these same velocity and temperature profiles figures it can be also seen that at lower frequencies the two models behave almost the same and so the first order velocity-slip/temperature-jump model being simpler is easier and more economical to use. But as the frequency increases they start to deviate from each other and when the difference between the two becomes significant enough the more complex, the implementation of the second order velocity-slip/temperature-jump model becomes a must for an improved accuracy.

The limiting frequency for this depends besides on the *Knudsen* number also on the geometry and flow driving force. The flow in both cases 1 and 3 is caused by the fluctuating walls and as such they follow a very similar pattern for the differences between the different models as can be seen in Fig. 4.15 and 21. From figures 4.16 and 4.22 the effect the *Knudsen* number on the normalized difference ($\Delta = \left|\frac{u_1(Y,\omega,\tau)-u_2(Y,\omega,\tau)}{u_1(Y,\omega,\tau)}\right|$, where the 1 and 2 subscripts stand for first and second order slip model respectively) between the two models can be seen. Basically, the smaller the *Kn* number is the smaller the normalized difference between the two models is. So, for the purpose of this work the comparison between the two model has been made at *Kn=0.1* as it is considered the upper limit of the region in which the Navies-Stokes equations with velocity-slip/temperature-jump boundary conditions are applicable and so the difference between the two models is more pronounced there.

If a 5% difference is considered to be significant enough to justify the use of the more complex model then from the detailed difference plot between the two models in Fig.4.16 and 22 it can be seen that at a $Kn = 0.1$ this happens for a dimensionless frequency of about $\omega = 8$. This means that for a fluctuating wall frequency higher than $\varpi = 8\nu/L^2$ for case 1 and $\varpi = 8u_0^2/\nu$ for case 3 the second order model should be used as it is significantly more accurate. In comparison, for case 2 where the flow is driven by a pump with a fluctuating pressure gradient, the behavior of the difference between the two models is completely different as can be seen in figures 4.18 and 19. For this case, and at large *Kn* number the slip at the wall is even more sensitive to the frequency, as can be seen in Fig. 4.19, the slip at the wall is close to 5% even below $\omega = 1.0$. So basically, at relatively large *Kn* numbers and for fluctuating pressure gradient driven flow the second order model should be used for any $\varpi \geq \nu/L^2$. In the fourth case the flow is driven by a temperature difference caused by fluctuating heating source. This is

why for it the resulting temperature profiles were studied using both the first and second order temperature-jump models in addition to the velocity profiles like in the previous three cases. As it can be seen from Fig. 4.23 and 24 the two models behave similarly at relatively low frequencies but start to deviate significantly as the frequency increases. Using the same analysis criteria as for the previous three cases and by looking at Fig.4.27 it can be found that the difference between the two temperature-jump models becomes significant for $\omega_t \geq 7$ or $\varpi_t = 7\nu/L^2$. As for the velocity-slip models, the difference between the two, is even more pronounced, as can be seen in Fig.4.28, and the frequency for which the difference of slip at the wall becomes significant is $\omega_v \geq 1.35$ which is equal to $\varpi_v = 1.35\nu/L^2$.

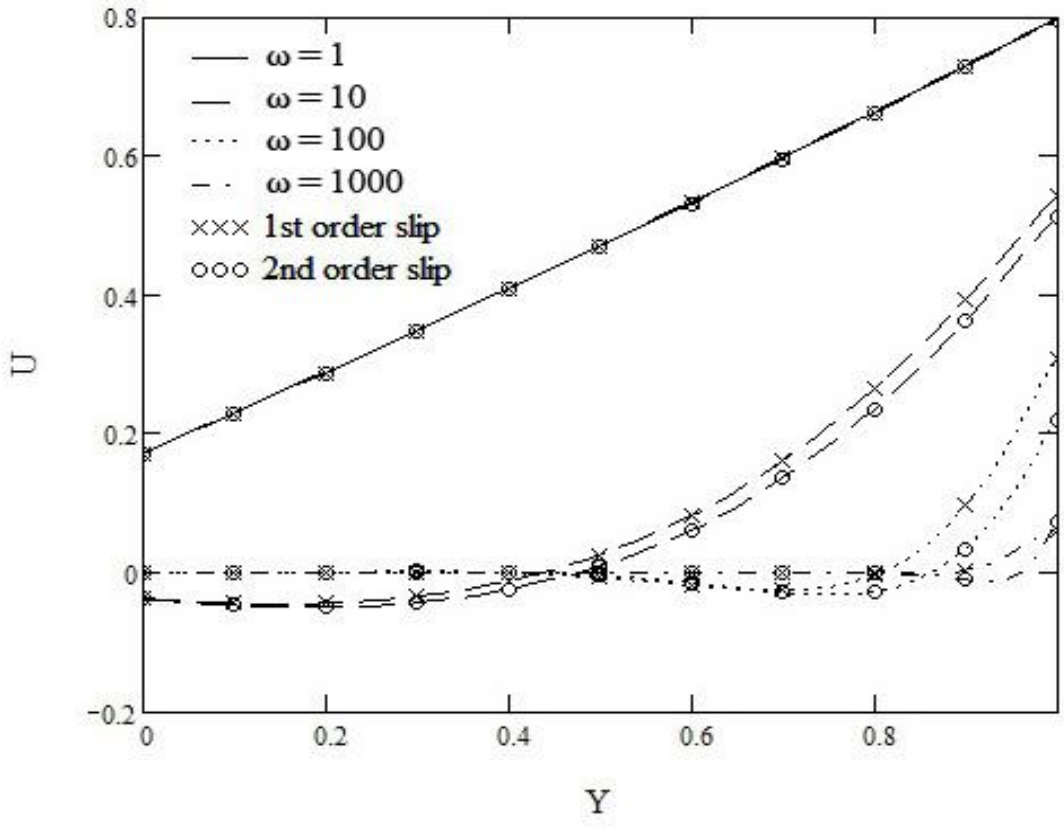

Figure 4.14: Case 1 – Velocity profiles for first and second order slip at $\tau = TP/4$ and $Kn=0.1$.

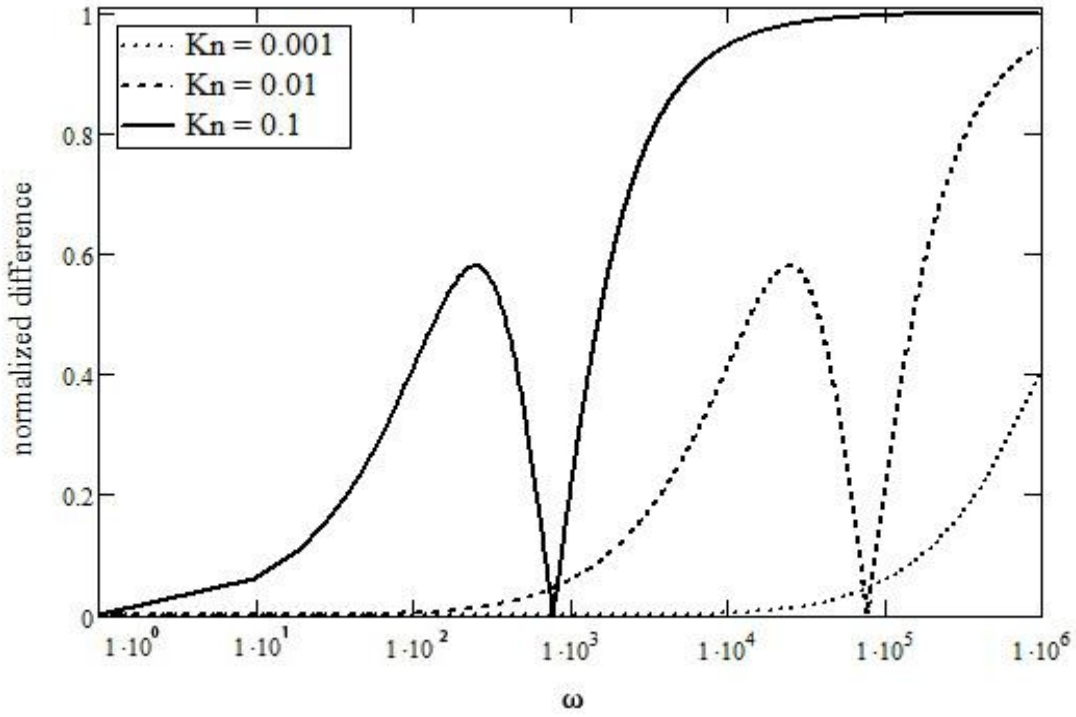

Figure 4.15: Case 1 – Normalized velocity slip difference between first and second order slip as a function of frequency for different *Kn* numbers.

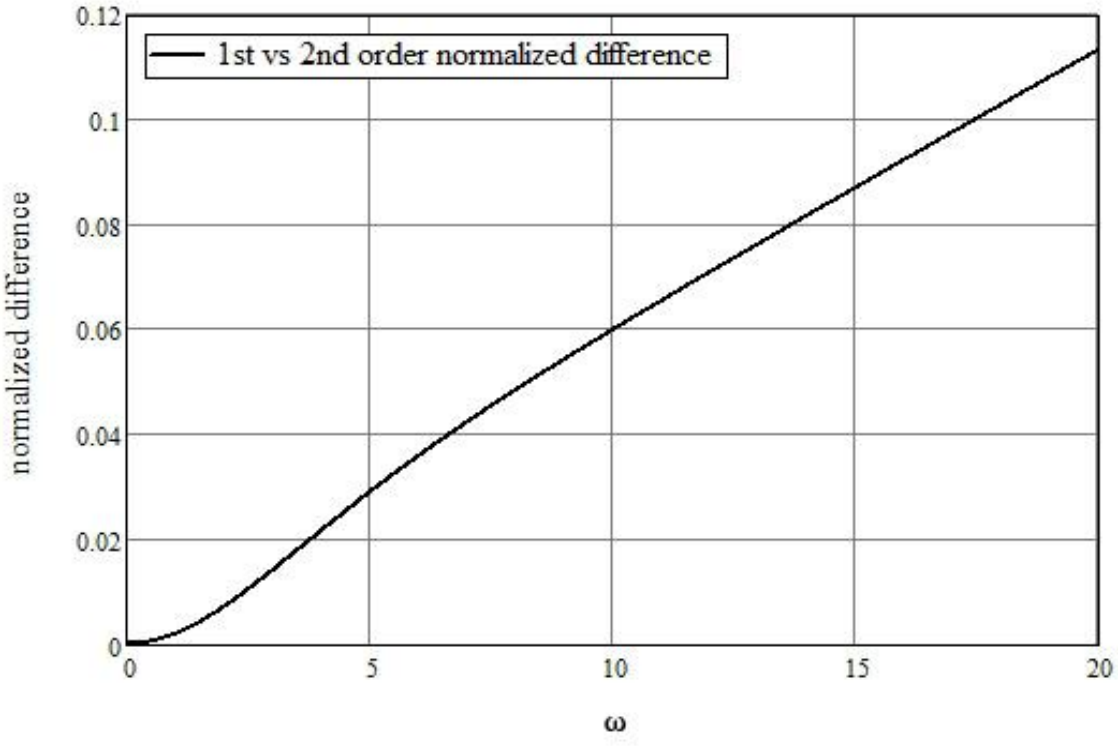

Figure 4.16: Case 1 – Normalized velocity slip difference between first and second order slip as a function of frequency for $\tau = TP/4$ and $Kn = 0.1$.

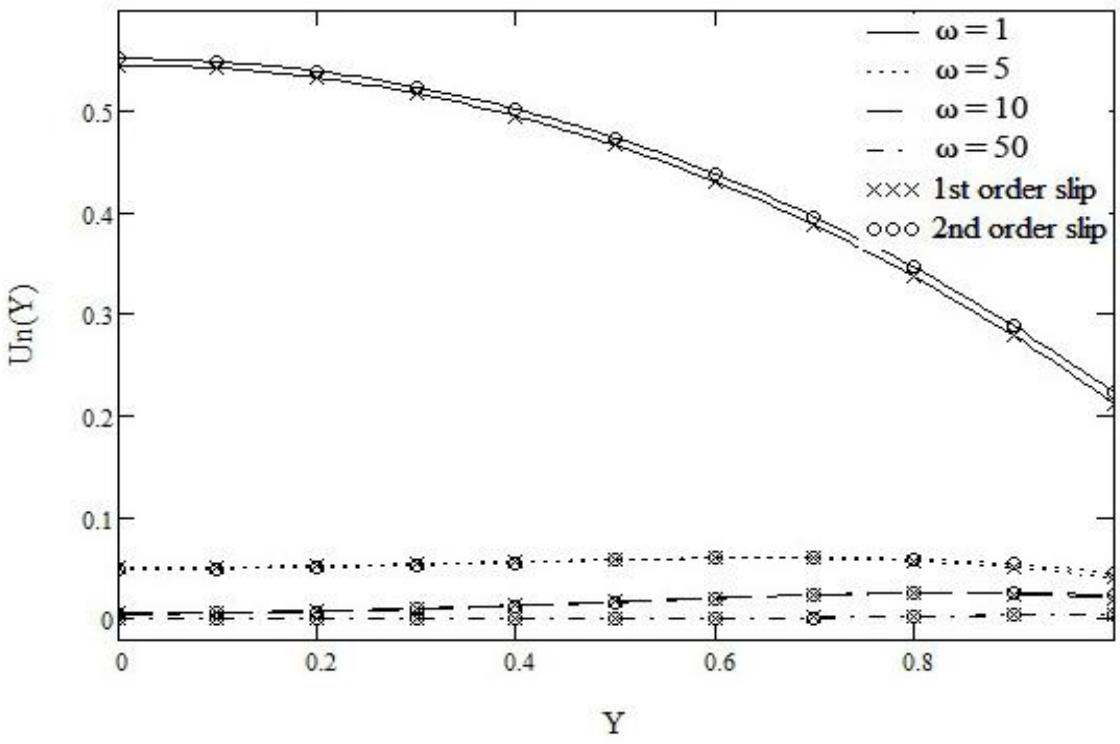

Figure 4.17: Case 2 – Velocity profiles for first and second order slip at $\tau = TP/4$ and $Kn = 0.1$.

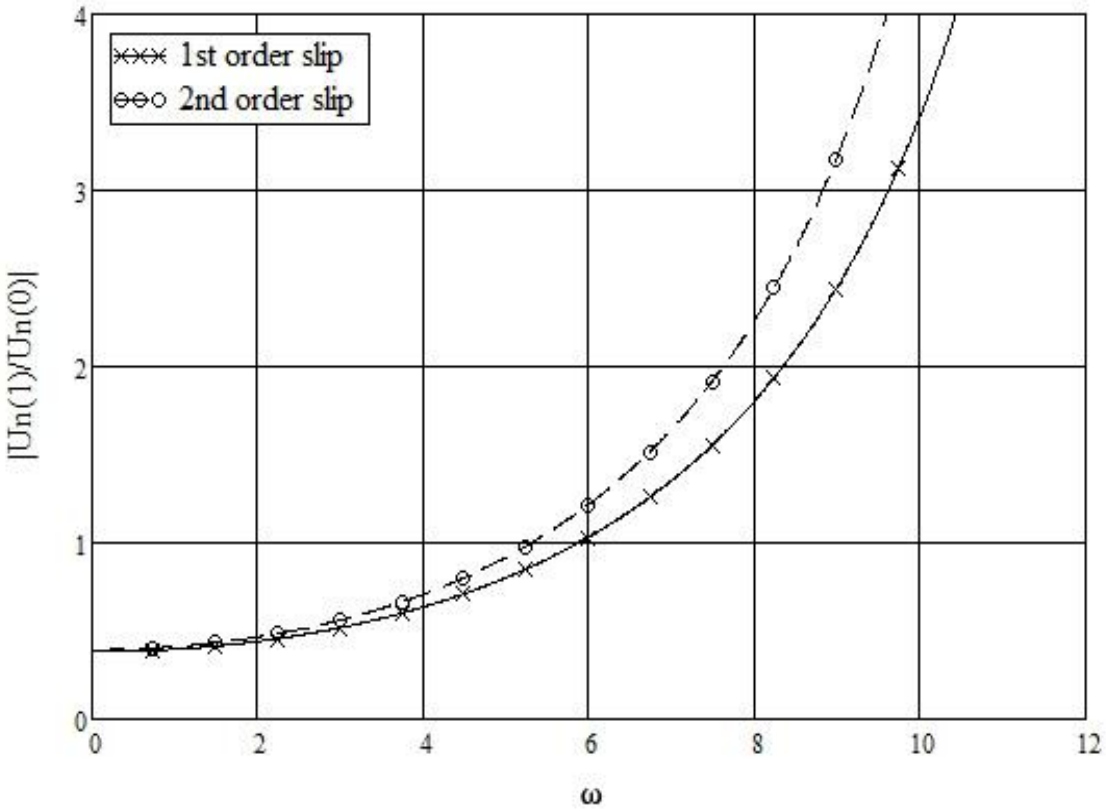

Figure 4.18: Case 2 - Normalized velocity slip for the first and second order slip as a function of frequency for $\tau = TP/4$ and $Kn = 0.1$.

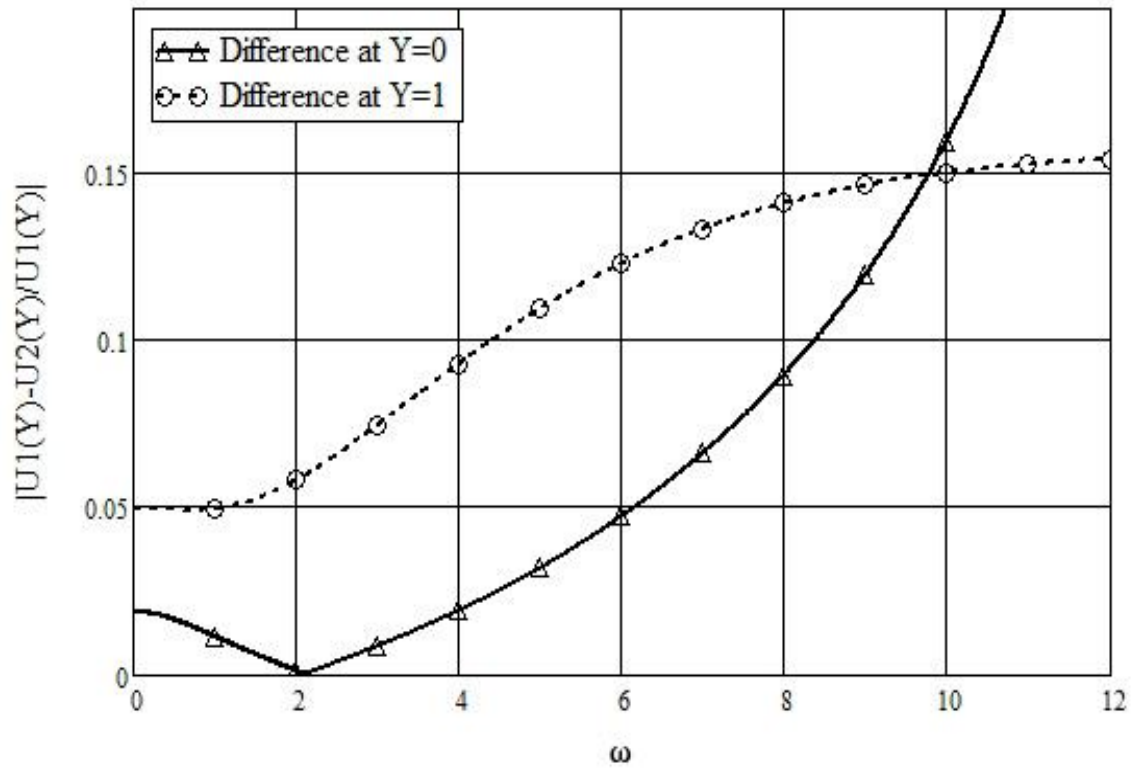

Figure 4.19: Case 2 - Normalized velocity slip differences between first and second order slip as a function of frequency for $\tau = TP/4$ and $Kn = 0.1$.

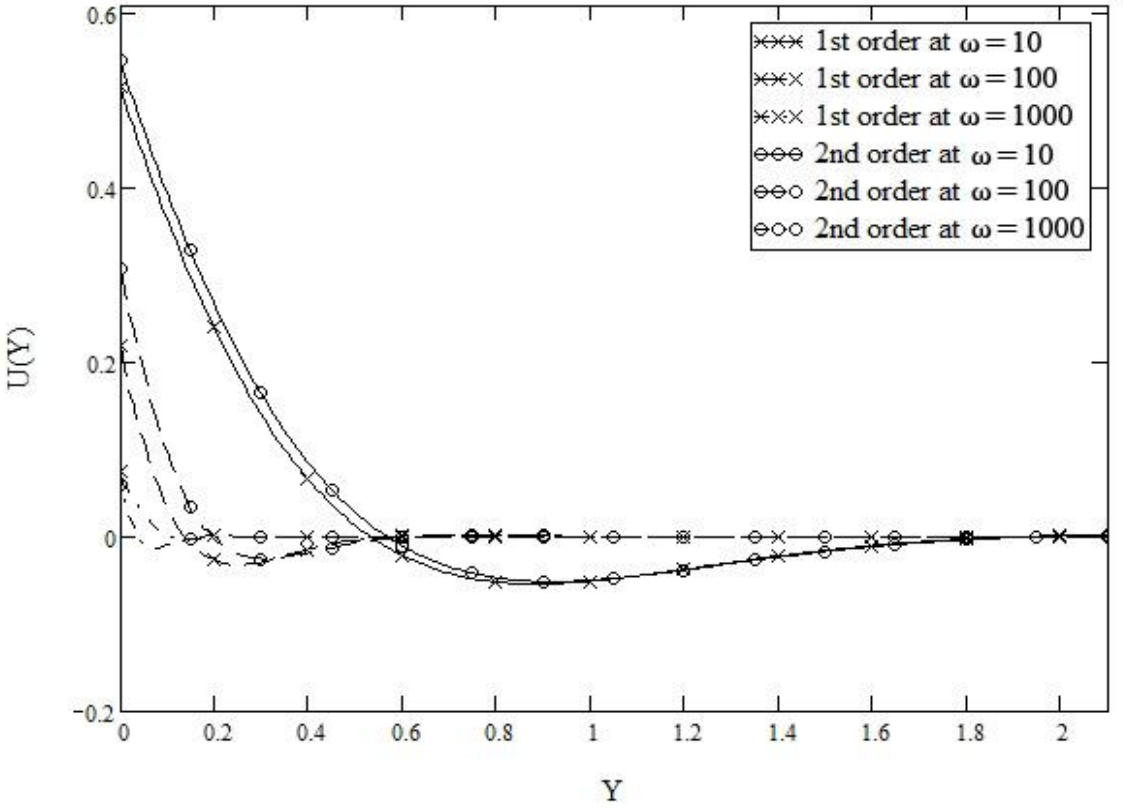

Figure 4.20: Case 3 - Velocity profiles for first and second order slip at $\tau = TP/4$ and $Kn = 0.1$.

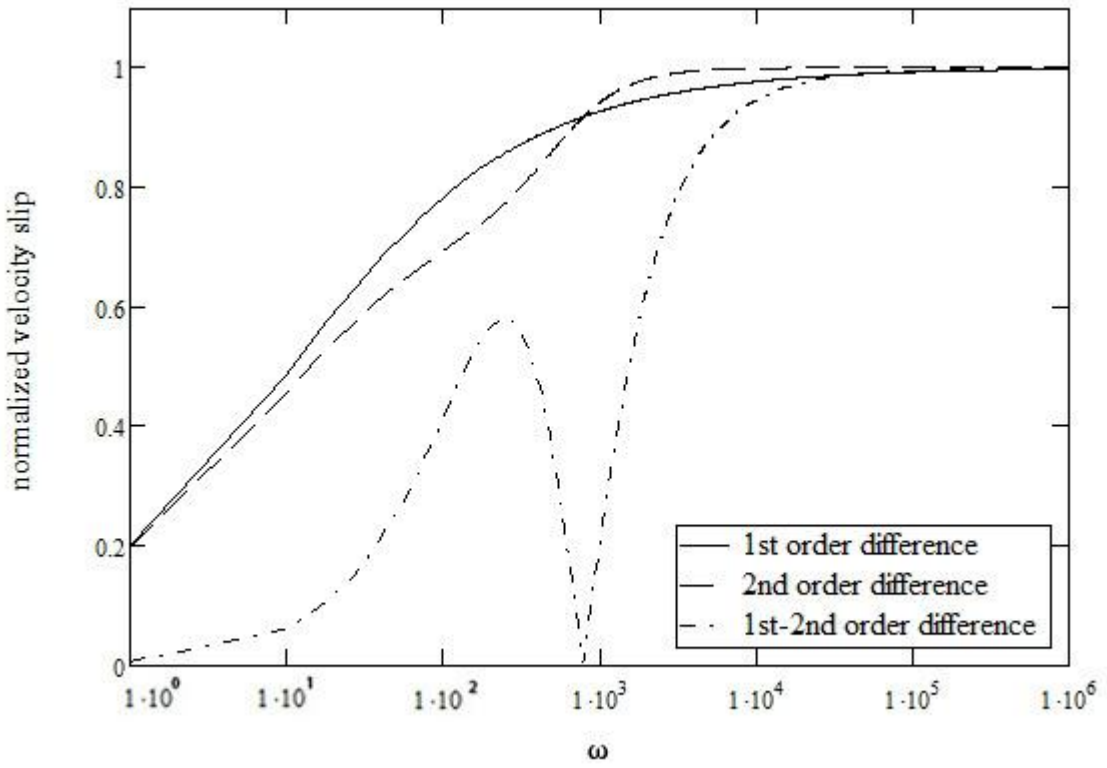

Figure 4.21: Case 3 – Normalized differences of velocity slip as a function of the frequency for $\tau = TP/4$ and $Kn = 0.1$.

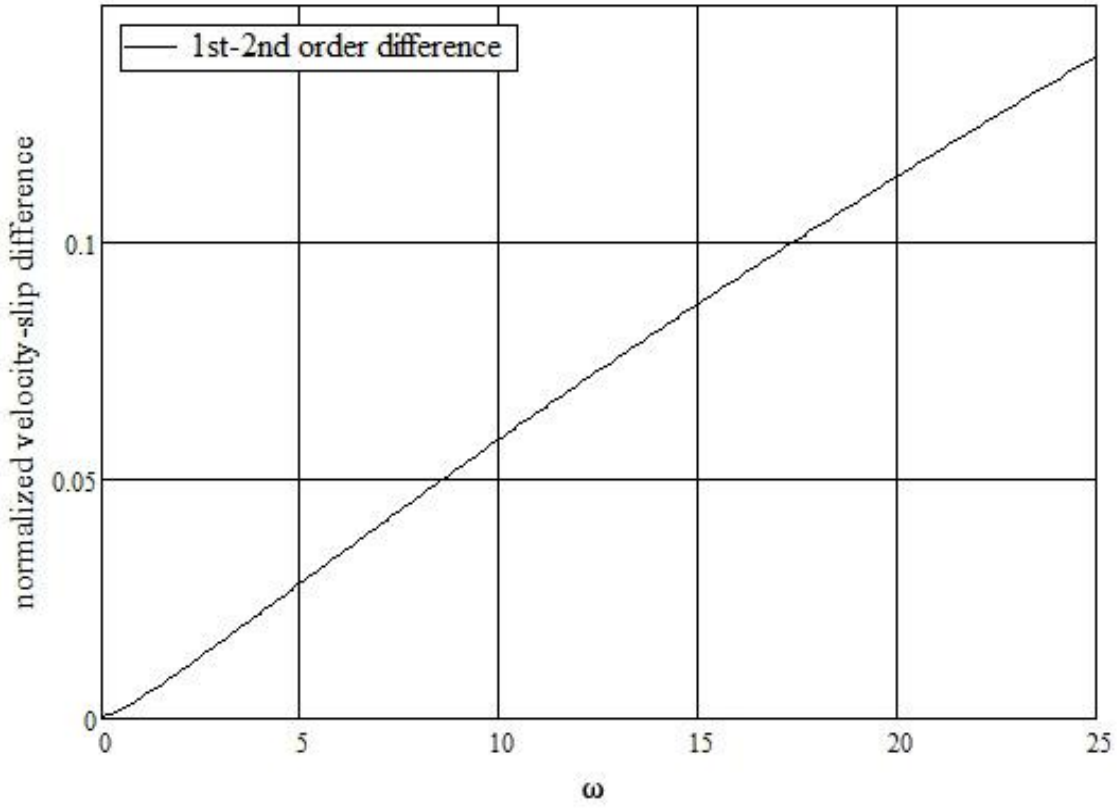

Figure 4.22: Case 3 – Normalized velocity slip difference between first and second order slip as a function of frequency for $\tau = TP/4$ and $Kn = 0.1$.

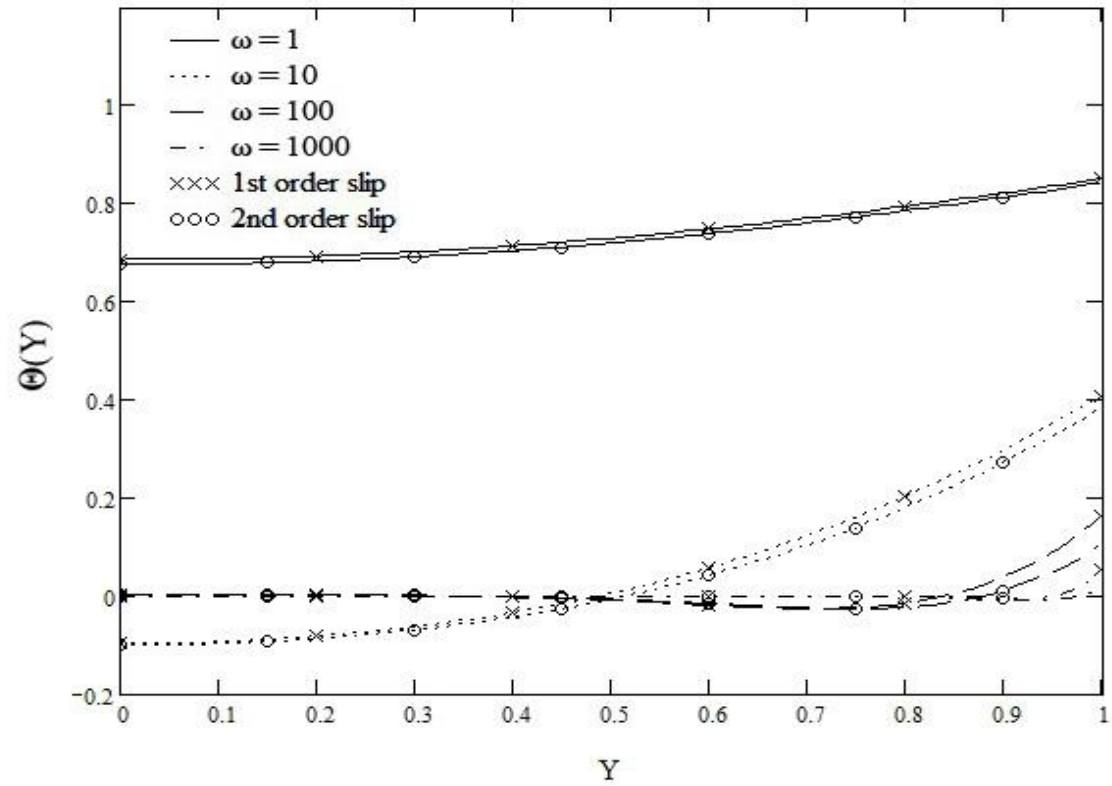

Figure 4.23: Case 4 – Temperature profiles for first and second order slip at $\tau = TP/4$ and $Kn = 0.1$.

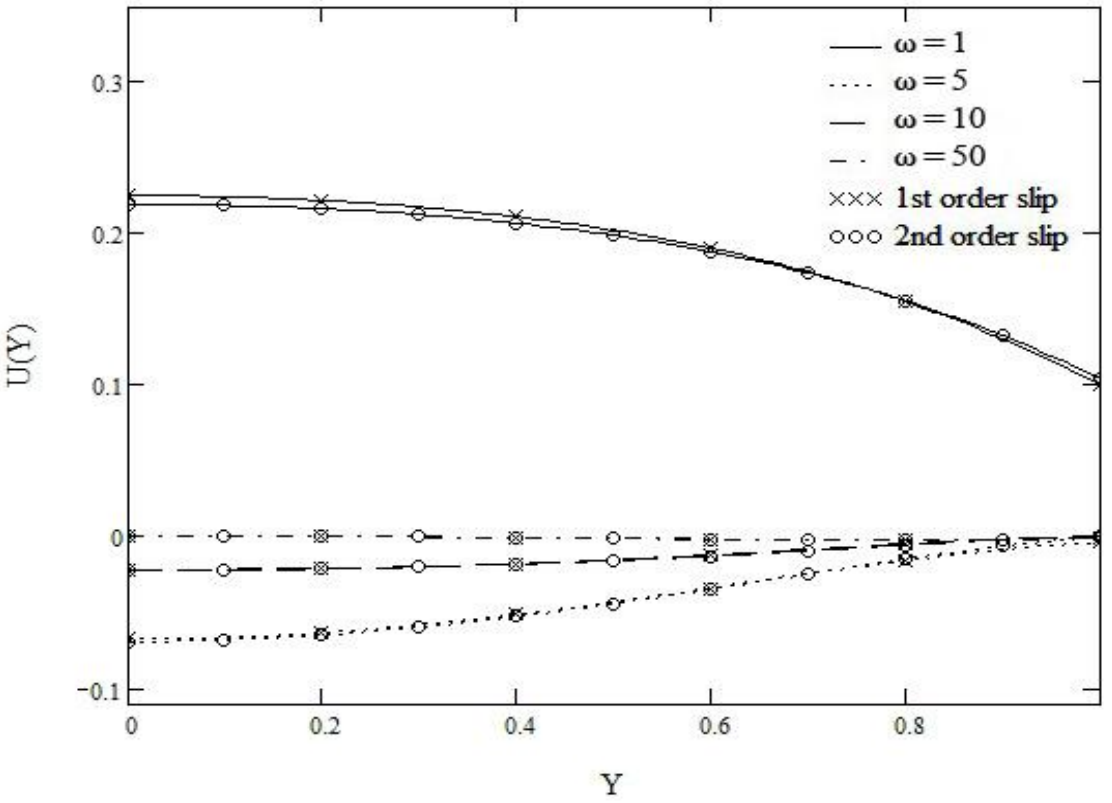

Figure 4.24: Case 4 – Velocity profiles for first and second order slip at $\tau = TP/4$ and $Kn = 0.1$.

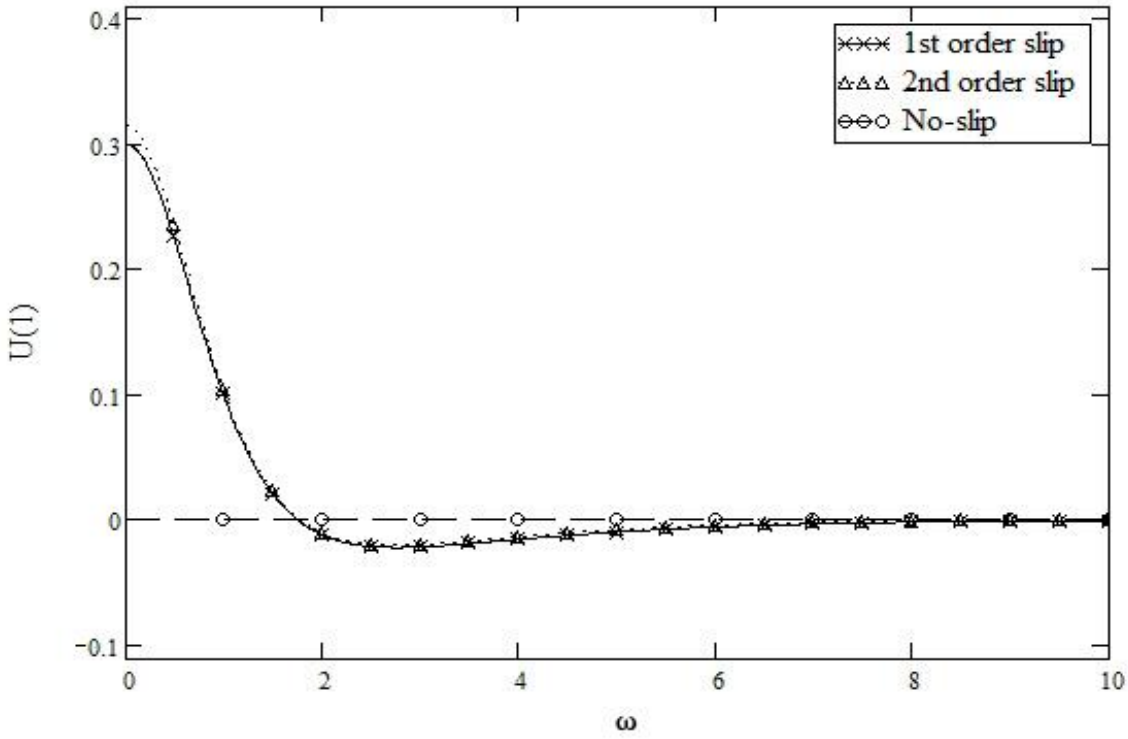

Figure 4.25: Case 4 - Comparison between the slip velocities at the wall as a function of the frequency for $\tau = TP/4$ and $Kn = 0.1$.

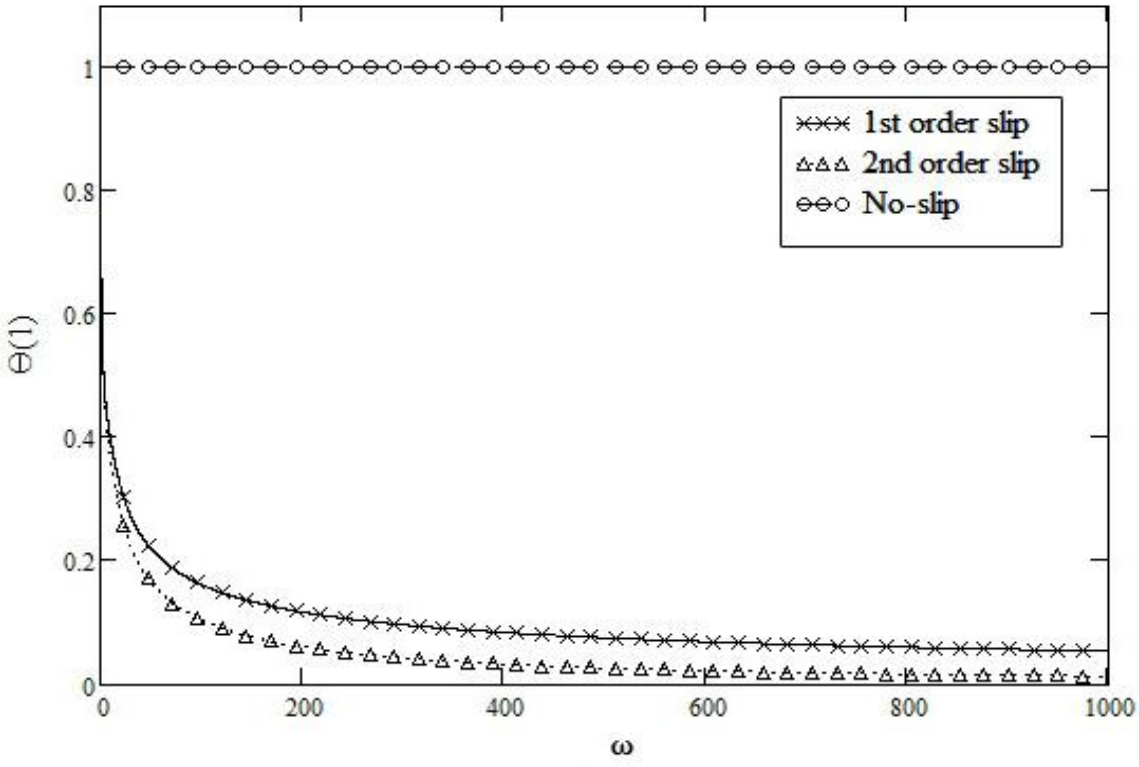

Figure 4.26: Case 4 - Normalized temperature at the wall for the first and second order slip as a function of frequency for $\tau = TP/4$ and $Kn = 0.1$.

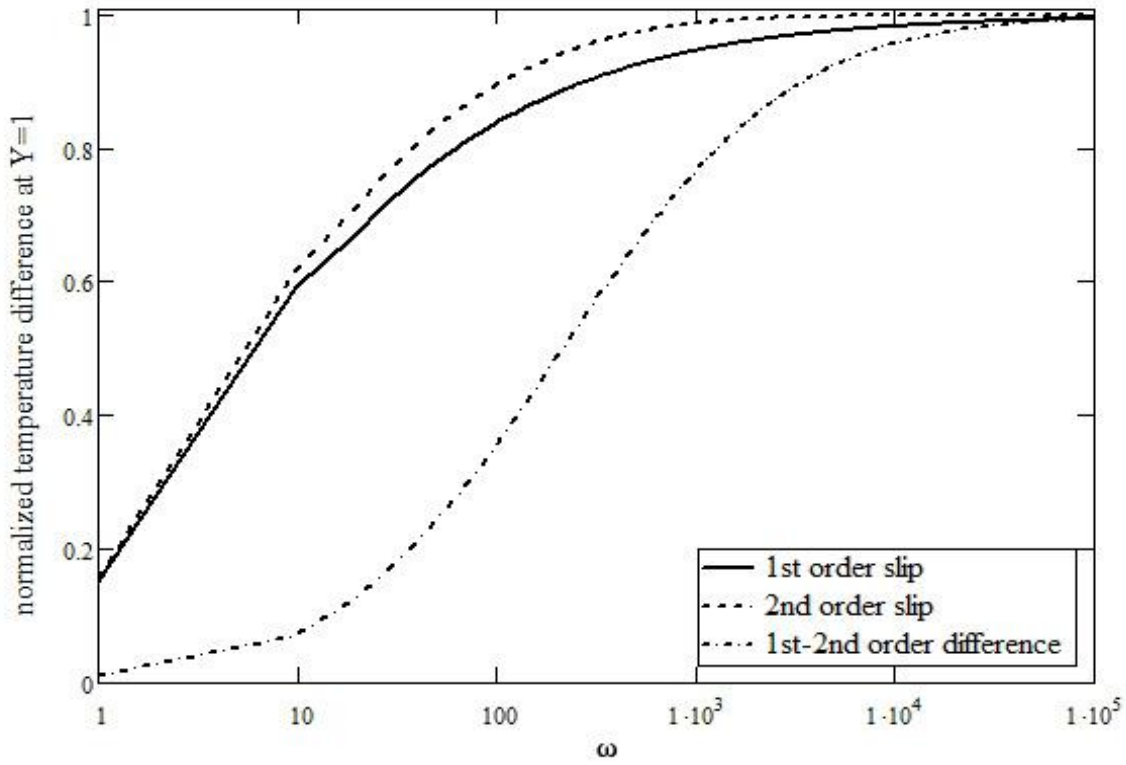

Figure 4.27: Case 4 - Normalized temperature difference at the wall for the first and second order slip as a function of frequency for $\tau = TP/4$ and $Kn = 0.1$.

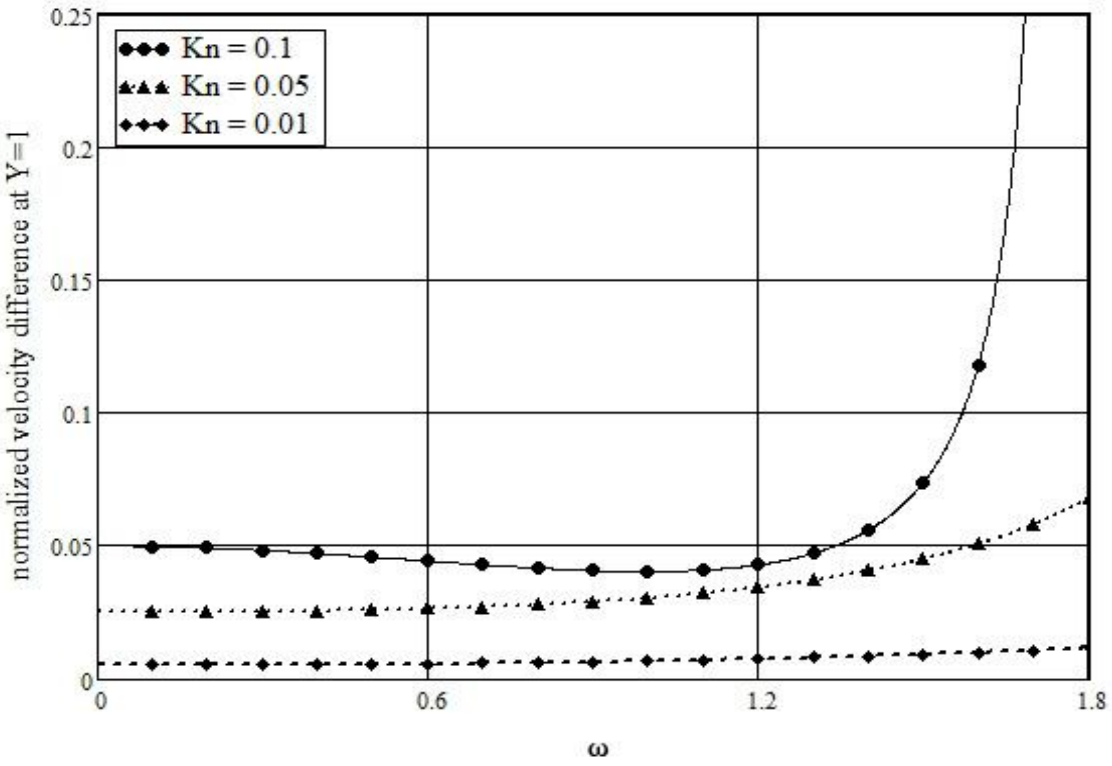

Figure 4.28: Case 4 - Normalized velocity slip difference at the wall between the first and second order slip at the wall as a function of frequency for different *Kn* numbers.

4.3 Fanno Flow in Microchannels

After the above equations have been derived, they were used to plot the figures from 2 to 11. The objective is to investigate the effect of change of the *Knudsen* number *(Kn)* on the flow characteristics derived previously for the range $0.001 \leq Kn \leq 0.1$. This is the range the Navier-Stokes equations with slip boundary conditions are considered in the literature to be applicable. For the purpose of this work the specific heat ratio γ is set to be $\gamma = 1.4$ (air).

The first two figures, Fig. 4.29, 30 show the effect changing the *Kn* number has on the shape of the velocity profiles for the fully developed laminar flow in a circular tube. As it can be seen by looking at these two figures, the velocity profiles for the two slip models is very similar in shape to the no-slip model velocity profile except for the amount of velocity-slip at the wall. Also, by comparing these two figures it is seen that increasing the *Kn* from 0.01 to 0.1 increases the slip at the pipe wall. Another thing which can be noticed from these two figures is that at $Kn = 0.01$ the profiles of the two slip models practically overlap, while at $Kn = 0.1$ they differ but only by a small amount. The amount of slip at the wall is as a function of *Kn* for the two velocity-slip models is summarized in the next figure, Fig.4.31. Here it is seen that even though the two models deviate significantly from the zero value for the no-slip model, for the studied *Kn* number range, they don't deviate significantly from one another. So assuming that a difference between the no-slip model and the first order velocity-slip of *10%* or more is significant enough to justify the use of the velocity-slip model, is can be seen that for $Kn \geq 0.017$ the first order slip model should be used instead of the no-slip model. The difference between the first and the second order slip models does not come even close to *10%* for the

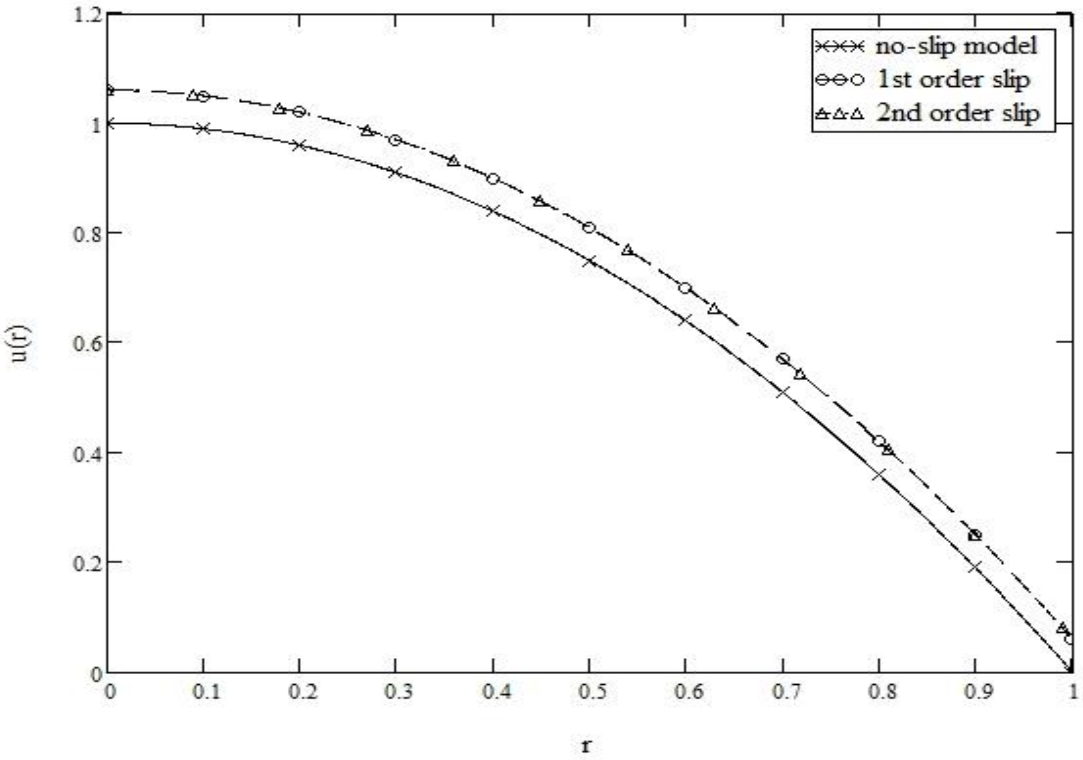

Figure 4.29: Normalized velocity profiles for laminar flow inside circular pipe, using the no-slip, first order and second order slip models at *Kn=0.01*.

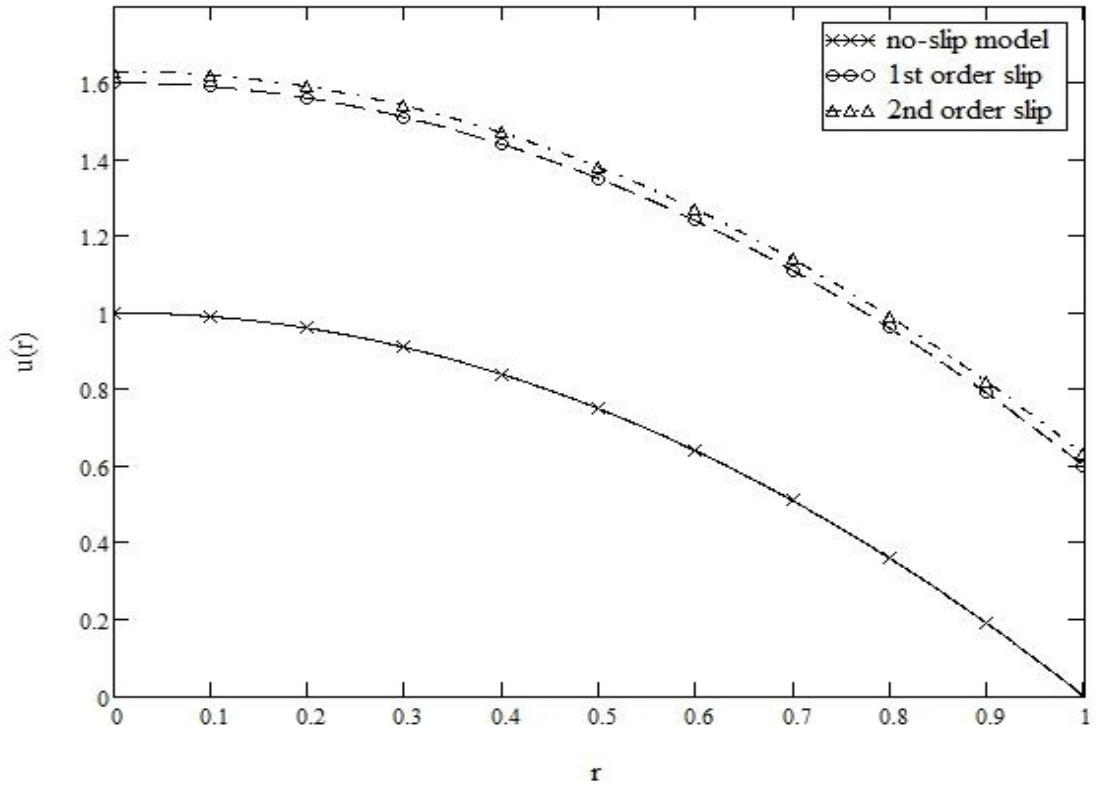

Figure 4.30: Normalized velocity profiles for laminar flow inside circular pipe, using the no-slip, first order and second order slip models at *Kn=0.1*.

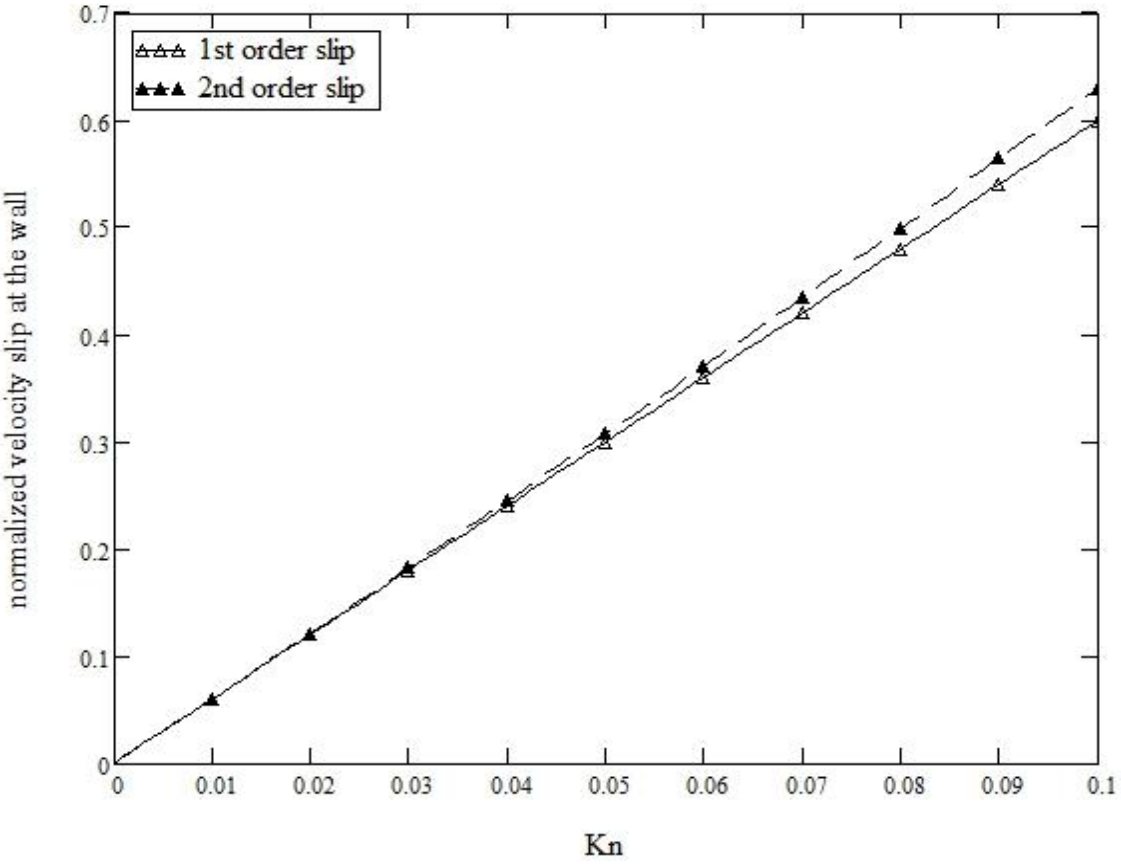

Figure 4.31: Normalized velocity slip at the wall for the first order and second order slip models as a function of *Kn*.

range under considerations so the use of the second order model to find the velocity distribution is neither necessary nor practical.

The next two figures show the skin friction coefficient C_f for the two velocity-slip models. The first figure, Fig. 4.32, represents C_f, as a function of *Kn* number for different values of the tangential-momentum-accommodation coefficient σ_v and using the two velocity-slip models. The tangential-momentum-accommodation coefficient σ_v depends on the type of the fluid, the solid and on the surface finish. It has been experimentally determined to be between 0.2-0.8, the lower limit being for exceptionally smooth surfaces while the upper limit is typical for most practical surfaces. As it can be expected, the smaller σ_v value is, the lower the skin

friction coefficient C_f is. From this figures it is also seen that increasing *Kn* decreases C_f. What is also noted from the figure is that for the range investigated, there is little difference between the results given by the first and the second order slip models. Since the difference between the first order and the second order slip model seems to be negligible for the range under investigation, the next figure Fig. 4.33 shows the effect of *Re* on the C_f for the first order slip model only. It is plotted for different values of *Kn* and as it can be seen, the difference between the no-slip model and the first order slip model becomes apparent only for $Kn \geq 0.01$, and only for relatively low *Re* numbers. As the *Re* number increases this difference becomes smaller so for relatively small *Kn* and higher *Re* the difference becomes insignificant.

The next two figures, show how the change of the *Darcy friction coefficient f* ($f=4C_f$) with *Kn* number, affects the compressible fluid flow in circular tube. The L_{max}/D parameter is plotted against the *Mach number* (*M*) for the first order slip model along with the no-slip model. As it is seen from Fig. 4.34, the first order slip starts to deviate from the no-slip model for $Kn \geq 0.01$ and only for the supersonic flow regime. In the subsonic region, for $Kn \leq 0.01$, there is practically no difference between the no-slip and the first order slip models. In the next figure, Fig. 4.35, the second order slip model is plotted along with the first order slip and the no-slip models at $Kn=0.1$. From this it is seen that although the two slip models deviate much from the no-slip model, they don't deviate from one another except for $M \geq 2$ and even then the difference between them is very small.

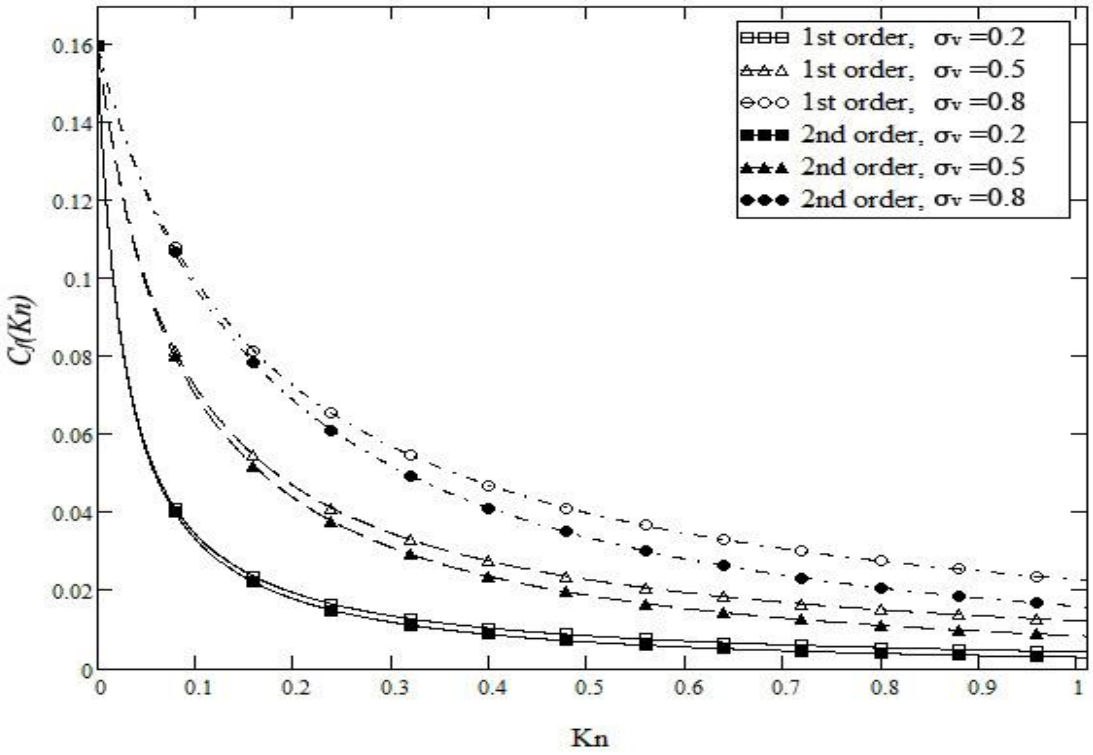

Figure 4.32: Skin friction coefficient C_f as predicted by the first and second order slip models as a function of *Kn* for different values of the accommodation coefficient σ_v at *Re=100*.

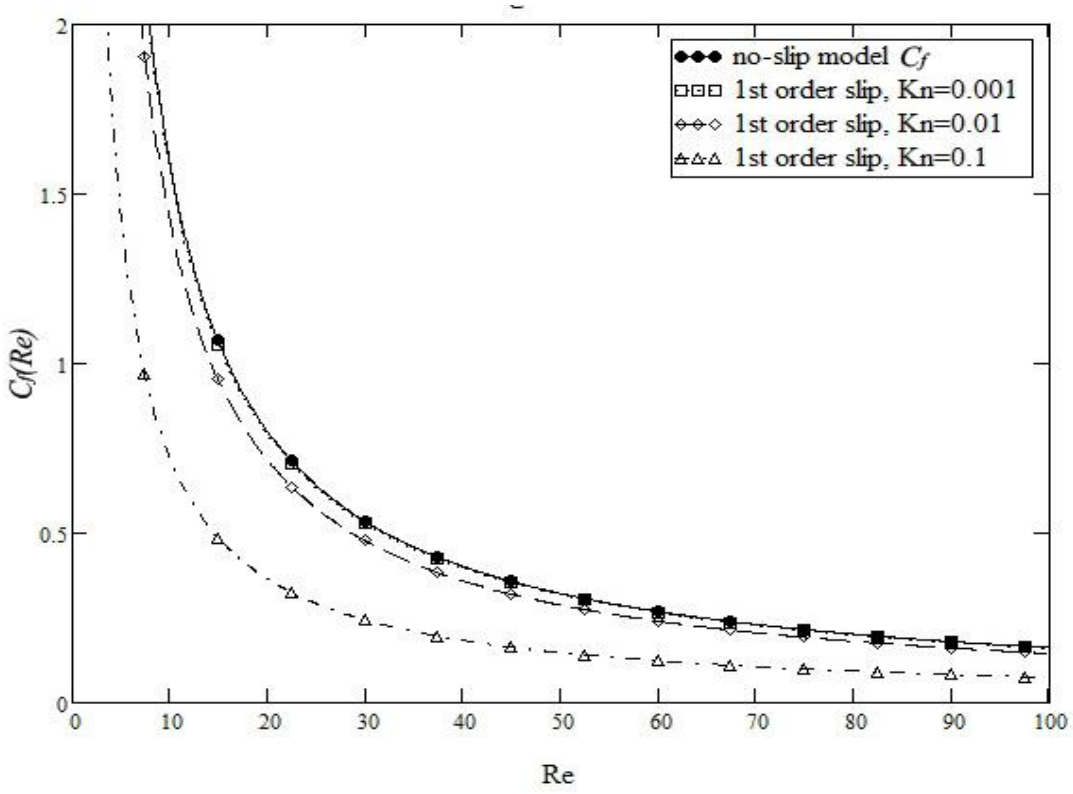

Figure 4.33: Skin friction coefficient C_f for the no-slip and the first order slip models as a function of *Re* for different values of *Kn* and for σ_v=*0.5*.

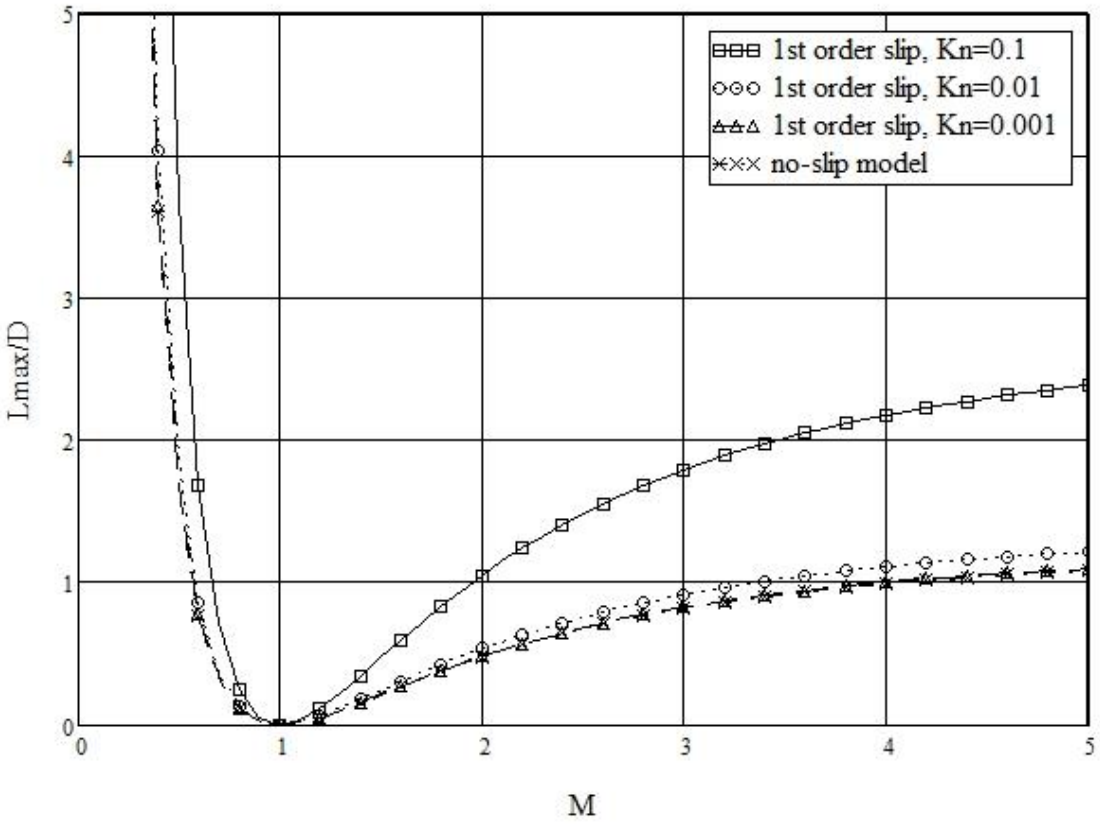

Figure 4.34: Comparison between L_{max}/D *vs. M* for the first order slip model at different *Kn* with the no-slip model for $\sigma_v=0.5$.

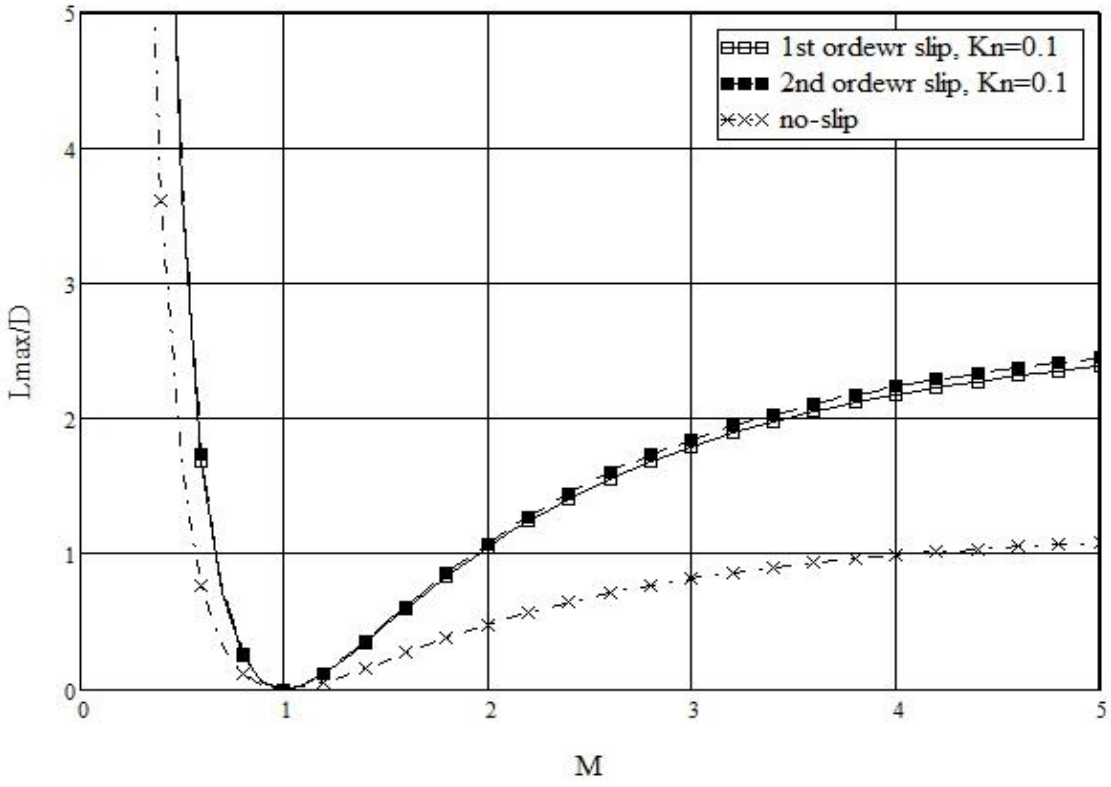

Figure 4.35: Comparison between L_{max}/D *vs. M* for the no-slip, first order and second order slip models at *Kn=0.1* for $\sigma_v=0.5$.

The next two figures, Fig.4.36, 37 are modified plots of *M* and *L/D*, and show how a supersonic/subsonic fully-developed flow will behave as it enters a constant area duct and moves downstream. As a supersonic flow enters a microchannel, due to the friction with the wall it is decelerated along the path until it reaches *M=1*, and Fig.4.36 shows this velocity changes downstream. It is seen that increasing the *Kn* number will increase the *L/D* distance needed for the flow to reach *M=1*. This should be expected because as it was seen above, increasing *Kn* decreases the friction coefficient *f*. For subsonic flow entering a pipe, due to the friction, the flow is accelerated along the way until it finally reaches *M*=1, and Fig. 4.37 shows the velocity change along flow path. As for the supersonic flow, increasing the *Kn* number will increase the *L/D* distance needed for the flow to reach *M=1*.

In the last figure, Fig.4.38 the difference between the critical *L/D* values for the two velocity-slip models as a function of *Kn* for different values of The tangential-momentum-accommodation coefficient σ_v is summarized. What can be seen from looking at Fig.4.36, 37 and 38 is that the difference between the first order slip and the second order slip models is very small compared to the difference between the first order slip and the no-slip model for the whole range of *Kn* number under investigation just as previously observed for the velocity profiles. So if the same criteria of a 10% difference are applied here also, these results would suggest that for an adiabatic compressible flow in circular microchannel, for $Kn \leq 0.01$ there is no need to apply any velocity-slip model as the no-slip model will give sufficiently accurate predictions, while for the range $0.01 \leq Kn \leq 0.1$, the first order velocity slip model should be applied, and there is no necessity to use the second order velocity-slip model.

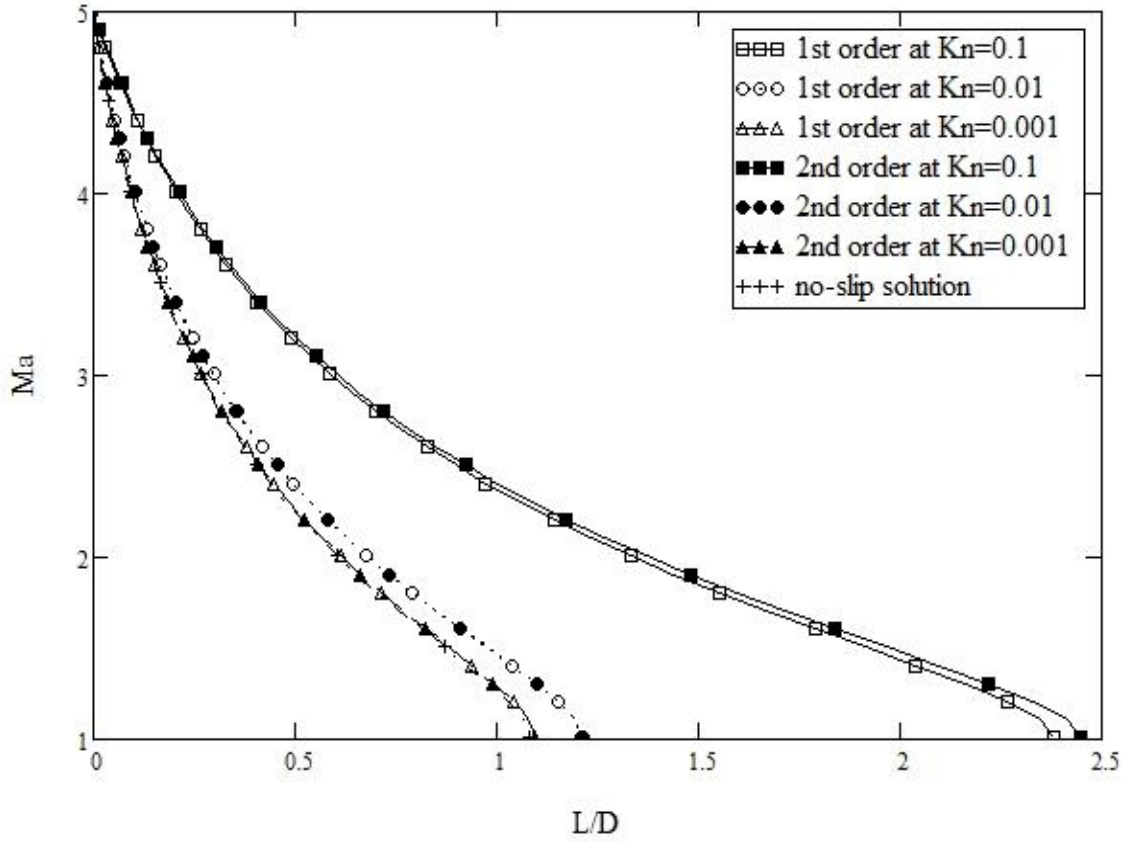

Figure 4.36: Comparison between *M vs.* L_{max}/D for the no-slip, first order and second order slip models for supersonic flow regime for $\sigma_v=0.5$.

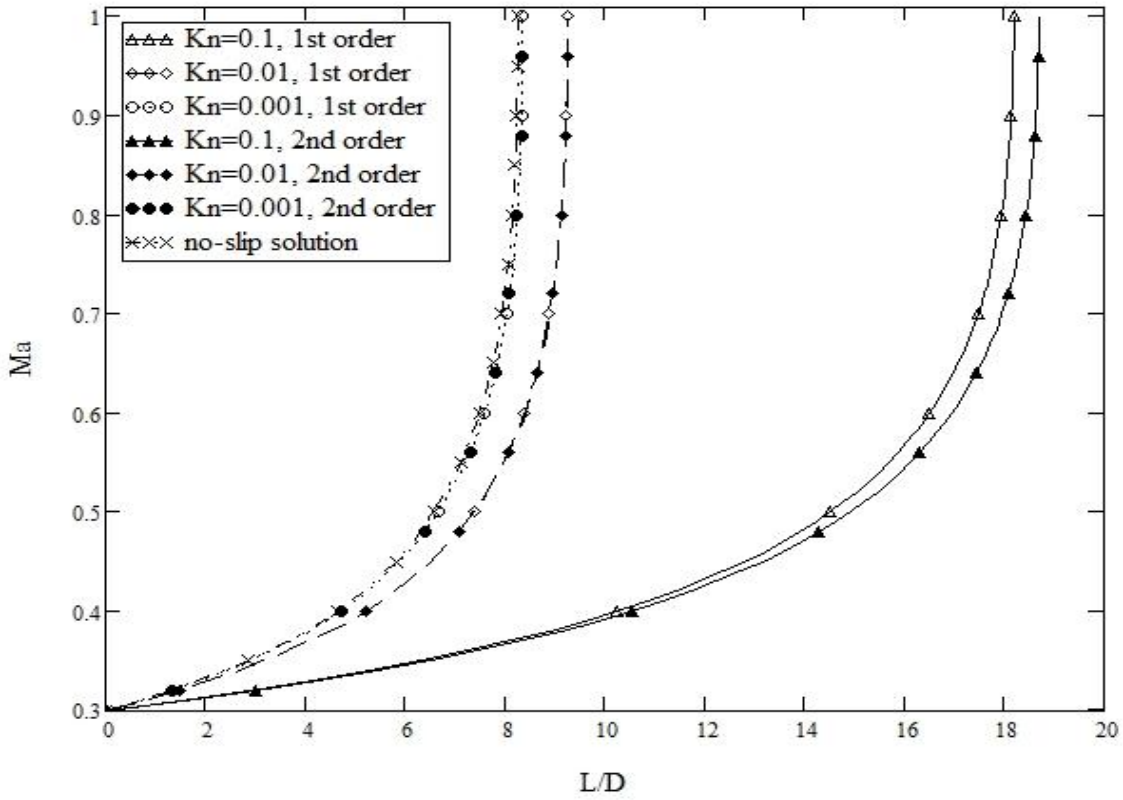

Figure 4.37: Comparison between *M vs.* L_{max}/D for the no-slip, first order and second order slip models for subsonic flow regime for $\sigma_v=0.5$.

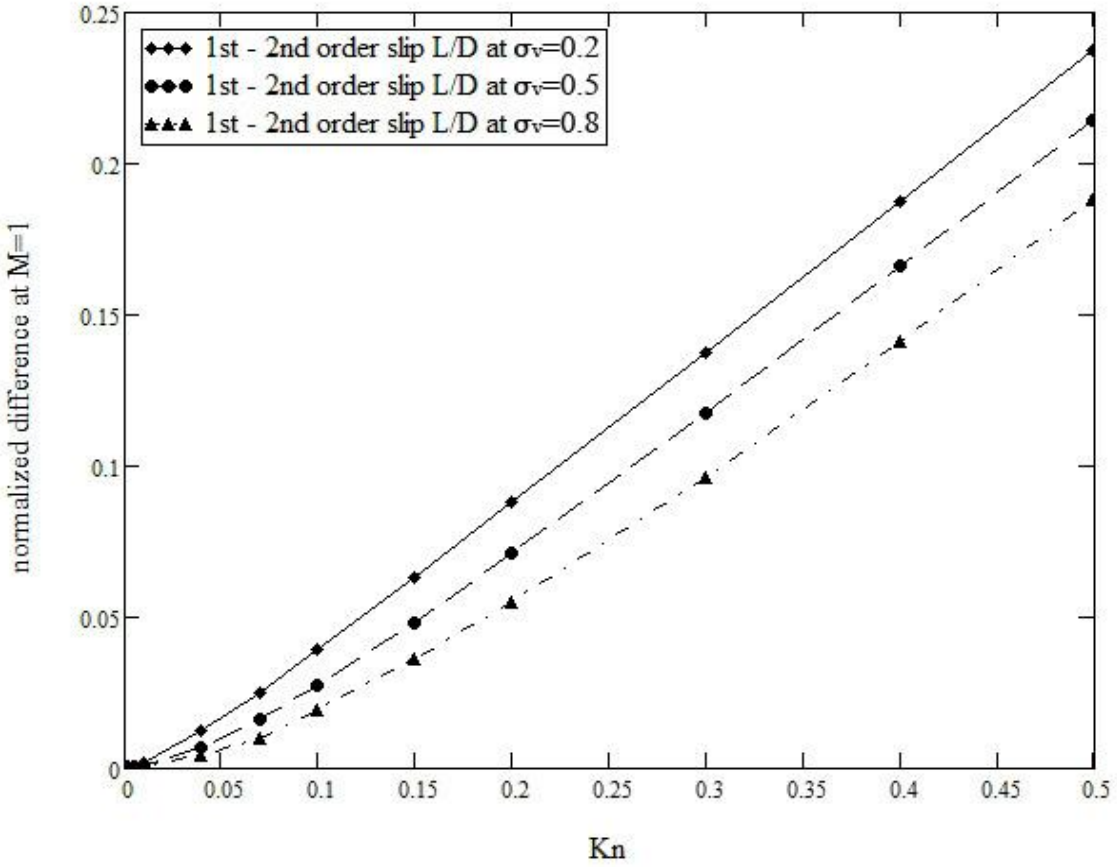

Figure 4.38: Normalized difference between L_{max}/D for the first order and second order slip models as a function of *Kn* number.

Chapter Five

Conclusions and Recommendations

In this work, three different cases that cover different flow patterns in microchannels was studied by implementing the first and second order velocity-slip/temperature jump models in order to observe the behavior of the flow so that a certain criteria for the use of each of the no-slip, the first order slip and the second order slip models. These three cases are; the Jeffery-Hamel flow in microchannels, Fanno flow in circular microchannels and basic fluctuating flows in microchannels.

5.1 Jeffery-Hamel Flow

In the first section, the Jeffery-Hamel flow case has been studied using both, first order and second order velocity-slip boundary conditions models and then compared to the no-slip boundary conditions solution. The study concentrates on investigating the effect the change of *Kn* number has on the velocity profiles, magnitude of slip at the wall and the skin friction coefficient. A Jeffery-Hamel flow is radial flow caused by a line source or sink. The major factor in this kind of flows is the combined $Re \cdot \alpha$ factor according to which the flow can be divided into two categories, inflow and outflow. When $Re \cdot \alpha < 0$ the flow is toward a sink and is called inflow, and when $Re \cdot \alpha > 0$ the flow is outward of a source and is called outflow.

For the inflow case it was found that due to the favorable pressure gradient the differences between the three models studied increases significantly as the *Kn* number increases and according to that three *Kn* number regions can be established. The first is the region where there is no need to use any velocity-slip model as the no-slip model is

accurate enough. The second is the region where the first order velocity slip model is sufficient and the third region is where only the second order velocity-slip model will suffice. As an example, for the case of $Re{\cdot}\alpha=-10$, these regions are: for $0<Kn<0.01$, the no-slip boundary conditions model is sufficient, for $0.01<Kn<0.05$, the first order velocity-slip model becomes necessary, and for $0.05<Kn<0.1$ the second order velocity-slip model will have to be used.

In the outflow case the things stand a little more complex, as for $0<Re{\cdot}\alpha<8$, the difference between the no-slip model and the two slip models is much smaller than for the inflow case, for example, at $Re{\cdot}\alpha=+5$, the difference becomes significant only at about $Kn>0.04$, so up to then the no slip model will give acceptable results. Also the difference between the first order slip and the second order slip models is negligible for almost the entire range of Kn numbers. But as $Re{\cdot}\alpha$ parameter becomes larger, and for relatively large Kn numbers, the adverse pressure gradient causes the flow at the wall to separate at $Re{\cdot}\alpha$ values lower than 10.31, the value obtained for the no-slip boundary conditions model. This fact is predicted only by the second order velocity-slip model for $9<Re{\cdot}\alpha<10.31$. So for outflow cases near the separation flow region the second order velocity-slip model should always be used.

It was also found that increasing the Kn number decreases the skin friction coefficient C_f calculated using the two velocity-slip models in all cases except for when separation occurs, as when the velocity at the wall is reversed as predicted by the second order velocity-slip model, this factor increases.

5.2 Basic Gaseous Fluctuating Micro-Flows

In the second part, the effect of adding the second order term to the velocity-slip/temperature-jump boundary condition has on the solution of four cases in which the

driving force is fluctuating was examined. The study concentrated on comparing the effect frequency has on the velocity and temperature solutions at given *Kn* number using the first and the second order slip/jump models. For most of the figures the *Kn* number was fixed at *Kn=0.1* as it is considered the upper bound of the *Kn* number regime in which the Navier-Stokes equations with slip boundary conditions are applicable and also because the larger the *Kn* number is, the more pronounced the effect of increasing the frequency is.

As the figures show, at a given *Kn* number value, increasing the driving force frequency increases the difference between the first and second order models. Assuming that a difference of over 5% is significant enough to justify the use of the more complex model the critical frequencies for the four different cases were found. It was found that the critical frequency for which the second order velocity-slip model should be used instead of the first order depends on the *Kn* number and also on the type of the flow driving force.

For the cases for which the flow is induced by the fluctuating wall as in cases 1 and 3 and at $Kn = 0.1$ it is found to be $\varpi = 8\nu/L^2$ for case 1 and $\varpi = 8u_0^2/\nu$ for case 3.

For the cases of flow driven by a fluctuating pressure gradient *dp/dx* as in case 2, this frequency was found to be much lower, as a comparison for the same value of $Kn = 0.1$ the frequency is $\varpi = \nu/L^2$, i.e. eight times smaller.

As for case 4, the fluctuating wall temperature driven transient natural convection flow there are two critical frequencies at which the difference between the first order and second order models becomes significant. The first is for the temperature-jump model and was found to be $\varpi_t = 7\nu/L^2$ at $Kn = 0.1$. The second, the velocity-slip model critical frequency at the same *Kn* number was found to be $\varpi_v = 1.35\nu/L^2$.

5.3 Fanno Flow in Microchannels

In the third part, the Fanno flow problem has been studied using both, first order and second order velocity-slip boundary conditions models and then compared to the no-slip boundary conditions solution. The study concentrates on investigating the effect the change of *Kn* number has on the velocity profiles, magnitude of slip at the wall, skin friction coefficient C_f and the L_{max}/D factor characteristic of Fanno line. The Fanno flow is an ideal gas adiabatic flow in constant area duct with friction. For this case the circular pipe geometry has been chosen and all the flow characteristics have been derived for the first and second order velocity-slip models.

It is found that the velocity profile for the two velocity-slip models has generally the same shape as the no-slip model velocity profile but with a slip at the wall. This slip increases as the *Kn* increases and for $Kn \geq 0.01$ it becomes significant enough and the first order slip model should be used instead of the no-slip model. Also, the skin friction coefficient C_f is found to decrease as the *Kn* increases. Also the effect of the slip has on the compressible flow characteristics have been examined. It shows that as the *Kn* number increases, the friction coefficient *f* decreases. This reduction in friction leads to increase of the *L/D* parameter for both supersonic and subsonic flows with slip when compared to the no-slip solution.

Overall, it is concluded that for an adiabatic compressible flow in circular microchannel, for $Kn \leq 0.01$ there is no need to apply any velocity-slip model as the no-slip model will give sufficiently accurate predictions. As for the range $0.01 \leq Kn \leq 0.1$, the first order velocity slip model should be applied, and that for this range, there is no necessity to use the second order velocity-slip model.

This work has been concerned with the comparison between the first order slip model and the second order slip model for a number of cases. One recommendation for further work that comes to mind is to compare the second order slip model with some well established molecular model as for example the Direct Monte Carlo Simulation (DMCS) for the region $Kn \geq 0.1$, i.e. for the transitional region, in order to study the second order velocity-slip/temperature-jump model's accuracy and applicable Kn number range.

References

Alexeenko, A. A., Gimelshein, S. F., and Levin, D. A., (2005), "Reconsideration of Low Reynolds Number Flow-Through Constriction Microchannels Using the DSMC Method", **Journal Of Microelectromechanical Systems**, Vol. 14, No. 4, August 2005.

Ambatipudi, K. K., and Rahman, M. M., (2000), "Analysis of Conjugate Heat Transfer in Microchannel Heat Sinks", **Numerical Heat Transfer**, Part A, 37: 711 –731, Taylor & Francis.

Araki, T., Kim, M. S., Iwai, H. and Suzuki, K., (2002), "An Experimental Investigation of Gaseous Flow Characteristics in Microchannels", **Microscale Thermophysical Engineering**, 6:117–130, Taylor & Francis.

Arkilic, E. B., Breuer K. S. and Schmidt, M. A., (2001), "Mass Flow and Tangential Momentum Accommodation in Silicon Micromachined Channels", **J. Fluid Mech.**, Vol. 437, pp. 29.

Asako, Y., Pi, T., Turner S. E. and Faghri, M., (2003), "Effect of Compressibility on Gaseous Flows in Micro-Channels", **International Journal of Heat and Mass Transfer** 46, 3041–3050.

Beskok, A., and Karniadakis, G. E., (1994), "Simulation of Heat and Momentum Transfer in Complex Micro-Geometries", **Journal of Thermophysics and Heat Transfer**, Vol. 8, pp. 355-370

Beskok, A., Karniadakis, G. E. and Trimmer, W., (1996), "Rarefaction and Compressibility Effects in Gas Microflows ", **ASME Journal of Fluid Engineering, Vol. 118, pp. 448-456.**

Celata, G. P., (2004), "Single-Phase Heat Transfer and Fluid Flow in Micropipes", **Heat Transfer Engineering**, 25(3):13–22, Taylor & Francis Inc.

Chen, Y., Kang, S., Tuh W. and Hsiao, T., (2004), "Experimental Investigation of Fluid Flow and Heat Transfer in Microchannels", **Tamkang Journal of Science and Engineering**, Vol. 7, No. 1, pp. 11−16.

Choi, S. B., Barron, R. F. and Warrington, R. O., "Fluid Flow and Heat Transfer in Microtubes", Micromech. **Sensors Actuators Sys.** Vol. 32, pp.123-134.

Choquette, S. F., Faghri, M., Kenyon, E. J. and Sunden, B., (1996), "Compressible Fluid Flow in Micron-Sized Channels", **Nat. Heat Transfer Conf.** 5, 25-32.

Colin, S., Lalonde, P. And Caen, R., (2004), "Validation of a Second-Order Slip Flow Model in Rectangular Microchannels", **Heat Transfer Engineering**, 5(3):23–30, Taylor & Francis Inc.

Currie, I. G., (1993), "**Fundamental Mechanics of Fluids**", McGraw-Hill.

Duncan, G. P. and Peterson, G. P., (1994), "Review of Microscale Heat Transfer". **Appl. Mech. Rev.** 47(9), 397-428.

Faghri, M. and Sun, H., (2003), "Effect of Surface Roughness on Nitrogen Flow in a Microchannel Using the Direct Simulation Monte Carlo Method", **Numerical Heat Transfer**, Part A, 43: 1-8.

Gad-el-Hak, M., (1999), "The Fluid Mechanics of Microdevices - The Freeman Scholar Lecture", **Journal of Fluid Engineering**, Vol. 121, March 1999, pp. 5-33.

Gad-el-Hak, M., (2002), "Flow Physics in Microdevices", **The Handbook of MEMS**, CRC Press, Boca Raton, Florida, 2002.

Gao, P., Le Person, S. and Favre-Marinet, M., (2002), "Scale effects on hydrodynamics and heat transfer in two-dimensional mini and microchannels", International Journal of Thermal Sciences 41, 1017–1027.

Haddad, O., Al-Nimr, M. and Abuzaid, M., (2005), "The Effect of Frequency of Fluctuating Driving Force on Basic Gaseous Micro-Flows", **Acta Mechanica**, Aug. 2005, Springer-Verlag.

Hamel, G., (1917), Spiralförmige Bewegung zäher Flüssigkeiten", **Jahresber. Deutsch. Math.** Ver., Vol.25, pp. 34-60

Harley, J. C., Huang, Y., Bau, H. and Zemel, J. N., (1995), "Gas Flows in Micro-Channels", **Journal of Fluid Mechanics** 284, 257-274.

Ho, C. and Tai, Y., (1998), "Micro-Electro-Mechanical Systems (MEMS) and Fluid Flows", **Ann. Rev. Fluid Mech.** 30, 579-612.

Jeffery, G. B., (1915), "The Two-Dimensional Steady Motion of a Viscous Fluid", **Phil. Mag.**, Vol.29, pp. 455-465.

John, J. E.A., (1984), "**Gas Dynamics**", 2nd ed., Prentice Hall.

Karniadakis, G. and Beskok, A., (2002), "**Micro Flows Fundamentals and Simulation**", New York: Springer.

Khaled, A. and Vafai, K., (2004), "The Effect of the Slip Condition on Stokes and Couette Flows due to an Oscillating Wall: Exact Solutions", **International Journal of Non-Linear Mechanics**, Vol. 39, 795-809.

Kucaba-Piętal, A., (2004), "Microchannels Flow Modelling with the Micropolar Fluid Theory", **Bulletin of The Polish Academy of Sciences, Technical Sciences**, Vol. 52, No. 3.

Lauga, E., (2005), "Microfluidics: The No-Slip Boundary Condition", Ch. 15 in **Handbook of Experimental Fluid Dynamics**, Editors: J. Foss, C. Tropea and A. Yarin, Springer, New-York.

Martin M. J. and Boyd, I. D., (2001),"Blasius Boundary Layer Solution with Slip Flow Conditions", RAREFIED GAS DYNAMICS: 22nd **International Symposium. AIP Conference Proceedings**, Volume 585, pp. 518-523.

Maxwell, J. C., (1879), "On Stresses in Rarefied Gases Arising from Inequalities of Temperature", **Philosophical Transactions of the Royal Society Part 1**, Vol.170, pp. 231-256.

Millsaps, K. and K. Pohlhausen, (1953), "Thermal Distribution in Jeffery-Hamel Flows between Nonparallel Walls", **J. Auronaut. Sci**., Vol.20, pp. 187-196.

N. T. Obot, (2002), "Toward a Better Understanding of Friction and Heat/Mass Transfer in Microchannels - A Literature Review", **Microscale Thermophysical Engineering**, 6:155–173.

Nishio, S., (2004), "Single-Phase Laminar-Flow Heat Transfer and Two-Phase Oscillating-Flow Heat Transport in Microchannels", **Heat Transfer Engineering**, 25(3):31–43, Taylor & Francis Inc.

Peng, X. F., Peterson, G. P. and Wang, B. X., (1994), "Frictional Flow Characteristics of Water Flowing Through Microchannels", **Exp. Heat Transfer**, Vol. 7, pp 249-264.

Pettersen, J., (2004), "Two-Phase Flow Patterns in Microchannel Vaporization of CO_2 at Near-Critical Pressure", **Heat Transfer Engineering**, 25(3):52–60, Taylor & Francis Inc.

Rosenhead, L., (1940), "The Steady Two-Dimensional Radial Flow of Viscous Fluid Between Two Inclined Planes", **Proc. Roy. Soc. London Ser. A**, Vol.175, pp. 436-467.

Roy, S., Raju, R., Chuang, H. F., Cruden, B. A. and Meyyappan, M., (2003), "Modeling Gas Flow Through Microchannels and Nanopores", **Journal of Applied Physics**, Vol. 93, no.8, pp. 4870-4879.

Smoluchowski, von M., (1898), "Ueber Wärmeleitung in verdünnten Gasen", **Annalen der Physik und Chemie**, Vol.64, pp. 101-130.

Toh, K.C., Chen, X. Y. and Chai, J. C., (2002), "Numerical computation of fluid flow and heat transfer in microchannels", **International Journal of Heat and Mass Transfer** 45, 5133–5141.

Tretheway, D. C., Zhu, L., Petzold, L., and Meinhart, C. D. , (2002), "Examination of the Slip Boundary Condition by μ-Piv and Lattice Boltzmann Simulations", Proceedings of IMECE'2002, **ASME International Mechanical Engineering Congress & Exposition**, New Orleans, Louisiana, November 17-22.

Tzeng, P. Y. and Chen, P. H., (2003), "Numerical Visualization of Gaseous Micro-Channel Flow in Transition Regime", **Proceedings of PSFVIP-4** June 3-5, Chamonix, France.

White, F. M., (1991), "**Viscous Fluid Flow**", 2nd ed., McGraw-Hill, Inc.

Xue, H. and Fan, Q., (2000), "A High Order Modification on the Analytic Solution of 2-D Microchannel Gaseous Flows", proceedings of ASME FEDSM'00, **ASME 2000 Fluid Engineering Division Summer Meeting**, Boston Massachusetts, June 11-15.

دراسة تأثير انزلاق السرعة و قفز الحرارة من الدرجة الثانية على الجريان في القنوات المجهرية

اعداد
فلاديمير اكرم سليم حموده

المشرف
الأستاذ الدكتور محمد احمد حمدان

المشرف المشارك
الأستاذ الدكتور محمد احمد النمر

ملـخـص

تناول هذا العمل دراسة ثلاث حالات تغطي انماط مختلفة من الجريان في القنوات المجهرية باستخدام نماذج انزلاق السرعة و القفز في الحرارة م ن الدرجتين الاولى و الثانية، و ذلك بهدف التنبوء بسلوك الجريان من اجل وضع معايير لاستخدام كل من النموذجين المذكورين (الأول و الثاني).

في الجزء الاول من العمل تمت دراسة الحالة المسماة (Jeffery-Hamel) باسخدام نموذجي الانزلاق من الدرجة الاولى و الثانية و من ثم مقارنة النتائج بالنموذج التقليدي اي نموذج اللا-انزلاق. تركز الجزء على دراسة تاثير التغير في قيمة ال (Kn) على توزيع السرعة ، مقدار الانزلاق عند الجدار قيمة معامل الاحتكاك عند السطح. في حالة الجريان الى الداخل وجد انه و بسبب الضغط الايجابي كان الفرق بين النماذج الثلاث واضحاً و ازداد هذا الفرق مع زيادة قيمة (Kn) و بناءاً على ذلك يمكن تحديد ثلاث مناطق مختلفة لاستخدام كل من النماذج الثلاثة المذكورة. اما في حالة الجريان الى الخارج فان الفرق بين النماذج الثلاثة كان اقل بكثير لكن و مع اقتراب المتغير ($Re\cdot\alpha$) من القيمة الحرجة له و مع زيادة ال (Kn) فأنه من الملاحظ ان سرعة الجريان عند الجدار تنعكس فيما يسمى بظاهرة الانفصال. هذه النتيجة لم تظهر الا عند استخدام نموذج الانزلاق من الدرجة الثانية و بناءاً على ذلك فانه ينصح بتطبيق نموذج الدرجة الثانية عندما تكون ظروف الجريان قريبة من المنطقة الحرجة. أيضاً تم ملاحظة أن زيادة مقدار (Kn) تؤدي الى نقصان مقدار معامل الاحتكاك مع الجدار باستثناء حالة انعكاس سرعة الجريان فعندها يزداد معامل الاحتكاك.

تركزت الدراسة في الجزء الثاني على تأثير اضافة الحد الثاني لعلاقة انزلاق السرعة و القفز في درجة الحرارة و ذلك في اربع حالات مختلفة تشترك جميعها بان القوة المسببة للجريان فيها متذبذبة. تركز الاهتمام على تأثير تردد القوة الدافعة على توزيع السرعة و الحرارة للمائع عند قيم محددة لل(Kn). وجد في هذا الجزء أن زيادة مقدار التردد تؤدي الى زيادة الفرق بين نموذجي انزلاق السرعة من الدرجة الأولى و الثانية. كما انه تم ايجاد الترددات الحرجة الخاصة بكل من الحالات الاربع و هي الترددات التي عند زيادة تردد القوة الدافعة عنها يفضل تطبيق نموذج

الدرجة الثانية عوضاً عن نموذج الدرجة الأولى. وجد ايضاً ان هذه الترددات الحرجة تعتمد بشكل رئيسي على نوع القوة الدافعة المسببة للجريان.

اما في الجزء الاخير من العمل فقد تمت دراسة جريان غاز قابل للانضغاط في قناة مجهرية دائرية المقطع فيما يعرف ب(Fanno Flow) باستخدام نموذجي الانزلاق من الدرجة الاولى و الثانية. تركز الاهتمام على دراسة تاثير التغير في ال (Kn) على توزيع السرعة و مقدار انزلاقها عند الجدار و ايضاً معامل الاحتكاك مع الجدار و المتغير الخاص بهذه الحالة (L_{max}/D). ما تمت ملاحظته ان الزيادة في قيمة (Kn) تؤدي الى زيادة مقدار الانزلاق عند الجدار و نقصان معامل الاحتكاك مع السطح. نقصان مقدار الاحتكاك عند الجدار تؤدي الى زيادة مقدار المتغير (L_{max}/D) سواءً كانت سرعة الجريان اقل او اكثر من سرعة الصوت في حالة استخدام نموذجي الانزلاق من الدرجة الاولى و الثانية مقارنة بالنموذج التقليدي (اللا-انزلاق). تم التوصل الى نتيجة أنه لا ضرورة لاستخدام أي من نماذج الأنزلاق للقيم المنخفضة نسبياً من ال(Kn) كون النموذج التقليدي الأبسط يعطي نتائج مُرضية، بينما يفضل تطبيق نموذج الأنزلاق من الدرجة الأولى للقيم الأعلى نسبياً من ال(Kn) و لا ضرورة لأستخدام نموذج الأنزلاق من الدرجة الثانية.